A LOW COST SENSOR SYTEM FOR MONITORING AND PREDICTING CORROSION OF LONG TERM SPENT NUCLEAR FUEL STORAGE

by

Vikram M. Patel

A dissertation

Submitted in partial fulfillment

Of the requirements for the degree of

Doctor of Philosophy in Electrical and Computer Engineering

Boise State University

May 2021

BOISE STATE UNIVERSITY GRADUATE COLLEGE

DEFENSE COMMITTEE AND FINAL READING APPROVALS

of the thesis submitted by

Vikram M. Patel

Thesis Title: A Low Cost Sensor System for Monitoring and Predicting Corrosion of Long Term Spent Nuclear Fuel Storage

Date of Final Oral Examination: 16 July 2019

The following individuals read and discussed the thesis submitted by student Vikram M. Patel, and they evaluated her presentation and response to questions during the final oral examination. They found that the student passed the final oral examination.

Sin Ming Loo, Ph.D.	Chair, Supervisory Committee
Mike Hurley, Ph.D.	Member, Supervisory Committee
Jim Browning, Ph.D.	Member, Supervisory Committee
Brian Jaques, Ph.D.	Member, Supervisory Committee
Gabriel O. Ilevbare Ph.D.	External Examiner

The final reading approval of the thesis was granted by Sin Ming Loo, Ph.D., Chair of the Supervisory Committee. The thesis was approved by the Graduate College.

ACKNOWLEDGEMENTS

None of the work in this dissertation would have been possible without a generous grant from the Department of Energy and the College of Engineering at Boise State University. The Hartman System Integration Laboratory along with the facilities belonging to the Department of Material Science were key in both the development and testing of the work contained within this dissertation. More importantly, the faculty and research students belong to these organizations provided the support and knowledge base for these advancements to be made and truly the cornerstone of this research.

ABSTRACT

With the closing of the Yucca mountain storage facility, on-site storage of spent nuclear fuel at reactor sites has increased and will continue to increase until a permanent storage facility is prepared. Dry storage canisters are used to store spent nuclear fuel waste over long periods of time, but are susceptible to mechanical failure via corrosion. This dissertation presents a system to monitor the integrity of the storage canister. Sensor data fusion algorithms have been designed to predict the integrity of the storage system and provide feedback for preventative maintenance. The environmental conditions that lead to corrosion have been replicated and detected by the sensor system within an environmental chamber and the predictive model has been able to estimate the time till failure of a sacrificial corrosion sensor.

TABLE OF CONTENTS

LIST OF TABLES

LIST OF FIGURES

LIST OF ABBREVIATIONS

ADC	Analog to Digital Converter
BM	Base Metal
CZT	Cadmium Zinc Telluride
DOE	U.S. Department of Energy
EFA	Electrochemical Fatigue Admittance
EPRI	Electric Power Research Institute
FIB	Focused Ion Beam
FFC	Flat Flex Cable
GM	Geiger Muller
HAZ	Heat-Affected Zone
HPGe	High Purity Germanium
HSIL	Boise State Hartman Systems Integration Laboratory
INL	Idaho National Laboratory
ISFSIs	Independent Spent Fuel Storage Installations
NDE	Non-Destructive Evaluation
NRC	U.S. Nuclear Regulatory Commission
NWTRB	U.S. Nuclear Waste Technical Review Board
PCB	Printed Circuit Board
PDF	Probability Density Function
RTD	Resistance Temperature Detector

RTG	Radioisotope Thermoelectric Generator
SCC	Stress Corrosion Cracking
SEM	Scanning Electron Microscopy
SLA	Stereolithograph Apparatus
SNF	Spent Nuclear Fuel
TDR	Time-Domain Reflectometer
TOW	Time of Wetness
UNF	Used Nuclear Fuel
WM	Weld Metal

CHAPTER ONE: INTRODUCTION

On-site storage of spent nuclear fuel (SNF) at a reactor site was intended to be an interim step (<20 years) prior to transportation to a consolidated site. With the closure and uncertain future of the Yucca mountain storage facility, there is now an absence of permanent central repository for spent nuclear fuel or reprocessing scheme in the U.S. This has necessitated longer-term storage of spent nuclear fuel on-site or at distributed Independent Spent Fuel Storage Installations (ISFSIs). Licensing requirements of ISFSIs stipulate a storage period of 20 years with a potential for an extension of an additional 20 years were given in 1998 [1]. Fuel from reactors that came online in the 70's and 80's is now reaching the end of the licensing period, and hence, significant effort has been devoted to establishing the framework for safe, dry storage of the spent nuclear fuel beyond the original licensing period. Multiple U.S. agencies have made an effort to identify and characterize expected degradation modes at times beyond 20 years [2]. Current research and characterization of the spent nuclear fuel container degradation modes has revealed that corrosion is a potential mode of failure in the canister structure.

Following fuel burn up in the reactor, fuel assemblies are transferred temporarily to wet storage pools. The duration of time spent in wet storage is dependent on the amount of fuel burn up required to adjust the thermal profile of the SNF assembly such that the decay heat load is within specifications for removal. Conditions of sufficient cooling in wet storage are detailed in U.S. Nuclear Regulatory Commission (NRC) guidelines and require that the calculated fuel cladding temperature should not exceed

400˚C during normal loading or storage operations [3]. These temperature guidelines were enacted to avoid temperature dependent degradation mechanisms of the fuel and cladding, primarily hydride formation and subsequent embrittlement of Zr-based cladding alloys [4 ,5]. The actual cladding temperature is dependent on extent of fuel burn up, number of fuel assemblies in the canister, and effectiveness of the passive cooling of the dry storage system. After this wet cooling the SNF assemblies are dried and loaded into a dry storage canister that is sealed and back filled with helium. In typical SNF storage schemes the canisters are oriented vertically or horizontally and stored in individual or modular vented concrete structures (termed casks or overpacks). The concrete overpack provides containment and radiation shielding for the SNF canisters as well as passive cooling via strategically placed vents that enable decay-heat removal through convective air flow along the canister exterior surface. Figure 1.1 details these features on a vertical dry storage system.

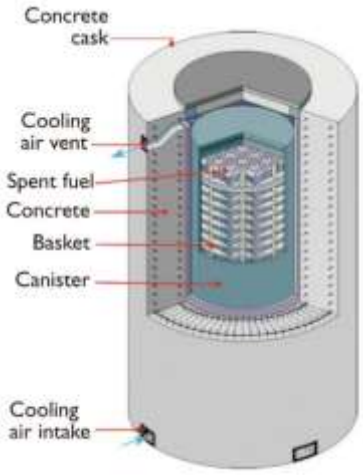

Figure 1.1. Vertical Dry Storage System. This figure shows the major components and locations of a vertical SNF dry storage system [6].

In order to ensure long-term canister health and safe storage of SNF, or should it need to be transported or retrieved in the future, it is necessary to know the condition of

the canister interior components including the fuel, cladding, moderators, and support assemblies. For example, prior to retrieving a fuel assembly from a sealed canister, it would be of interest to know whether a cladding breach or fuel rearrangement due to pellet degradation has occurred. However, the ability to remotely determine the condition of the SNF canister itself is of greater challenge and importance, since there are relatively greater potential consequences due to degradation of the primary confinement barrier. In addition to monitoring the environmental conditions and canister degradation modes, exterior canister monitoring can also provide information about the condition of the internals. Changes in the radiation and temperature profiles on the canister exterior are indicators of significant degradation of any internal components. Therefore, spatially resolved monitoring of the external conditions can be used to infer conditions on the interior, without breaching the container or placing a separate monitoring system in the very tightly-confined interior of the sealed canister.

Understanding the prominent expected failure modes is important when assessing the condition of the exterior side of the SNF canister while stored in a concrete overpack. Assuming a 304L or 316L stainless steel SNF storage canister is used, the primary degradation concern is atmospheric corrosion induced stress corrosion cracking (SCC) near heat affected weld zones on the canister exterior surface. These weld zones are established during container fabrication and sealing [7]. To verify container integrity, the optimal solution would be direct measurement of the weld zone corrosion evolution using electrochemical polarization or impedance spectroscopy in addition to non-destructive flaw detection such as guided ultrasonic waves for the presence of cracks [8]. However the complexity of implementing a full-scale direct assessment inspection for the entire

container and all circumferential (and longitudinal, if present) weld zones is prohibitive, expensive, and challenging. The implementation of such a system would not be conducive as a reliable, self-supported, long-term, or cost-effective monitoring system that will be available for near-term deployment.

System Deployments

ISFSIs normally place multiple canister systems in close proximity in a repeating geometric pattern such as a grid. A large number of canisters can be concurrently monitored by deploying sensor nodes across an entire storage facility. These sensor nodes communicate and report data via a wired or wireless sensor network with a central coordinator/receiver. This data is then transmitted by various means to a server with a sensor measurement database. This data can then be viewed by querying the database using various devices. Figure 1.2 shows a sample configuration of a deployed sensor network.

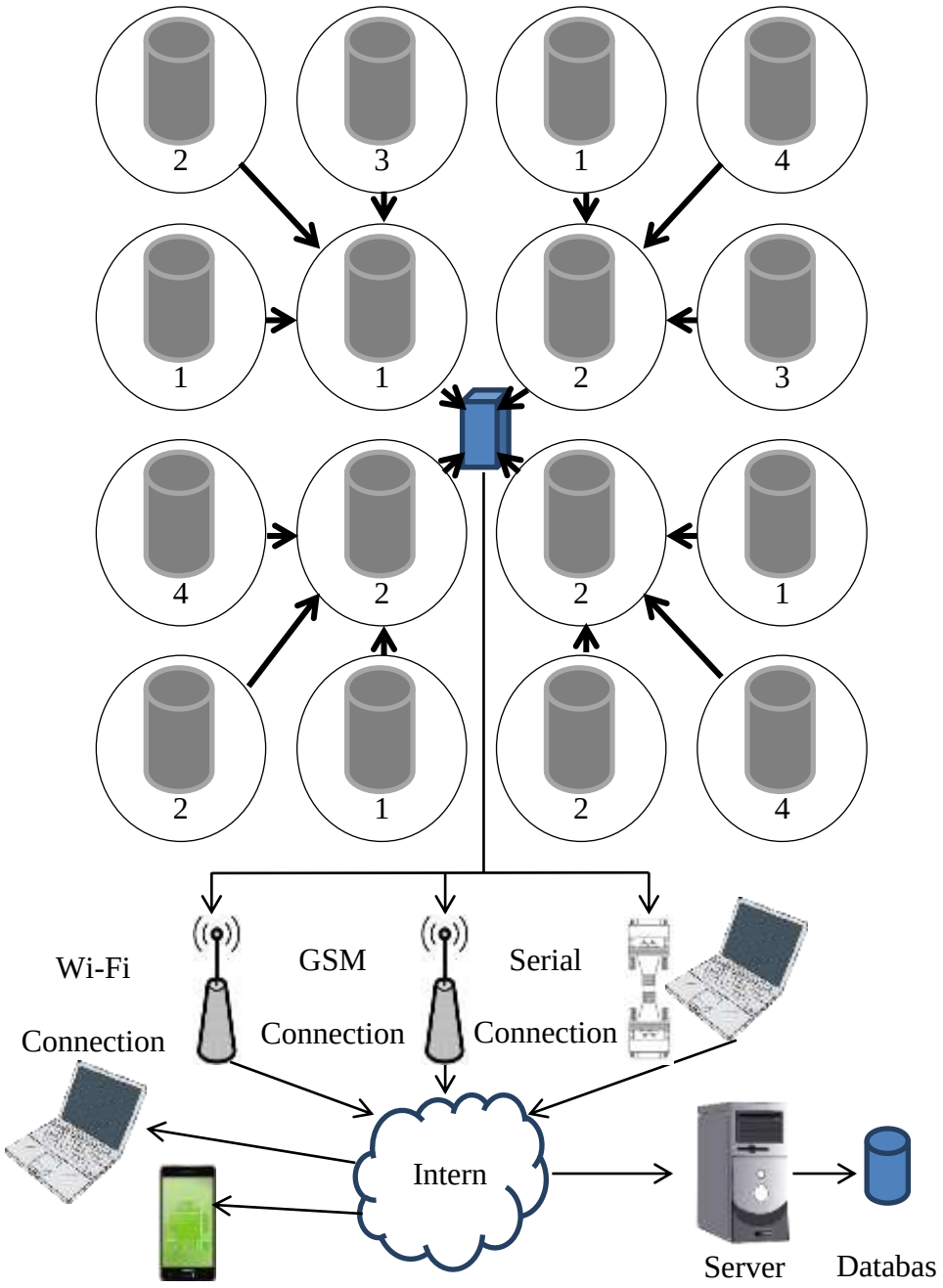

Figure 1.2. Example Sensor Network Configuration. This example network contains 16 SNF storage systems (grey cylinders) with a various number of nodes at each system. All of these nodes report to the central coordinator (blue box) which then manages the data by storing and/or transmitting it by various means to a server.

Each sensor node may communicate with the coordinator by wired or wireless means. If a wireless mesh network is implemented, such as a ZigBee network, adjacent nodes may “piggyback” transmissions across the network to reach the coordinator. This allows the network topology to be malleable and reduces infrastructure costs to implement the network. Sensor measurements taken at each node can be analyzed on the server side for events such as the presence of water, corrosive elements in the atmosphere, and changes in the corrosion sensors. If an abundance of corrosive elements and water are present, the odds of corrosion occurring increase. Predictive algorithms can detect data trends and predict the time of failure for each corrosion sensor element at each node. This can be used to prognosticly evaluate the health of an individual canister.

The contents of each canister can vary considerably, and therefore, the sensing needs may vary for each canister. In some instances a single sensor node can be used to monitor a critical location on a canister, such as the circumferential closing weld at the top of each vertical storage system. Figure 1.3.A shows a sample deployment of a single node designed to monitor a single closing weld by being placed in close proximity.

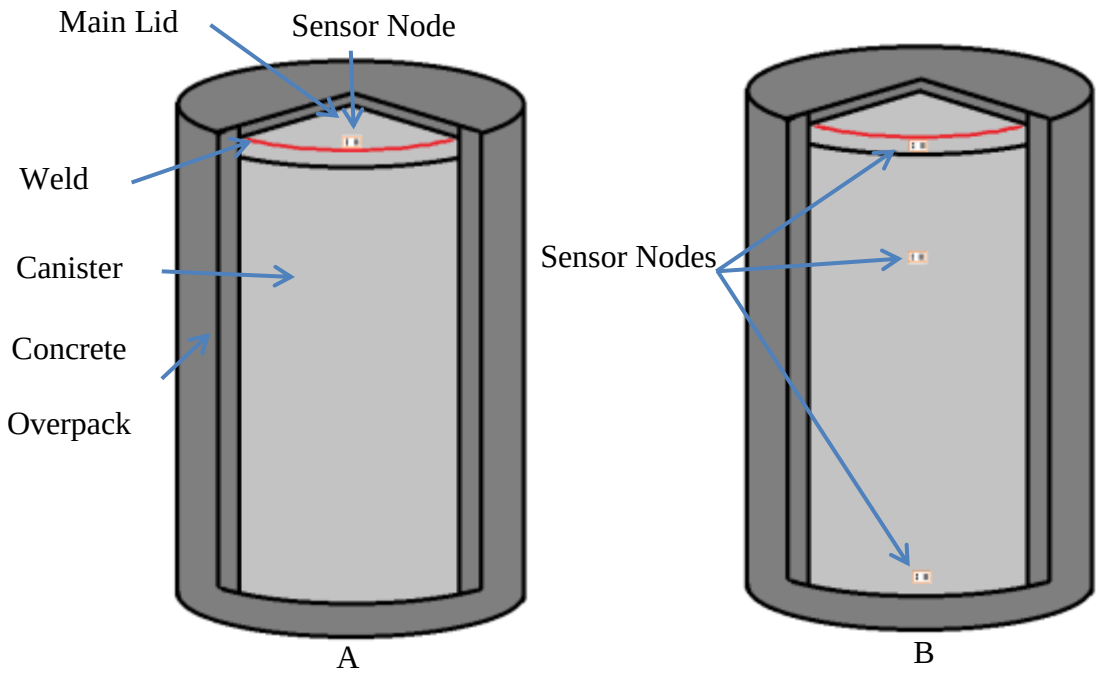

Figure 1.3. Single Sensor Node and Multi-Sensor Node Deployment. (A) shows the example deployment of a single sensor node near the closing weld (red line) of a vertical canister system. (B) shows the example deployment of a multi-sensor node system over the body of a canister.

Multiple nodes on a single canister have the ability to deduce information about the health of a SNF storage system that a single node could not such as the state of the internal fuel rod configuration. According to a report [9] released by the U.S. Nuclear Waste Technical Review Board (NWTRB) the location of hottest spot on the exterior of the steel canister in vertical storage systems upon initial loading is approximately two thirds the way up the canister. This is assuming the internal structure (see Basket in Figure 1.1) has not deteriorated and the majority of the SNF contained within has not fallen to the bottom of the canister. Should this occur, it is theorized that the lower sections of the canister would become hotter and that the canister would no longer be safe to move. This increased heat would also increase the rate of deterioration in the lower extremities of the canister [9]. An example sensor node configuration as depicted in

Figure 1.3.B would be able to monitor the temperatures at various points over the body of the canister, and over time, show a trend of moving peak temperatures that may signify internal deterioration.

Summary

This research seeks to enable a new set of applications through the creation of a SNF canister corrosion monitor, combining a cost effective corrosion sensor with commercial sensors, and a model to predict the integrity of the storage system. The dissertation focuses on three areas: designing a monitoring system, collecting corrosion data, and creating an event detection framework with models to monitor and predict the rate of corrosion in a stainless steel canister.

The creation of a corrosion sensor for prognostic monitoring of stainless steel SNF canisters is a novel combination and extension of existing work across multiple disciplines. The dissertation work builds on the following areas of embedded systems and environmental sensing:

- Corrosion detection of stainless steel using sacrificial sensors
- Environmental sensing in the local area of spent nuclear waste containment
- Event detection and notification in sensor systems

Motivations

There have been two recent events that have raised the global national awareness of the significance and need for safe storage of nuclear fuel. The first is the uncertain status of the proposed deep geologic repository at Yucca Mt., NV, which has re-opened the dialogue with the U.S. regarding used nuclear fuel (UNF) reprocessing as well as the strategy and potential selection for a real high level waste disposal site. This action has resulted in an increased amount of UNF stored at 75 sites across 33 states in the United

States [10]. Currently, the regulatory basis for dry cask storage is 60 years, but longer storage time will likely become necessary as the U.S. Department of Energy (DOE) and NRC evaluate repository and reprocessing components under the modified open cycle strategy. The open nuclear fuel cycle, or once-though nuclear fuel cycle, does not include the recycling and reprocessing of nuclear fuel, but rather stores the fuel for long periods of time before it is ready to reprocess should the need arise.

The second recent event is the ongoing cleanup at the Fukushima Nuclear Power Plant following the tragic earthquake and tsunami in Japan in March 2011. The efforts to clean and contain the serious radiological contaminants have revealed that the latent energy and radioactive materials contained in UNF must be controlled and safe guarded against conceivable and inconceivable events. The environmental effects of this incident can be detected around the world. Kelp off the cost of Orange County, California, had a 250 fold increase in Iodine 131 content which was traced back to the contamination caused by the disruption of the fuel storage pool in Unit 4, which contained UNF in the first stage of cooling [11]. The ramifications of the release of radioactive material into the environment are not limited to the local area in which it was released. Radioisotopes released from nuclear accidents can circumnavigate the entire world and persist for hundreds of years making complete clean up impossible.

The increased energy demand within the United States is pushing the nuclear power production industry towards higher and higher burnup fuel rates (>45GWD/t) which will increase energy production. This creates a UNF storage challenge as higher burnup increases cladding degradation, fission product concentrations, and other phenomena that will affect storage performance. High burnup fuel must remain in

cooling pools for longer periods of time, and once placed in dry storage, remain hotter for longer periods of time compared to traditional 30GWD/t fuel. This added heat exposure can lead to an increased rate of corrosion and expedite canister failure [12].

The Hanford Nuclear Reservation is currently the United States' largest repository of high-level nuclear waste by volume due to its history of weapons grade plutonium production. In 1977, the double walled storage tank AY-102 received a combination of liquid and solid waste for long term storage. Inspections of the tank occur on a visual 5 year cycle and an ultrasonic wall thickness test on an 8 to 10 year cycle. Corrosion monitoring probes are installed every 3 years and analyzed only on removal of the probe. In 2012 tank AY-102 experienced a leak between the inner and outer wall of the tank which had not been detected in its previous 2007 inspection. This tank is now under enhanced monitoring and investigation while its future is evaluated [13]. The long periods between inspections and corrosion tests did not allow the site technicians to preemptively service the tank before it leaked. What is needed is a prognostic and real time method of monitoring the storage tanks such that maintenance and inspections on said tanks occurs on a priority basis and not on a scheduled plan.

Contribution

Currently, there are no commercially available sensor systems for monitoring spent nuclear canisters. At the rate at which the number of new canisters are coming online, the need for this technology is only growing. Implementing any kind of system on a spent nuclear canister is performed under the highest scrutiny in order to ensure the safety of the public. By performing this research in cooperation with government agencies, it is possible to implement field testing which may not be readily available to

others. The work behind this dissertation is meant to open the door for enabling this type of sensor system to be commercially developed. To that end the following contributions were made.

Development of a Corrosion Sensor

The first contribution was the creation of a low cost, small form-factor stainless steel corrosion sensor that is designed to detect corrosion in a SNF canister. This specific approach used precision cut sacrificial sensor elements made of stainless steel (same alloy as the canister) which were placed in a fixture and placed under tension. A combination of thin and thick wires as well thin and thick strips was used as the geometry of each sensor. Each sensor element was placed under constant and calibrated tension and then exposed to the environment under test. While sensors of this type have been created previously [14], none have been attuned so specifically for the application of monitoring spent nuclear waste canisters.

Development of Circuitry to Monitor the Corrosion Sensor

The second contribution was the creation of circuitry capable of assessing the state of the corrosion sensors and quantifying the amount of corrosion that had occurred. This was accomplished by creating a series of high gain current amplifiers that interpolated the amount of current flowing through each sensor. Each current sensor gain was calibrated to the geometry of each sensing element and produced a value that was easily read by a microprocessor for evaluation. This type of circuity for this specific application is to the best of the author's knowledge novel.

Development of Application Specific Sensor Fusion Algorithms

The third contribution was the creation of a sensor fusion algorithm that adjusted the readings taken from the corrosion sensing elements for environmental factors. These factors included temperature, humidity, condensation, and presence of corrosive material. These sensor fusion algorithms increased the reliability of the data acquired from the corrosion sensors and reduced environmental error.

Development of a Application Specific Prognostic Algorithm

The fourth contribution was the creation of a prognostic method that determined the probability of a corrosion sensor element's failure within a given time. By using current and previous data gathered by the sensors, and by using experimental and theoretical corrosion curves, an evolving probability density function (PDF) was generated for each individual sensor element. This PDF was used to estimate the probability of when a sensor element would fail by integrating the function over the time span in question. This function, being so specific to this application, is to the best of the author's knowledge novel.

The work in this dissertation was, in some cases, the result of a collaboration of several students working in an area. This was true where expertise was required that lay outside of the author's field (e.g. material science). The development of the corrosion sensor and the housing was performed in conjunction with material scientists, a mechanical engineering student, and the author. The circuitry, firmware, PCB design, and assembly techniques used to drive and monitor the various sensors were performed by the author. The sensor fusion and prognostic algorithms were built upon existing works [15], but were molded by the author for the specific application of monitoring for corrosion.

The remainder of this dissertation discusses previous work (Chapter 2), the conducted research (Chapter 3, 4, and 5), results (Chapter 6), research to be completed (Chapter 7), and conclusions (Chapter 8).

CHAPTER TWO: PREVIOUS WORK

The use of sacrificial sensors to monitor corrosion is by no means a novel concept. The connection between the conductivity of the sacrificial electrode and how it changes as it corrodes has been well established in both literature and in industry practice [14]. There are many applications for this type of technology in both the structural monitoring arena as well as preventative maintenance. However, in the application of detecting stress corrosion cracking in stainless steel in particular, there are fewer viable technologies. When specifying to the use of corrosion sensors in the nuclear storage field, there are no field deployable systems. Corrosion has been extensively researched when it comes to its effects on spent nuclear fuel canisters by the Electric Power Research Institute (EPRI) [16,17] as well as Idaho National Laboratory (INL) [18].

In 1990 EPRI released a report on a series of experiments designed to initiate SCC on stainless steel samples (as well as many other materials) and to detect cracks using Electrochemical Fatigue Admittance (EFA) [16]. The stainless steel samples were placed in a stress inducing load cell and coated with various acids which initiated the cracks. A potentiostat was attached to the load cell, and the sample and was monitored by a Digital Multimeter (DMM). The resulting analysis showed that SCC could be detected using EFA, but according to the test procedure, the sample would need to be removed from its source in order to test it for cracks [16].

In a 2014 report [17] concerning the inspection for SCC on two spent nuclear fuel containers at the Calvert Cliffs Nuclear Power Plant, EPRI performed visual inspections,

collected surface samples, and surface temperature measurements. The visual inspection found large amounts of dust had settled on the canister and a few rust blooms had appeared on the exterior of the steel. The surface chloride concentration had been found to be rather low at less than $0.1 g/m^2$, which is indicative of a rain water environment rather than a sea water environment. This is interesting itself, because the canisters were stored less than half a mile from the Atlantic Ocean. The report continues to state that it has been determined that SCC can occur under extreme conditions, but such conditions may not be indicative of actual in-service conditions. What is not understood in this report is what the actual in-service conditions are [17].

Sensor systems have been placed onto spent nuclear canisters to collect long term data and detect internal corrosion. INL developed a sensor system to monitor the inert gases within the canister for xenon [18]. When a steel canister is sealed it is pumped full of helium to prevent atmospheric chemical reactions. Two of the radioactive products of the irradiated fuel pellets are xenon and krypton gas. By routinely sampling the helium gas for xenon gas concentrations, the status of the internal fuel and cladding can be determined. Other sensors were placed on this unit including relative humidity and radiation, and the results were sent back to a base station via a radio link. The components inside the sensor system were not radiation resistant, so a half inch of machine grade tungsten was used to shield the components against a potential radiation dosage of 500 R/hr [18].

SCC has been studied extensively by researchers at Los Alamos National Laboratory, where in cooperation with the University of Southern California, a hierarchical petascale simulation framework for stress corrosion cracking has been

developed [19]. This system uses scalable computer resources to create multimillion-to multibillion-to multitrillion atom molecular dynamics (MD) simulations of certain metal lattices. These simulated lattices are subjected to a stress and exposed to simulated corrosive elements which results in SCC which can be monitored on the atomic level. Using this software, the exact mechanics of how crack growth begins and propagates has been simulated with a variety of materials, corrosive catalysts, and corrosion inhibitors. These results are promising, but there are still questions to be answered regarding temperature dependence and how liquid and solid atoms interact within the simulation [19].

There are several sacrificial corrosion sensors available on the open market [14]. These sensors are based on the fundamental concept that the action of corrosion on an exposed metal element will reduce the cross-sectional area of the element, thereby increasing its electrical resistance. The value of the resistance increases in a predictable manner with depth of corrosion, thereby permitting the accurate determination of the metal loss occurring. One such sensor is manufactured by Corr Science which uses a spiral geometry shown in Figure 2.1 below.

Figure 2.1. Corr Science Corrosion Probe. This image shows a rendering of one of the corrosion probe geometries made by Corr Science [14].

The spiral geometry maximizes the amount of surface area of the sacrificial element which can be used to detect a 1-2 nm loss of material from a 0.5mm thick sensor due to corrosion. In testing, using a 10 hour exposure test of a probe to a 1% solution of sodium chloride, a metal loss between 10 and 10.5 nm/hr was measured.

Compact corrosion sensor solutions are also available on the market and are targeted towards monitoring specific alloys in server farms [20]. Jointly developed by IBM and iButtonLink, replaceable and sacrificial corrosion sensor coupons that integrate into a wired or wireless network system have been used to monitor electronics. These corrosion coupons use copper and silver wafers, which are the most commonly used metals inside electronics and are the most vulnerable to corrosion damage. The corrosion coupons are constantly measuring and monitoring the changing levels of sulfur and nitrogen dioxide (CO2, SO2), which directly influence the rate of decay in electronics. The sensor software provides users with a 3D floor-to-ceiling view of a facility space, including environmental factors such as humidity, corrosion, hot spots and others that

could be disrupting applications. This solution is very similar to the one provided in this dissertation, but lack the targeted alloy, multiple sensor geometries, as well as the needed environmental considerations [20].

CHAPTER THREE: SENSOR MODULES

Based on previous work completed by the Boise State Hartman Systems Integration Laboratory (HSIL) [21], the clear initial design challenge was to create viable sensor interfaces for the various sensors. In order to expedite prototyping, each sensor was integrated into an Atmel based microcontroller prototyping board created previously by researchers in the HSIL. This prototyping system includes a 32-bit microcontroller, a wireless Zigbit radio, visual and auditory feedback (a piezo buzzer and tricolor LEDs), and several debug and serial interfaces. Each of the designed sensor modules must work together to achieve the sensor system's mission and, therefore, must conform to the standards required by the sensor motherboard. Table 1 shows the sensor type and the intended interface.

Table 1. Sensor Type and Interface. This table shows the types of sensors integrated into the sensor system and the standard interface protocol for each.

Sensor Type	Sensor Interface
Temperature	ADC, 1-Wire
Humidity	ADC, 1-Wire
Radiation	Digital Counter
Time of Wetness	ADC
Corrosivity	ADC

Temperature

There are two types of acceptable sensors for measuring temperature in this system: K-type thermocouples and platinum resistance temperature detectors (RTD). K-type thermocouples can measure temperatures between -200 ˚C and 1350 ˚C and can be made to be highly corrosion resistant for long term deployment in the field. Additionally, the chromel-alumel junction that creates the thermocouple junction can be placed away from the senor interface circuitry via the thermocouple wires. This means that the circuitry can be placed in a central location, and multiple thermocouples can be employed to measure various locations across the canister. Platinum RTDs come in integrated circuit form and can monitor the internal temperature of the sensor system by being soldered to the motherboard. According to Gonzalez-Guerrero et al. [22], IC-based thermometers degrade and their sensitivity drifts as they are exposed to neutron and gamma radiation while thermocouples and Platinum RTDs remain stable and reliable up to a total ionizing dose of 60 krad. However, because of the versatility and superior noise filtering offered through thermocouple instrumentation, external RTDs were not further considered for the current version of the sensor system.

Thermocouples use two dissimilar metals joined together at an interface. As the temperature changes at the interface, a voltage is generated (Seebeck effect) which can be routed through the thermoelements. As long as the interface metals are physically and chemically isolated from the environment though a thermally conductive medium, the thermocouple will continue to function in extreme environments. The generated voltage must be amplified with an instrumentation amplifier that has been precalibrated for use with thermocouples. This type of amplifier normally includes a cold junction

compensation temperature sensor on chip, which compensates for the differences in temperature at the measurement interface and the reference interface. The reference interface is made of a different metal then the thermocouple leads and the printed circuit board (PCB) board which creates two additional thermocouple interfaces. In order to get around this problem, both interface terminals are kept as physically close as possible and kept as far away as possible from high wattage devices on the PCB. This will result in the additional SeeBeck effect voltages created by these new metal junctions canceling each other and only reporting the voltage found at the desired thermocouple. An additional consideration when using long thermoelements is the filtering of high frequency noise coupled onto these long leads. The long leads function as an excellent antenna and may pick up unwanted signals, therefore a low pass filter with a low corner frequency will allow only the correct input signal to pass through undiminished. Figure 3.1 shows the full implementation of the circuitry.

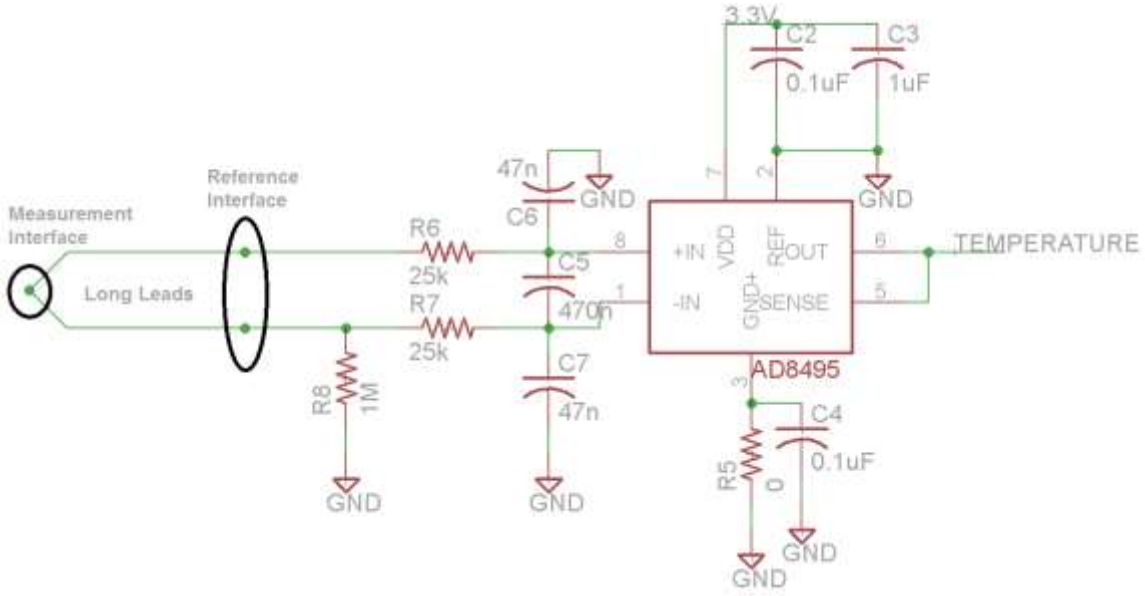

Figure 3.1. Thermocouple Circuitry. The circuit shows the thermocouple, low pass filter, and the cold junction compensated instrumentation amplifier.

The equation to calculate the cutoff frequency for the low pass filter is as follows [23]:

$$Filter\ Frequency(Hz) = \frac{1}{2\pi R(2C_D + C_C)}, \quad \text{Equation 3.1}$$

where C_D = 470nF (C5 in Figure 3.1), C_C = 47nF (C6 and C7 in Figure 3.1), and R = 25kΩ (R6 and R7 in Figure 3.1). This resulted in a cutoff frequency of 6.45 Hz.

The temperature signal, when using the AD8495 IC, reports an analog value such that every 5mV is equal to 1 ˚C. If this IC is attached to a 12-bit analog to digital converter (ADC) (4096 analog combinations), it will allow a temperature resolution of 0.161133 ˚C by Equation 3.2.

$$Resolution = \frac{V_T}{\frac{V_A}{2^{Bits}}} = \frac{5mV}{\frac{3.3V}{2^{12}}} = 0.161133, \quad \text{Equation 3.2}$$

where V_T is the number of volts reported per degree C, V_A is the analog voltage range (3.3V in the current system), and bits is the bit resolution of the ADC.

Humidity

Temperature and humidity are the two atmospheric conditions that contribute to whether or not corrosion activity on the canister surface may occur. Monitoring these conditions alone will allow prediction of the onset and duration of possible corrosion activity on the canister surface. Many types of cost-effective humidity sensors are widely commercially available. However, very few meet the requirements of the environment in which they need to function. Capacitive sensors are preferred for their resolution over resistive humidity sensors and are also more corrosion resistant. Capacitive humidity sensors consist of a hygroscopic dielectric material sandwiched between a pair of electrodes forming a small capacitor. The properties of the capacitor vary depending on the dielectric constant of the material used and the dimensions of the sensor. As water

vapor interacts with the hygroscopic dielectric, the effective capacitance of the sensor changes, which results in a reading of absolute or relative humidity (depending on sensor calibration). The majority of these sensors have a 0% humidity capacitance in the pico-Farad (pF) range, which would require a variety of different driving frequencies in order to properly read them. In order to test a variety of these sensors a custom humidity driving board was created (Figure 3.2) which could vary the driving frequency and voltages applied to the sensor as well as calibrate it with a precise standard humidity meter.

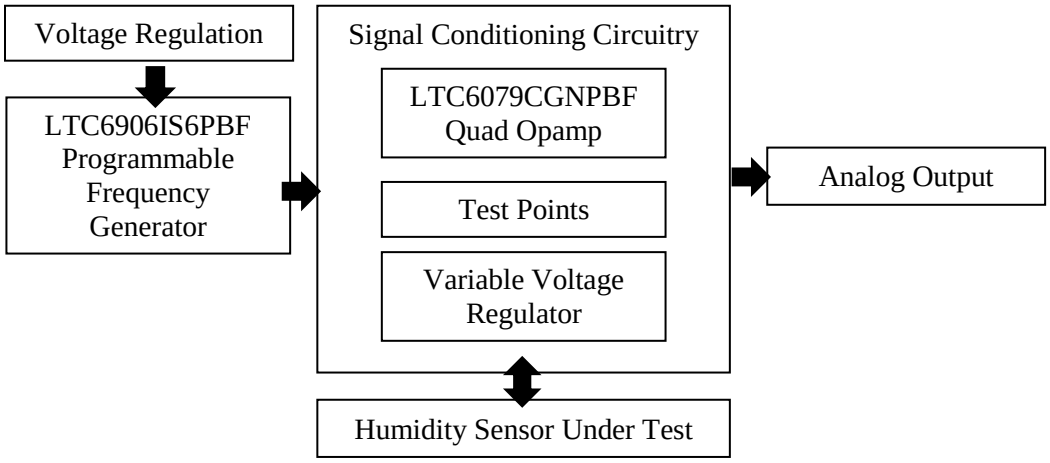

Figure 3.2. Humidity Sensor Driver. The circuit block diagram shows the oscillator and amplifier circuitry used to drive and calibrate humidity sensors.

It was quickly discovered that each sensor element of similar make and model required calibration values that in some cases were vastly different. This is primarily due to manufacturing differences and variations in the dielectric. Prepackaged sensors are calibrated in factory, contain the appropriate driving circuitry, and have standardized interfaces such as a simple analog output or Dallas One Wire. This makes them the better candidate for a system that needs to be mass manufactured and reduces error due to

miscalibration. The amount of board level circuitry is also reduced which shrinks the volume of the entire design and generally results in an improved signal to noise ratio.

For preliminary testing the HIH-4030 Honeywell relative humidity sensor was used as it was an all in one chemically resistant surface mount sensor. This sensor produced a near linear voltage to %RH signal that could be read on an ADC. For lab tests, this sensor performed well, but its small size and surface mount nature made it very difficult to place into assemblies exposed to the atmosphere. Should condensation form on the sensor, then the humidity readings would become inaccurate until the sensor dried out again. This resulted in a search for a more robust sensor that was immune to dew point or frost point issues. The RHT03 [24] sensor from MaxDetect was selected as it is commonly used in green house monitoring. An advantage to this sensor is it that it contains a local temperature sensor that can be used to help predict dew and frost points and that it is made to be mounted up to 100m from its host microcontroller. The communication scheme is also digital (similar to Dallas one wire), therefore signal to noise ratio issues are removed and fewer filtering capacitors need to be used on the board.

Radiation

The thick walls of the inner steel canister are unlikely to allow alpha and beta radiations to penetrate. In the event of containment breach, in which case all forms of radiation would be present, the level of gamma would increase significantly along with the levels of alpha and beta radiation. A sharp rise in the amount of gamma radiation would be a significant indicator of canister failure, and if multiple sensor units are deployed, allow for some degree of triangulation of the radiation source.

The temperature in the annulus surrounding the canister may be as high as 200-250 °C. This parameter significantly restricts the choice of radiation sensors as the majority have operational temperatures well below this threshold. There are several solid-state sensors used for detecting radiation including Cadmium Zinc Telluride (CZT), High Purity Germanium (HPGe), or Silicon. However, these sensors require room temperature or even cryogenic temperature conditions to function, and the sensors will also run into complications at the anticipated radiation intensity. In some cases, such as when using CZT sensors, the thickness of the sensor determines the range of energies that can be detected (thicker crystals can detect higher energies). At this point, the anticipated radiation level is expected to vary depending on canister type and fuel load, so it is difficult to specify a device thickness beforehand [25]. Another solid-state solution using the structural reorganization of Ag doped Ge-S chalcogenide glasses under a radiation environment is currently under investigation by Mitkova et al. [26]. They find the resistance of the devices decreases with an increase in radiation which would be ideal for low power systems. This technique is still in its infancy but may prove to be a useful technology since the sensor size would be very small and the electronics required to drive the sensor would be minimal. This is, of course, depends on the final operating temperature of this type of sensor.

The current solid-state or thin film detection technologies are limited by their environmental stability and/or maturity and, hence, were eliminated from consideration in our monitoring system. This means that a non-solid-state sensor needed to be adapted for this system. Geiger Muller (GM) tubes are gas filled radiation detectors that measure the ionizations created by radiation interactions with the sealed tube. In the simplest form,

the detector is a cylindrical sealed tube composed of a cathode (the thick cylinder wall), an electrically isolated anode (a wire that is supported down the centerline of the cylinder), and filled with a low pressure (approximately 50-100 torr) noble gas such as neon, argon, helium, or krypton [27, 28]. A potential is applied across the anode and cathode such that when an ionization event occurs in the gas due to radiation, the ion and electron will separate rather than recombine. If the potential is high enough, a cascade occurs due to the accelerating particles and produces secondary and tertiary ions and electrons. These move to the cathode or anode as well and provide the necessary level of charge for detection. In general, low energy X-ray or gamma rays produce ions through a photo-ionization mechanism directly with the gas atoms while high energy radiation types ionize the gas through electrons ejected by photo-emission from the inner surface of the cathode tube wall. Typically, there is a small amount of halogen gas inside the tube, called the quencher, which deionizes the noble gas after a cascade event. The halogen gas has a lower ionization potential than the noble gas, so it readily gives up an electron to the cation and eventually deionizes itself when it comes in contact with the cathode [29].

LND Inc manufactures a GM tube that can operate in the expected environment. It is 158 mm long with a diameter of 16 mm. It is constructed of a 446 stainless steel body and filled with Ne, with a small amount of a halogen gas (not specified) as a quencher. The interior of the body is plated with Pt in order to enhance the production of photo-electrons from the wall during a radiation event. This sensor provides the best available solution to survive the operating conditions and provide acceptable radiation level data. However, as of our last request, LND is unwilling to sell this specific sensor

for research purposes and will only accept large volume orders. Therefore, a similar tube with similar electrical characteristics was purchased from LND for proof of concept and experimentation [30].

The selected GM tubes require voltages between 850-1200V to operate with a recommended voltage of 900V. This voltage is generated using a 5V DC source and a modified Villard Cascade multiplier with a 1:1 isolation transformer. Using an RC transistor oscillator attached to the primary winding of the transformer, an AC voltage can be generated on the secondary side to excite the multiplier and provide the required voltage to the GM tube. When the tube generates a pulse, it is fed into a high voltage transistor which reduces the signal down to 5V. This signal is then fed to a comparator to square and buffer the pulse resulting in a digital signal that can be fed into a microcontroller or a simple digital counter. In this case, the comparator can also be used to drive a simple Piezo buzzer which produces the iconic clicking noises associated with Geiger counters. Figure 3.3 shows the circuit block diagram used to drive the GM tubes as stated above.

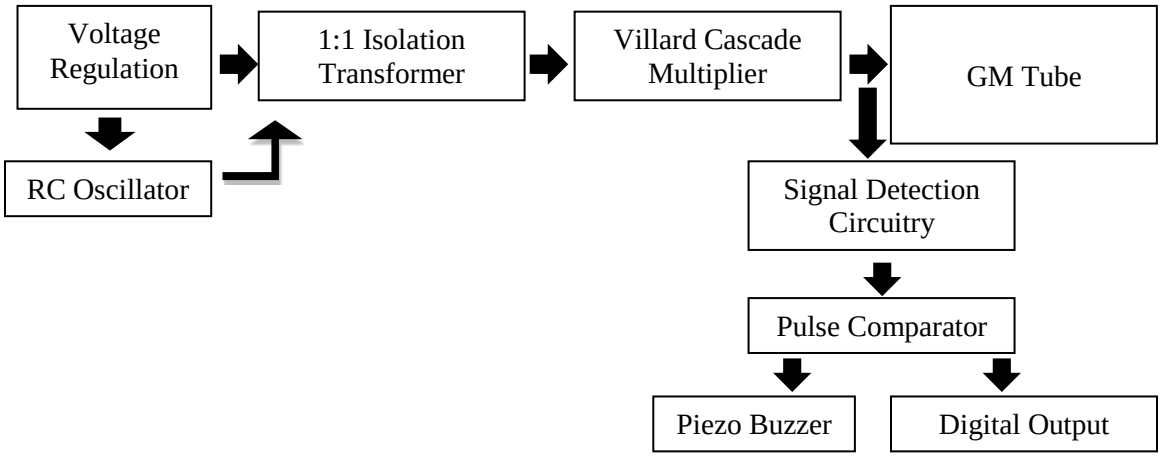

Figure 3.3. GM Tube Driver. The circuit block diagram shows the isolated AC voltage generation, voltage multiplier, and signal conditioner of the GM tube driver.

An important note for the PCB layout of this type of circuit is the careful physical separation of each of the high voltage traces in the multiplier and beyond. The high voltage components are, in this case, through hole components, which provide the required isolation between each stage of the multiplier. TVS diodes as well as high voltage low value capacitors placed at the input and output terminals of the driver circuit will prevent switching noise from compromising the rest of the sensor system.

Time of Wetness

As humidity and temperature fluctuate over time, favorable conditions will be encountered where moisture can condense on the surface of the container forming an electrolyte layer, allowing corrosion to occur. This is an expected primary source of SNF canister degradation stemming from the atmosphere surrounding the canister [31]. In order to measure the time that the canister is susceptible to atmospheric corrosion, a time-of-wetness sensor is included in the sensor system. This sensor measures the amount of time when an electrolyte layer is present and the canister, is therefore, potentially susceptible to corrosion activity. A threshold for dry conditions must first be established as a baseline, and then the sensor outputs data any time a measurement is made and the threshold is exceeded. The output signal may be voltage, current, or resistance/impedance [31].

A time of wetness (TOW) measurement contains two separate parameters, an environmental parameter and a surface parameter. The environmental parameter measures the conditions around the canister, such as humidity and temperature, and measures the “wetness” as the time the humidity is at 80% or higher at a temperature greater than 0 °C [32]. The surface parameter can be measured two ways. The first

method is to use two noble metals and measure the time that a liquid bridges the gap between the two metals. The second approach is to have two non-noble metals that act as a galvanic corrosion monitor. As a liquid electrolyte is formed between the two metals, corrosion occurs, and duration of corrosion activity is measured [32].

Several iterations of time of wetness sensors were tested or created before the final choice was made. A Campbell Scientific 237 Leaf Wetness sensor was obtained for initial testing of this type of sensor. Figure 3.4 shows this sensor and its inter-digitated comb design.

Figure 3.4. Campbell Scientific 237 Leaf Wetness Sensor. Time of wetness sensor using a noble metal inter-digitated comb design.

As water droplets accumulate or as a full electrolyte layer forms on the comb, the resistance between each electrode changes. Monitoring this change gives a real time indication of the status of the surface of the canister. Unfortunately, the Campbell Scientific sensor had several physical and electrical inconveniences for an application within the scope of this sensor platform design. The first step in eliminating these issues was to reverse engineer the sensor to solve the electrical problems experienced such as noise and poor sensitivity. The comb section was replicated on a LPKF circuit board

plotter to match both the dimensions and comb spacing of the Campbell Scientific module as shown in Figure 3.4. The electronics were also altered to include an accurate 2-stage amplifier to improve the signal to noise ratio as well as reduce the required current to run the sensor down to less than a milliamp (mA). These changes are shown in Figure 3.5.

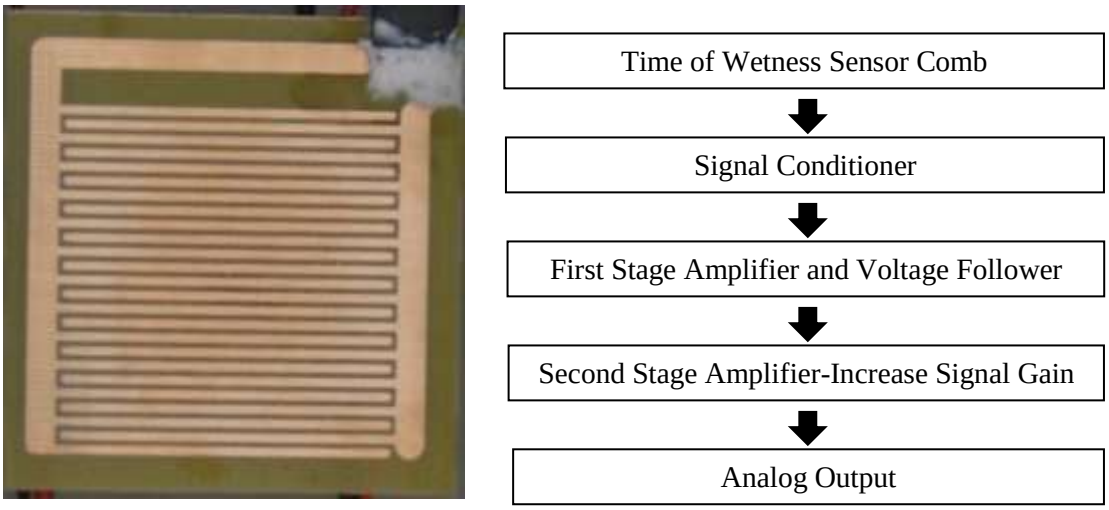

Figure 3.5. Custom Time of Wetness Sensor. Time of wetness sensor redesigned with new comb to improve signal quality and reduce power.

Several nondestructive tests were run to confirm the accuracy of the sensor and the accompanying electronics. Figure 3.6 shows the data gathered from dropping approximately 0.25 mL of DI water directly onto the sensor and allowing it to evaporate.

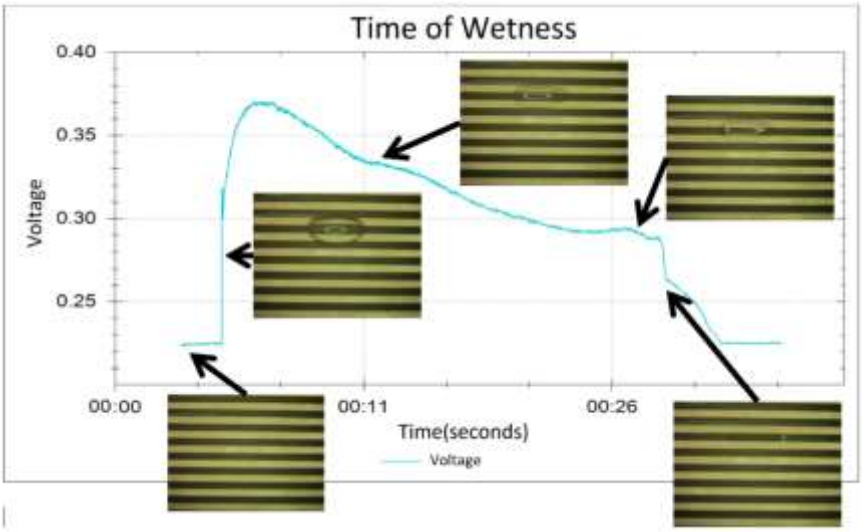

Figure 3.6. Custom Time of Wetness Sensor Drop Test. Graph shows the voltage (Y axis) output as a single drop of water is placed on the sensor and its evaporation over time (X axis).

The sensor in its dry state puts out a low level voltage of 13mV, but when excited by a drop of water quickly increases to 37mV. As the drop evaporates the surface tension collapses, and the drop spreads out resulting in a slow decline in voltage, followed by a sharp decrease, ending with the sensor returning to the dry state.

The physical inconveniences of the sensor comb are apparent. The redesigned comb measures 2.5 inches by 2.5 inches which is a very large surface area and would most likely dictate the physical dimensions of the final sensor system. The copper in the comb would also become corroded over time which would result in skewed data and loss in sensitivity. A smaller comb covered in a noble metal would be required to implement this sensor in the field. Silver was chosen as the noble metal for price and availability reasons, and the comb was reduced to 2.5 inches by 1 inch. However, the apparatus to easily deposit an even layer of silver onto this new copper comb was unavailable as molten silver tends to form a meniscus over the comb traces as shown in Figure 3.7.

Figure 3.7. Smaller Custom Time of Wetness Sensor with Silver. Smaller redesigned sensor comb with silver melted onto each comb to prevent corrosion.

These defects in the silver coating would increase the chances of electrolyte buildup between the combs giving a skewed sense of the rate of corrosion. The solution to this problem was found at Case Western Reserve University which produces inter-digitated combs for sensor applications. A variety of combs of different sizes and materials were selected and tested, and the final choice was a gold comb on an alumina substrate. This sensor comb measures 0.6 inches by 0.6 inches which provides an excellent space savings. Figure 3.8 shows a drop test with this new comb.

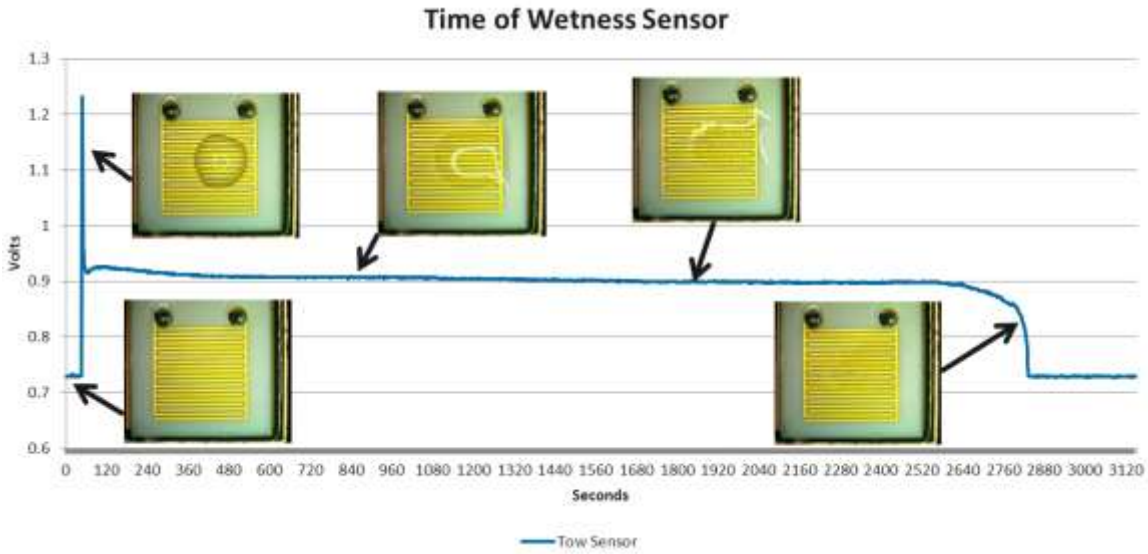

Figure 3.8. Gold on Alumina Time of Wetness Sensor Drop Test. Graph shows the voltage (Y axis) output as a single drop of water is placed on the sensor and its evaporation over time (X axis).

The comb spacing on this sensor is much tighter than that of the previous version which provides additional sensitivity to small levels of moisture and electrolyte buildup. There is also a sharper roll off in this sensor as the drop evaporates which is more indicative of a wet or not wet environment.

Corrosivity

Humidity and time of wetness strongly influence the atmospheric corrosion rates of a canister, but in order to measure the chemical corrosivity on an environment a corrosivity monitor is required. The chemical composition on the atmosphere can exacerbate the rate of corrosion caused by moisture. Because of the proximity of the ocean, dry storage installations sited in coastal regions will be exposed to different and more severe corrosion conditions than sites located far in-land where the composition of the airborne particulates and aerosols is less influenced by the sea. Relative corrosivity data will provide an indication of the potential influence of atmospheric composition on corrosion rate. Similar to the previously described inter-digitated time of wetness sensor,

a corrosivity sensor has the ability to sense when an electrolyte layer forms on the surface. However, due to the dissimilar electrode materials selected and trace geometries of the electrodes, it is also able to indirectly assess the relative severity of the corrosive atmosphere.

A corrosivity monitor works by placing two dissimilar metals in near proximity to each other, but isolated from each other by an electrical insulator. When the atmosphere promotes formation of an electrolyte layer on the surface of the sensor, the insulator gap may be bridged, and the two dissimilar metal electrodes become electrically connected. As a result, a galvanic couple is formed which generates a potential and allows for the flow of a corrosion current. The resulting corrosion current is dependent on the aggressiveness of the environment, with more severe environments creating a greater corrosion current [33]. If the base metal (anode) is selected based on the canister system of interest and the conductive layer (above the insulator) is a noble metal, the corrosion current will correspond to a corrosion rate of the base metal under galvanically driven corrosion conditions [34]. The sensor is not able to identify either the specific electrolytes or their concentrations only a measure of the relative aggressiveness of the environment. However, this sensor provides information on the potential corrosion rate of the canister that would not be available from the temperature, humidity, and time-of-wetness sensors alone since data from those sensors will only allow a prediction of when corrosion activity is possible or not.

For the corrosivity sensors deployed in the sensor system, the substrate would be a thin (<1mm) carbon steel or a stainless steel (depending on the specific canister being monitored) and the noble metal would be a thin silver layer. A commercially available

corrosivity sensor constructed with a carbon steel anode and silver cathode was procured and proof tested. The electrical characteristics were obtained over a period of seven days under very aggressive, constant immersion, saltwater conditions. The appearance of the corrosivity sensor surface before and after immersion is shown in Figure 3.9.

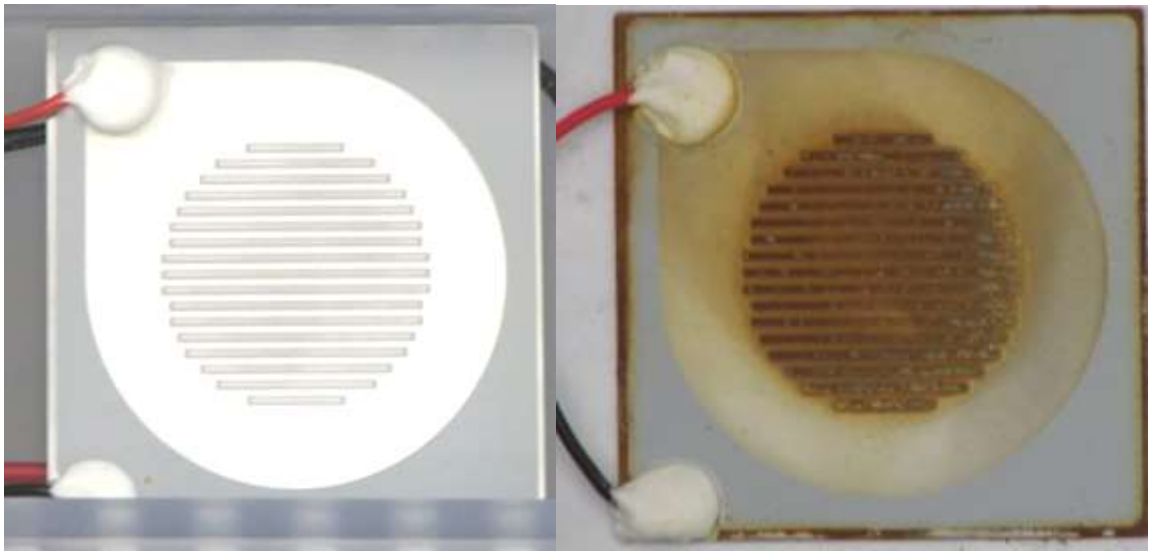

Figure 3.9. Corrosivity Sensor Before and After. Dissimilar metal corrosivity sensor before (left) and after (right) a 7 day exposure in a super saturated salt water bath to test the electrical output characteristics over the corrosion period.

This sensor was used in early development of the sensor nodes, but was found to be far too large and cumbersome to design into the cases of the nodes. During the research work it as surmised that the only way to fix this problem was to build a custom corrosivity sensor using the same materials only smaller in size. Luckily, before that process began, the original manufacture of the sensor released a smaller version. The old corrosivity sensor measures 2.5 inches by 2.5 inches, and the new sensor measures 1 inch by 0.85 inches. Figure 3.10 shows the size comparison.

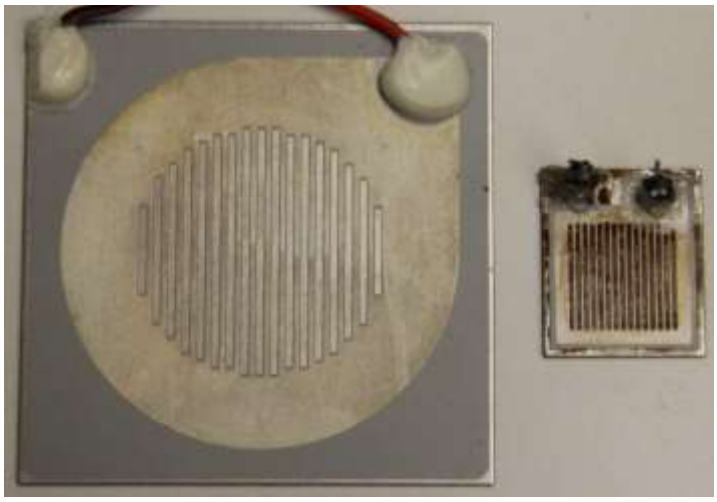

Figure 3.10. Atmospheric Corrosion Sensor Size Comparison. The Sensor on the left is the old larger sensor and the sensor on the right is the smaller new sensor. Both of these sensors have undergone destructive testing and are corroded.

The small size of this sensor and the need to compress the electronics further has created the need to develop a new current sensor board made just for reading galvanic sensors. The circuitry for this sensor was vastly simplified by using the LOG101 IC from Texas Instruments which allows decade based logarithmic current measurement inside one IC. The PCB on which this circuity resides also supports and helps mount the new smaller sensor. Figure 3.11 shows the new circuit and the mounting PCB for the new sensor.

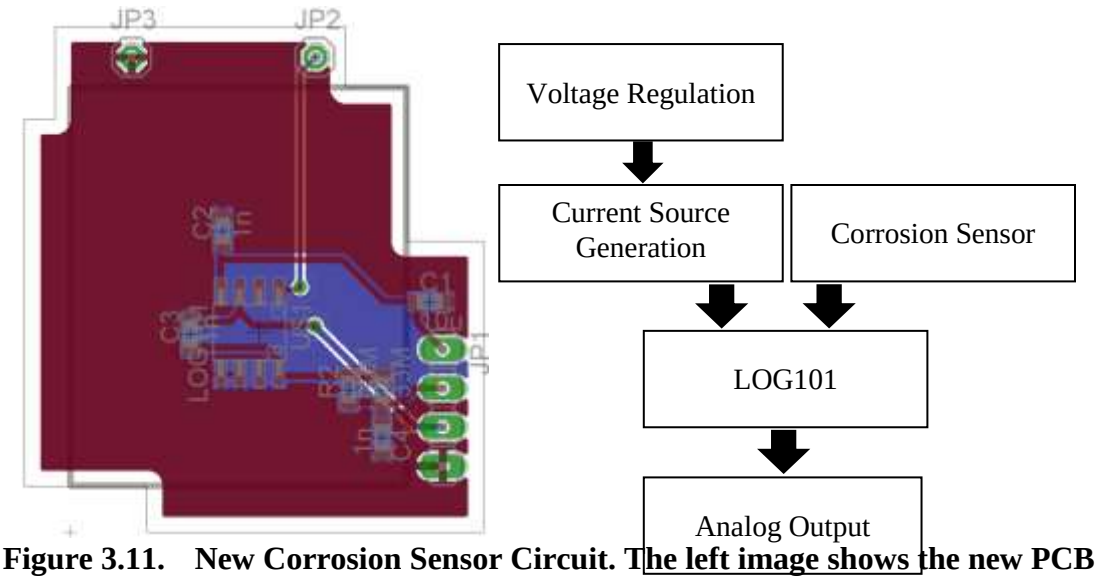

Figure 3.11. New Corrosion Sensor Circuit. The left image shows the new PCB board and the outline of the new atmospheric corrosion sensor. The image on the right shows the circuitry block diagram for the PCB in the image on the left.

Early destructive testing of this new sensor on this PCB was conducted and the results are shown below in Figure 3.12.

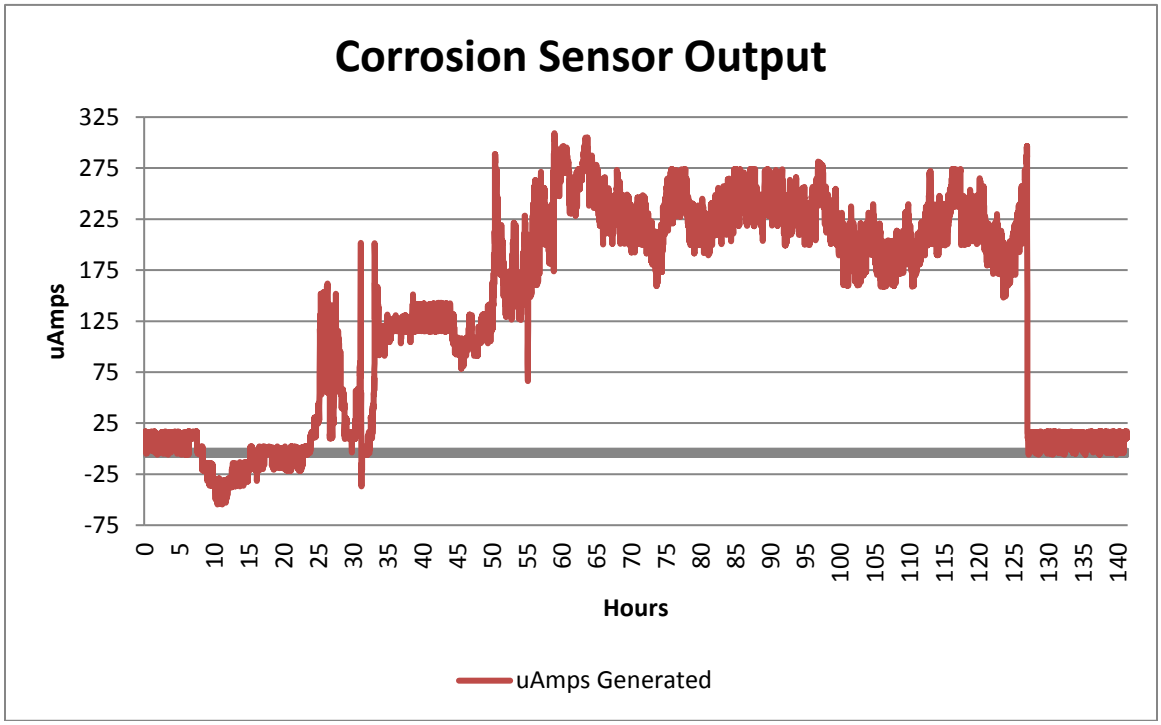

Figure 3.12. New Corrosion Senor Test. The graph shows the corrosion sensor test data from a destructive test of the sensor over a six day period.

In this test the sensor was submerged in a sea water solution (33 parts NaCl per thousand) and allowed to corrode until it failed approximately eight days later. Once the sensor fails, the current generated drops off completely, and no more useful data can be collected. Data for this sensor is best represented as an accumulated value or integrated current over time.

Corrosion Sensor

To meet the specific corrosion sensing needs for the welded stainless steel container, a novel sensor was needed. The primary sources of dry storage canister degradation are expected to be corrosion of the welded lid region and atmospheric induced pitting or crevice corrosion of the container wall. The other environmental sensors mentioned above will allow an estimation of when and how fast corrosion is occurring, however the novel indirect-assessment corrosion sensors will provide complementary information on the actual extent of corrosion from identical container materials including the complex influence of weld metallurgy. These canister materials include 304, 304L(N), 316, and 316L(N) type stainless steel [35]. A multiple electrode sensor was designed using electrical resistance change as a corrosion sensing technique. This technique allows accurate, reliable measurements over a long period of time and does not require extensive electronic hardware or experimental setups associated with full-scale electrochemical corrosion measurements. When metal is oxidized and converted into oxides or hydroxides during active corrosion, the resistance across the electrode will change according to Ohm's law. The measured electrode resistance, R(Ω), can be compared to calculated resistance values (Equation 3.3) using the known material resistivity, ρ (Ωcm) compensated for temperature, and for the electrode geometry where

L(cm) is electrode length and A(cm^2) is cross section area, to yield a measurement of the effective extent of corrosion on the electrode.

$$R = \rho \frac{L}{A}, \qquad \text{Equation 3.3 [36]}$$

where R is the resistance, ρ is the material resistivity, L is the length of the electrode, and A is the cross section area.

Careful design of the electrodes was conducted to provide accurate corrosion data over a long period of time and isolate and characterize the effect of stress and sensitization. Corrosion sensor electrodes were constructed from similar stainless steel as used for canister construction. Electrodes of varying thickness were used to provide data on the extent of corrosion of the container wall, which when monitored over time can be converted to corrosion rate. Thin sensor electrodes will have a greater resistance change over short time periods and will corrode though earlier than thicker electrodes. Figure 3.13 shows a Scanning Electron Microscopy (SEM) of one corroded stainless steel electrode.

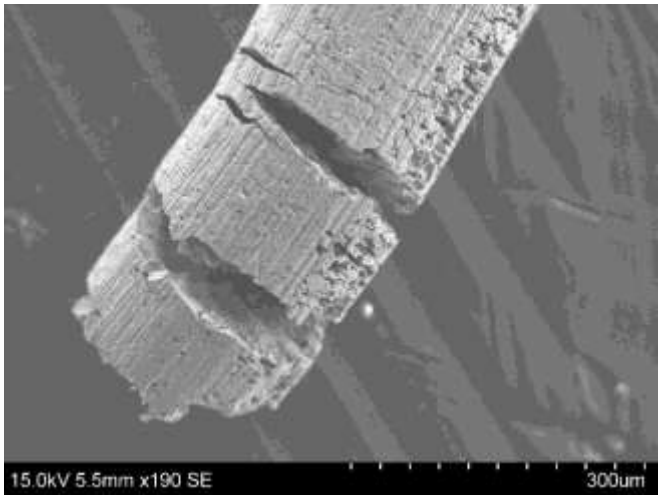

Figure 3.13. SEM Image of the Effects of Corrosion on a Stainless Steel Wire. In this image large cracks due to corrosion have reduced the cross sectional area of a stainless steel wire, decreasing the load bearing capacity and has caused the wire to break.

In Equation 3.3 the cross sectional area A is inversely proportional to the resistance of the wire. As cracks form the sections of the wire begin to lose their cross sectional area, and therefore, the resistance of the wire as a whole increases. Eventually one of the cracks will break the wire, and the circuit will be open. Mechanically, there are several methods of creating and holding the electrode samples such that they can be exposed to the environment in which they can corrode. There were three primary design revisions to these holders which we also accompanied by necessary changes in the monitoring circuit.

Corrosion Sensor Revision 1.0

The first approach for this sensor system was to create an array of sacrificial sensors tailored to account for multiple time scales and material conditions. A group of sensor electrodes were placed in parallel, with a resistor in series with each electrode. Figure 3.14 shows this configuration and the expected method of electrode failure.

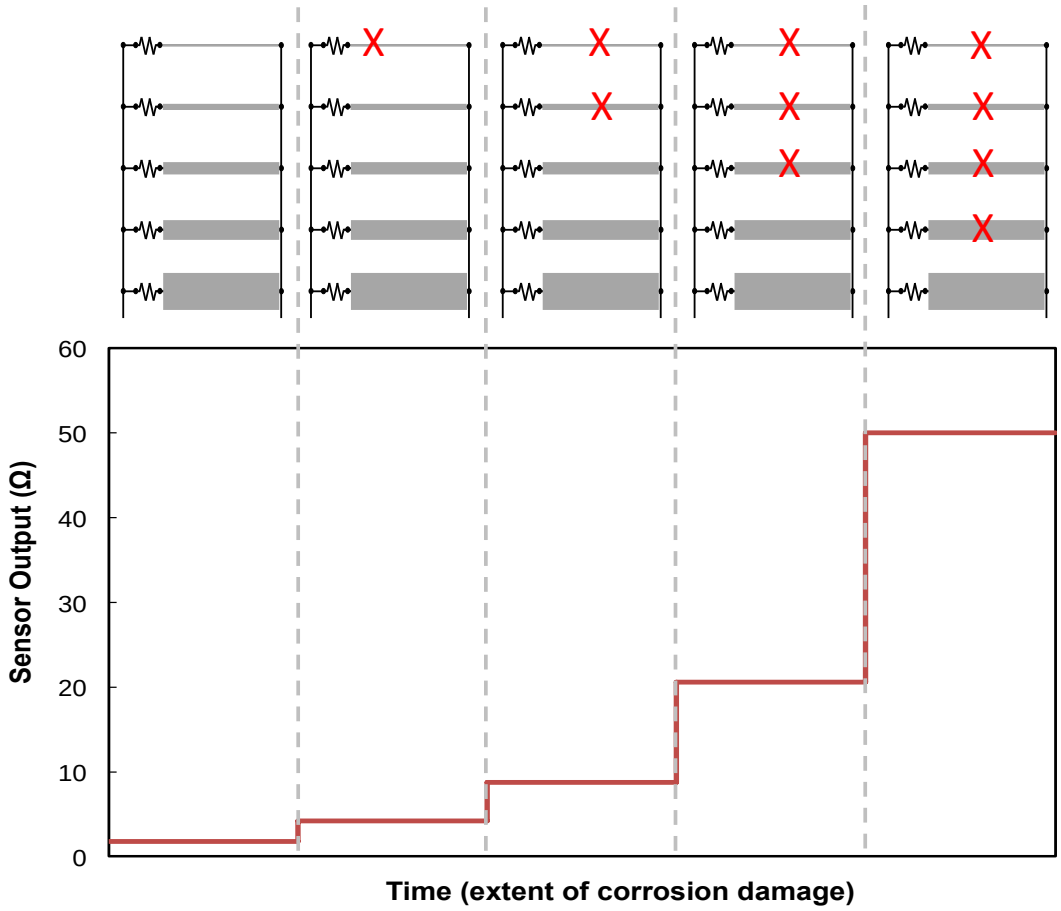

Figure 3.14. Simple Schematic diagram of V1.0 Corrosion Sensor and Example Data. The top figure shows the resistive element placed in series with each corrosion electrode of varying thickness. As each electrode corrodes and fails the total resistance of the circuit increases.

At the beginning (left most circuit) all of the electrodes are intact and the total resistance of the circuit is at its lowest. It is assumed that the thinnest electrode will break first as it's cross sectional area would leave it the most vulnerable to failure by corrosion or cracking. The second circuit shows this thinnest wire breaking and the resulting increase in resistance. This pattern is expected to continue in the third, fourth, and fifth circuits until the senor output registers an open circuit. The question then remains, what if the corrosion does not follow this pattern? The resistors are not all the same value so should this pattern not follow, then one can still determine which electrode corroded by back solving the resistive network. This form of the sensor relies on the complete loss of

the electrode cross-section and would not allow for the measurement of the slow resistive change of each electrode as it corroded. This design does, however, keep the required components to a minimum which may be beneficial in a radioactive environment and is suitable as an early warning sensor design.

Corrosion Sensor Revision 2.0

The second revision of the corrosion sensor fixed the shortcomings of the previous generation. One of the key mechanical changes was the inclusion of tension on each of the electrodes. In revision 1.0 the electrode would succumb to a crack but would then fall back together and still conduct giving a false reading. This was solved by placing springs underneath a curved "bumper" to apply tension to the electrode while it underwent testing. Figure 3.15 shows this bumper and spring setup.

Figure 3.15. Corrosion Sensor V2.0 Bumper and Clamp Design. This cross sectional view of the sensor holder shows the spring, bumper, and clamps.

The clamps on each end of the electrode are designed to pinch the sample and keep it in place while the spring maintains the tension on the sample. Should a crack of significant depth occur, the added tension will allow the sample to completely separate and no longer conduct. Two sensor electrodes can be placed on the same bumper next to each other as long as they are of the same dimensions. Figure 3.16 shows this configuration.

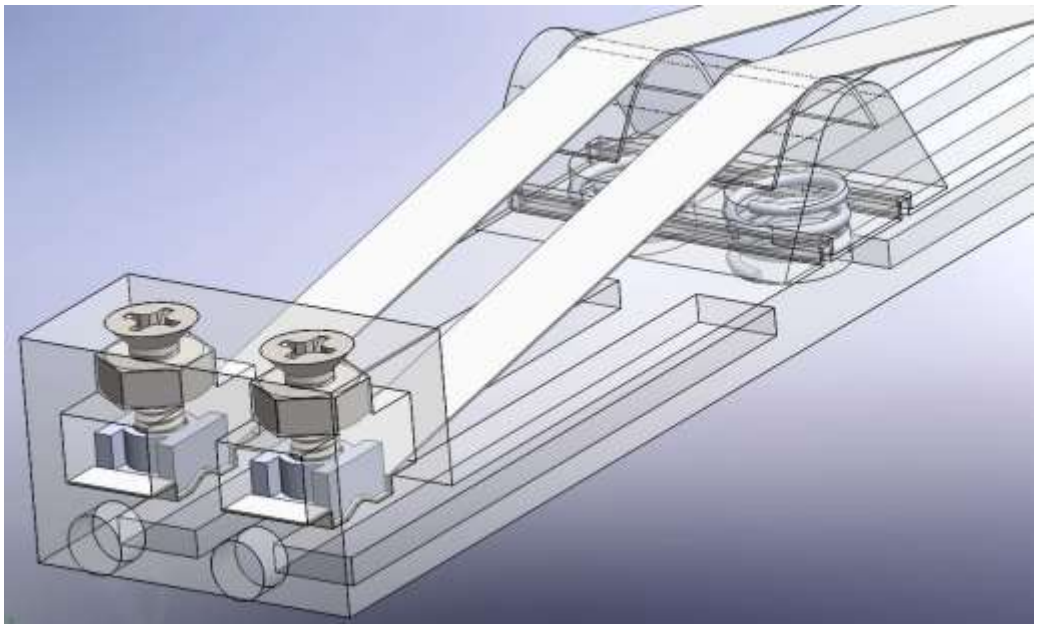

Figure 3.16. Corrosion Sensor V2.0 Dual Electrodes. This wireframe diagram shows two strip electrodes placed next to each other.

The circuitry for this version of the sensor was also upgraded to monitor each individual electrode resistance over time. The MAX9634 current sensor was used to monitor the current through each electrode with a known voltage applied. This allowed for simple and highly accurate resistance measurement to be taken, and the progress of corrosion to be monitored. The ADG706 analog multiplexor was used to manage the large number of signals. One ADG706 was connected to the load of each current sensor so only one electrode would have current flowing through it at a time. The other ADG706 was used to manage the large number of analog signals to a single ADC pin on a microcontroller with only five pins needed to control both multiplexors. Figure 3.17 shows the configuration of the current sensors and the multiplexors.

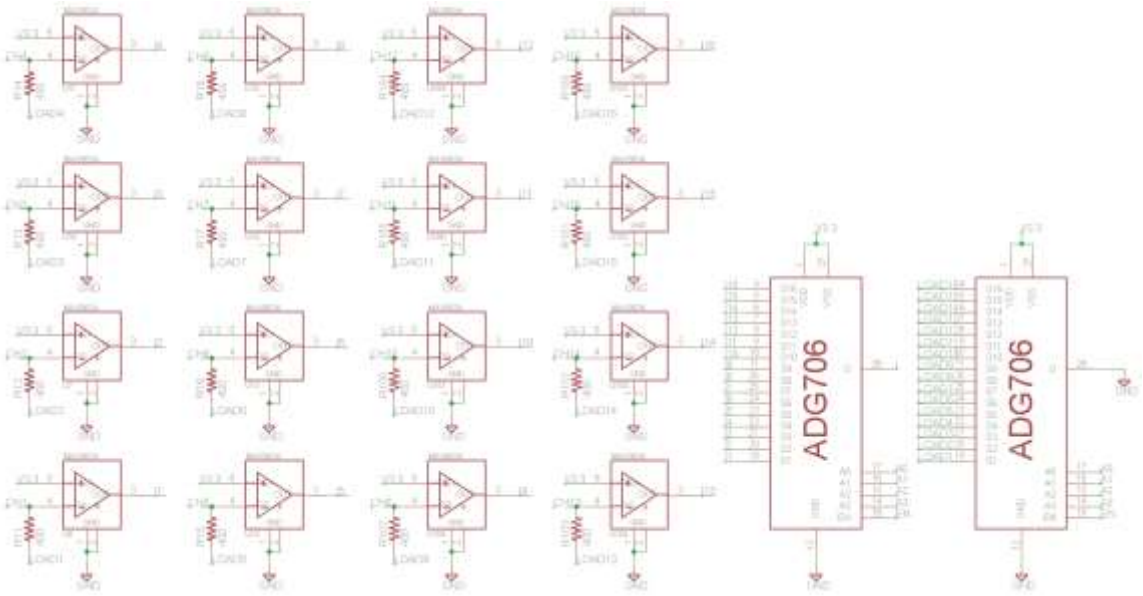

Figure 3.17. Corrosion Sensor V2.0 Current Sensors and Multiplexors. This schematic shows the 16 current sensors and the control multiplexors used to manage the large number of signals.

This entire electrode holder was created using a stereolithograph apparatus (SLA) 3D printer as it was the only feasible way to machine the specific shapes required by the design. This however led to a few problems. The first issue with this design was the tension on the samples. Thin samples or wires worked very well, but thicker strip samples caused the entire sensor to bow which proved that the tension by the springs was too high. When testing this tension, it was found that the springs would change in tension over time due to corrosion. Additional testing also showed that even though the majority of the force being applied to the sample was at the bumper, it was possible for the pressure at the clamp to cause the electrode sample to fail early. In some cases, this would leave the majority of the electrode flopping around which could easily electrically short with its neighboring sample causing a false reading.

Corrosion Sensor Revision 3.0

The last revision of the corrosion sensor improves further upon the previous generation. Figure 3.18 shows a cross section of the new sensor.

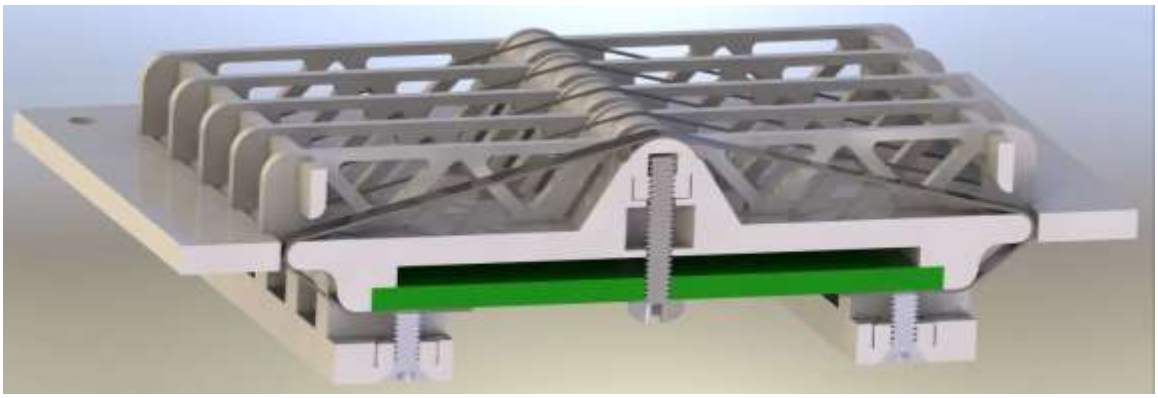

Figure 3.18. Corrosion Sensor V3.0 Cross Section Rendering. Render of the cross section of the corrosion sensor V3.0 which shows the improvements over the previous generation.

The first improvement, and most notable, is that the sensor is one piece that holds many electrodes. This process still requires the use of 3D printing, but by placing the electrodes on a compact frame and by reinforcing the structure along the direction in which the tension is occurring, all bending of the frame is eliminated. The additional reinforcement also serves a second purpose by isolating each electrode from its neighboring electrode such that when they break they do not interfere with each other. The truss formation of these reinforcements was chosen to promote airflow underneath each electrode.

The second improvement focuses around the spring and bumper. Each electrode now has its own bumper which is fitted along guide rails built into the trusses. This restricts the motion of the bumper such that the force applied to the electrode is focused at one point which drastically increases the chances of the electrode breaking at or near this point once corrosion has occurred. Additionally, the spring material has been

changed to Inconel, which is very corrosion resistant and works well in extreme heat environments. These springs have been tested before and after being subjected to an extended and aggressive HCl acid bath while being maintained a constant compressive force. Loading the electrodes onto the sensor is normally difficult to do while under tension, which is why a nut is placed into each bumper and a screw is passed from the bottom of the sensor, through the spring, and into the nut to secure it. In this manner, the electrode can be mounted, and then the screw can be removed to place it under tension.

The last improvement is the clamping mechanism. To prevent the pinching issue from the previous version, in which the electrode would become plastically deformed, all corners have been rounded out. The PCB that holds all the current sensors slides into the bottom of the corrosion sensor body and each electrode is screwed down to a pad on the PCB. If the electrode is a wire, a screw terminal can be populated onto the PCB to assist in securing it. The added gold-plated copper resistance from the pads is easily calibrated out the resistance measurement. The PCB is referred to as the corrosion sensor backbone as it helps keep the entire structure of the sensor ridged once placed into the sensor body. Figure 3.19 shows the layout of the backbone PCB.

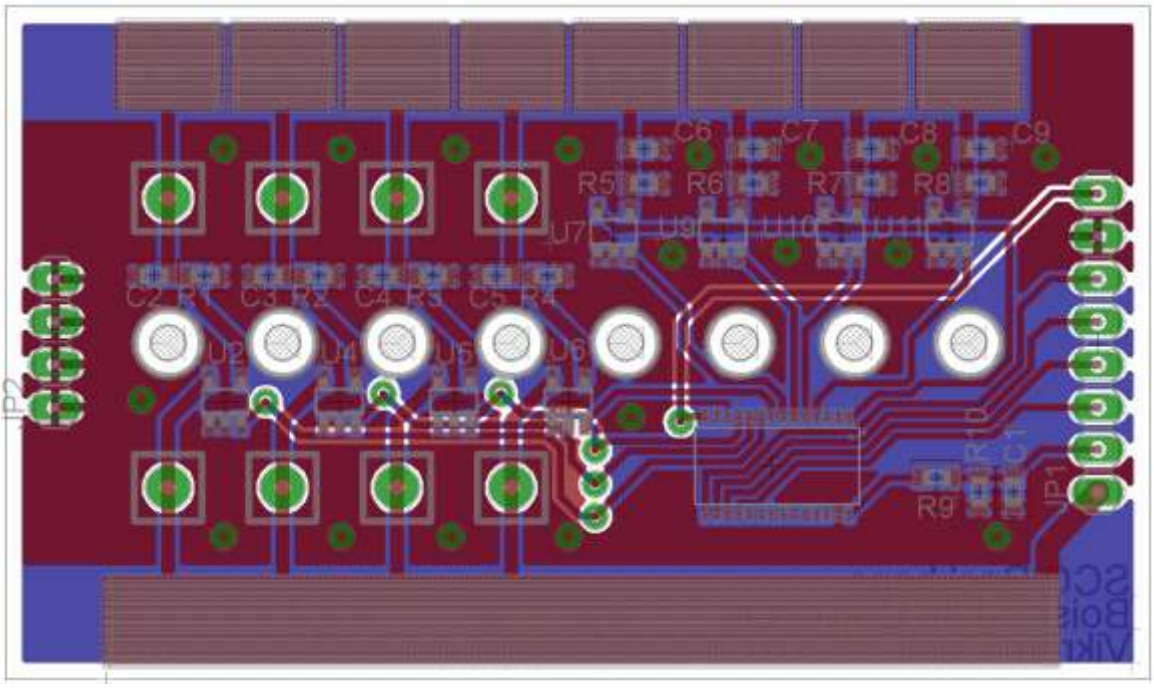

Figure 3.19. Corrosion Sensor V3.0 Backbone PCB Layout. Layout of the V3.0 corrosion sensor PCB. The layout of this board has been designed to snuggly fit into the body of the corrosion sensor.

The Backbone PCB circuitry was redesigned from the previous version with modularity in mind. Different corrosion sensor element geometries require different current sensor gains. For instance, a thick element would have more current flowing through it and, therefore, less resistance. This would cause the amount of voltage drop on the element to be small and, therefore, require a larger gain to read properly. The opposite would be true of a thinner sensor element. The MAX9634 current sensing IC comes in four fixed gains which can be selected and populated on the Backbone PCB based on the resistance of the corrosion sensor element. This configuration also reduces the number of multiplexors required and the number of control signals required to read each channel which also increases the speed at which each channel can be sampled.

CHAPTER FOUR: SENSOR NODES

The majority of the sensor electronics result in an output that is measured by converting an analog voltage into a digital one. In order to do that an IC with an ADC is required. Once these values are read, they need to be processed and transmitted to some form of storage. In the process of creating all of the sensor boards which collect all of the environmental data, motherboards which process and store the data were also created. Once these pieces were finalized, they required enclosures and mounting methods to make them field deployable. The following sections will cover the iterative design process that was followed to complete three standalone sensor node designs and the feedback that was received from the NRC that fueled each stage of the design.

Motherboard V1.0: Atmegaton

The first motherboard was designed using previously researched and tested hardware that was much more powerful than what was required for this project. The idea was to create something with enough capacity that the sensor system would never want for more power or processing speed. A key concept was to make the motherboard modular, so it could take on other daughter boards and attempt to expose almost all unused IO pins to these boards. In short, this motherboard was to be akin to many available development boards focusing on sensor design.

This motherboard was called the Atmegaton due to its use of the Atmega AT32UC3A2 32-bit processor. The LPQF144 package in which this processor came gave

it an abundant amount of IO to control a variety of devices. Figure 4.1 shows the layout and populated versions of the board.

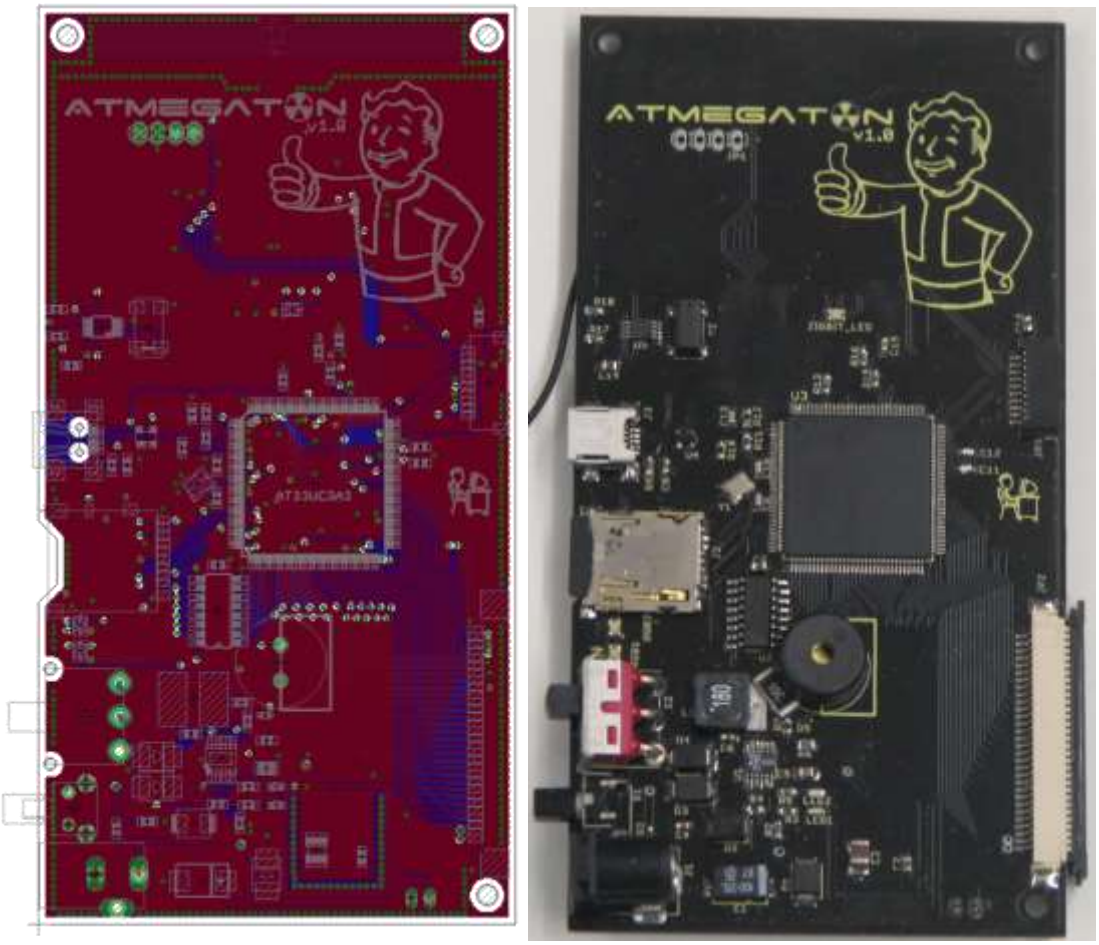

Figure 4.1. Motherboard V1.0 Atmegaton Layout and Populated. The layout (left) and populated (right) of the Atmegaton motherboard.

The key driving force for this design was the uncertainty of the final form factor and sensor set. It was unclear at the beginning of this project how the sensor system would be powered and at what voltage. It was also unclear as to what sensors would be used and what their support needs would be. This motherboard in essence became a development board where all the sensors could be prototyped.

To meet the needs of any future development or field deployment, several key design features were selected. A wide DC input range of 12V to 40V was selected, which would allow the sensor system to run off a large number of wall adapters or even off of vehicles. All power entering the system is filtered for extraneous noise and protected using a resettable fuse (PPTC). A battery backup system was also implemented to both charge and use 7.4V lithium polymer batteries in the case of power failure. Switching time from wall power to battery power was measured to be less than one micro second. The voltage taken from any of these sources was stepped down to 3.3V using a high wattage linear regulator. The final design also moved nearly every unused processor IO pin out to two 30 pin flat flex cable (FFC) headers to be used as daughter board connectors. This allowed external sensors to be attached to report back data which could then be stored on a SD card, sent out via USB, wirelessly transmitted via a ZIGBEE radio, or any combination of the three.

The ZIGBEE option is of particular interest to this application as it would take advantage of the close proximity of storage containers. ZIGBEE is a personal area network protocol that implements mesh networking, which would allow sensor modules to communicate directly with each other as well as relay data from module to module and eventually to a central data repository. This type of non-hierarchical networking would allow for a very flexible and redundant wireless network and also reduce the amount of power needed to send data.

Boise State Barnacle V1

The first daughter board developed for the Atmegaton Motherboard was an I2C to Ethernet (RJ-45) converter, which was designed to multiplex several I2C devices. The

primary goal was to place a sensor on every Ethernet port which would allow a variety of different devices to be placed on each port. In this fashion a humidity and atmospheric temperature sensor was developed as well as a thermocouple based temperature sensor. These devices could be plugged into any Ethernet port and be recognized via their unique I2C hardware address. Once this had been proven as a viable means of sensor development, the first full sensor system was designed. This sensor board consisted of twelve thermocouple reading circuits, a humidity sensor, a time of wetness sensor, an atmospheric corrosion sensor, a Geiger counter, five corrosion sensors (revision 1.0), and an internal temperature sensor. Figure 4.2 shows this board.

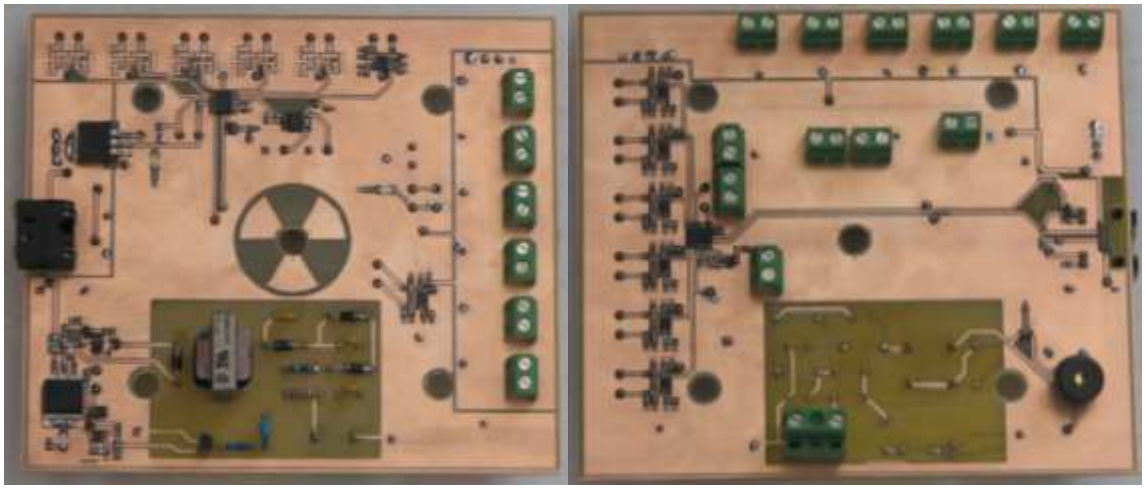

Figure 4.2. Boise State Barnacle V1 Populated. The top (left) and bottom (right) of the Boise State Barnacle sensor board. The board measures 13.8 cm X 12.1 cm.

This sensor board interfaced via an Ethernet port, and all sensors could be polled and recorded once a second. The enclosure for this board was designed to fit on top of the stainless steel canister and hang from the lid in a manner very similar to a barnacle on a ship's hull, so it was named the Boise State Barnacle. Figure 4.3 shows the assembled enclosure.

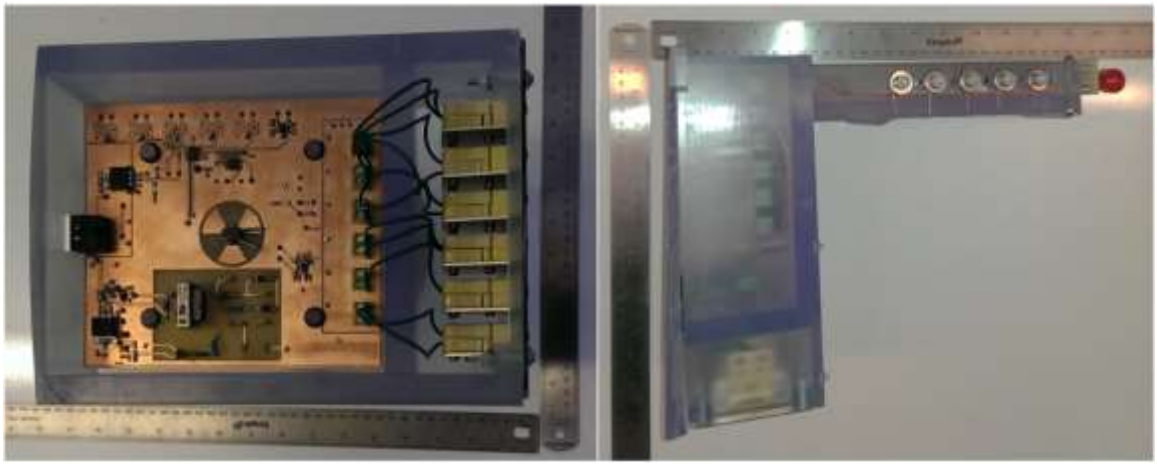

Figure 4.3. Boise State Barnacle V1 Enclosure. Top view of the enclosure showing the circuit board and thermocouple connectors (left) and view of the side of the sensor node showing the senor boom (right).

The enclosure was designed to protect all the circuitry from the elements and the radiation. The walls around the electronics were designed in order to withstand the expected radiation should the sensor node be place on top of the canister and the casing material be made out of titanium. A thermocouple mounting plate was installed in a separate compartment to provide additional shielding from the elements, and all additional external sensors were placed in a sensor boom attached to the bottom of the node. The atmospheric sensors, such as the humidity, time of wetness, and corrosion sensors faced outwards as shown in Figure 4.4.

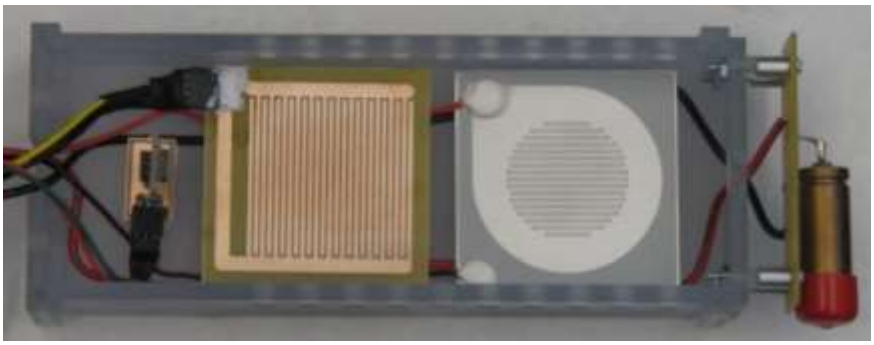

Figure 4.4. Boise State Barnacle V1 Sensor Boom. View of the sensor boom without the protective cover. Picture shows from left to right the humidity, time of wetness, corrosion, and radiation sensors.

The Geiger tube was placed at the bottom of the boom, but never weatherproofed for this version of the enclosure. All signals were routed from the top of the boom to the bottom of the enclosure cavity to protect against water. When attached to the canister, the sensors would be covered with a protective mesh covering that would allow air to flow through but keep all other large debris out.

When this project began, the grant proposal did not provide very many details or specifications on the corrosion sensor besides the ability to detect corrosion and the contributing factors of corrosion. Hence, the first sensor node design was developed with great uncertainty. The initial feedback from the NRC had many positive points. The number and type of sensors was appropriate as were the wireless capabilities, however the form factor needed work. This design was far too big and was limited to being hung from the canister lid. It is possible for the canisters to be stored horizontally which would make attaching this sensor node much more difficult. The spacing between the stainless steel canister lid and the concrete overpack also varies from each storage container model which would mean that a custom enclosure would need to be made for each model. The final verdict was to reduce the number of sensors and make it smaller and allow the sensor node to be placed in more locations around the canister.

Boise State Barnacle V2

The second standalone sensor node design would have to be smaller and flatter to fit inside more locations around the canister, so many of the sensors modules needed to be redesigned. At this point the revision 2.0 corrosion sensors were designed to accommodate the reduced space and to provide more detailed information on the rate of corrosion. The sensor motherboard was also redesigned on a six layer board which allowed for the

electronics to be compressed into a very tight space. Figure 4.5 shows the Micro Megaton motherboard.

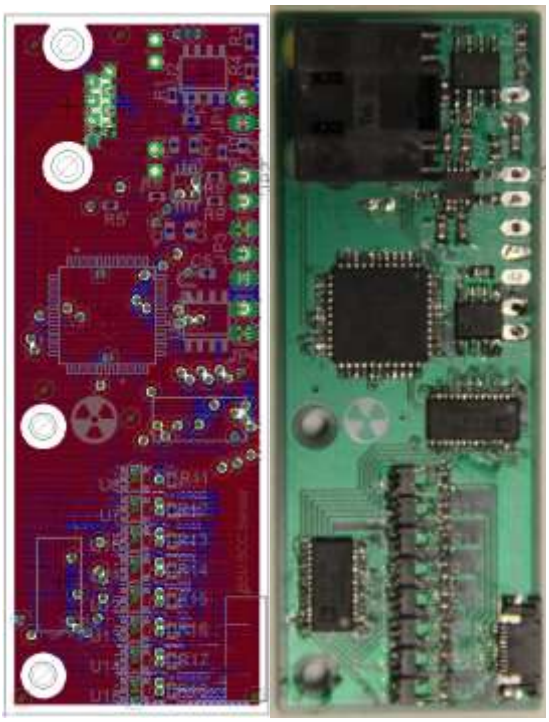

Figure 4.5. Motherboard V2.0 Micro Megaton Layout and Populated. The layout (left) and populated (right) of the Micro Megaton motherboard. The board measures 2.7 cm X 7.3 cm.

The revision 2.0 corrosion sensors can support different electrode geometries, and in order to test these different geometries more corrosion sensor channels were required on this motherboard. The final sensor support count came to one thermocouple reading circuit, a humidity sensor, a time of wetness sensor (custom dimensions), an atmospheric corrosion sensor, a Geiger counter, sixteen corrosion sensors (revision 2.0), and an internal temperature sensor. By reducing the number of thermocouples and improving the mechanical design of the corrosion sensors, a smaller sensor package was designed as shown in Figure 4.6.

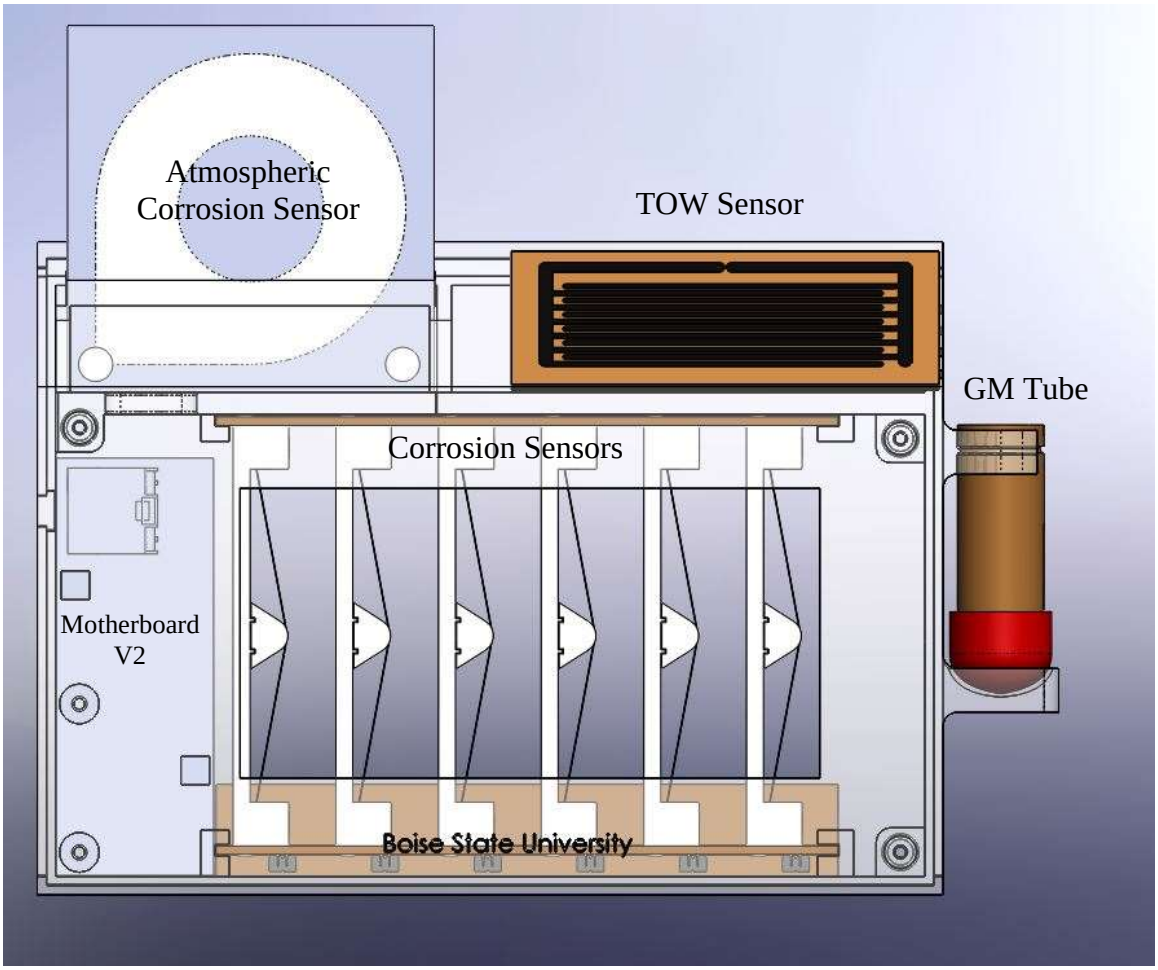

Figure 4.6. Boise State Barnacle V2 SolidWorks Design. This image shows the internal component layout for the Boise State Barnacle V2 sensor node.

The hollow section in the middle of the node allows air to freely pass through the center, which reduces the impact of the node's presence on the canister. For this design however, only twelve of the sixteen corrosion sensor channels were filled to reduce the size of the node. Since the time of wetness sensor could be designed to fit any shape, it was remade to fit on the top of the node at a 45° angle which was found to be an optimal orientation. Miniaturizing the corrosion sensor, however, was still a problem since at this point only the large version was available. The best solution was to recess it partially into the node until it to could be redesigned to be smaller. This version of the enclosure

needed to be weatherproofed, so it was made to be compartmentalized and potted with an epoxy resin. Figure 4.7 shows a rendering of the node from behind.

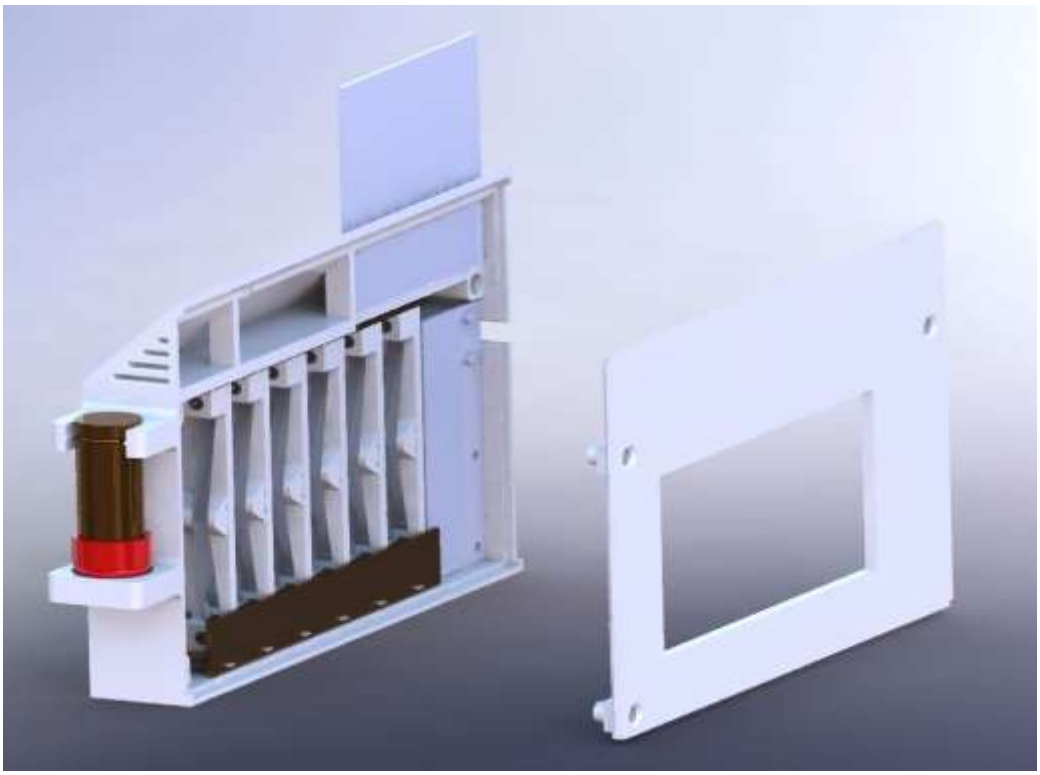

Figure 4.7. Boise State Barnacle V2 SolidWorks Design Rear View. This image shows the rear of the sensor node with the back plate removed. The various compartments can be seen.

The epoxy resin can be poured from the back to fill each compartment and seal it from moisture and corrosive elements while providing thermal insulation and increasing vibration resistance. The back plate in this design was not created with its intended thickness for shielding purposes in order to save prototyping costs, but when deployed would be the appropriate thickness/material depending on expected radiation levels.

In order to build the sensor node a SLA 3D printer was again used to construct the enclosure. Instead of running wires from the corrosion sensors to the motherboard, three PCB boards were used to internally mount the sensors and route the signals. The final

connection between these PCBs and the motherboard was a centimeter long FFC cable. By routing the signals in this manner, the overall structure of the package was improved, and the signal to noise ratio from the sensors was increased. Finally, venting holes were placed in one of the sections to allow atmospheric sensors (humidity and temperature) access to the air, and in the end these sensors were given an unpotted compartment to reside in. Figure 4.8 shows the final assembled sensor node.

Figure 4.8. Boise State Barnacle V2 Assembled. This image shows the assembled Boise State Barnacle V2 sensor node.

When compared to the size of the canister, this sensor unit very small. Figure 4.9 shows a CAD design of a HSM-H Nuhoms Horizontal Storage Module provided by the NRC and the sensor node placed within it.

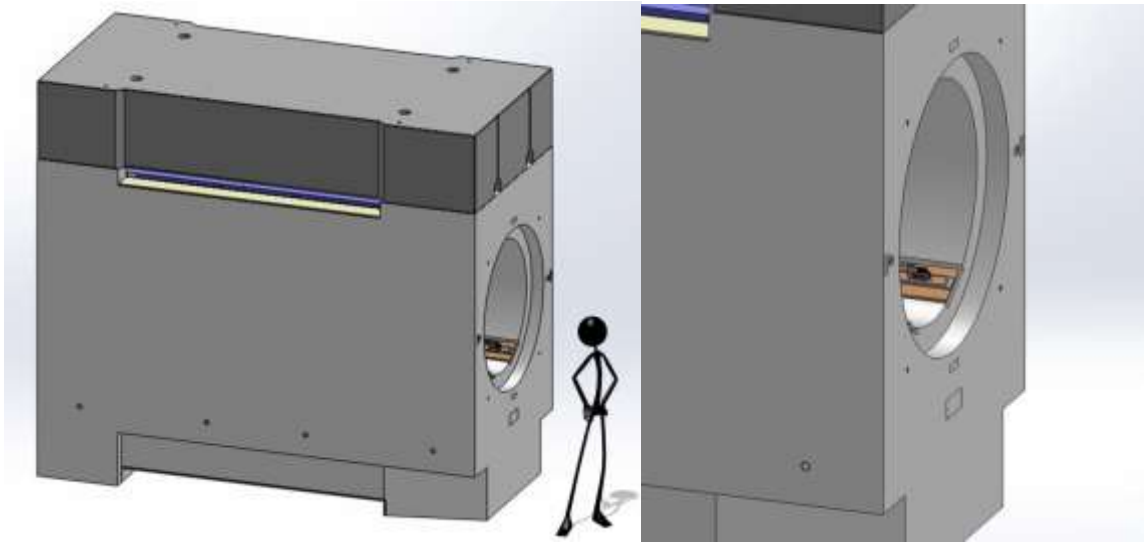

(a) (b)

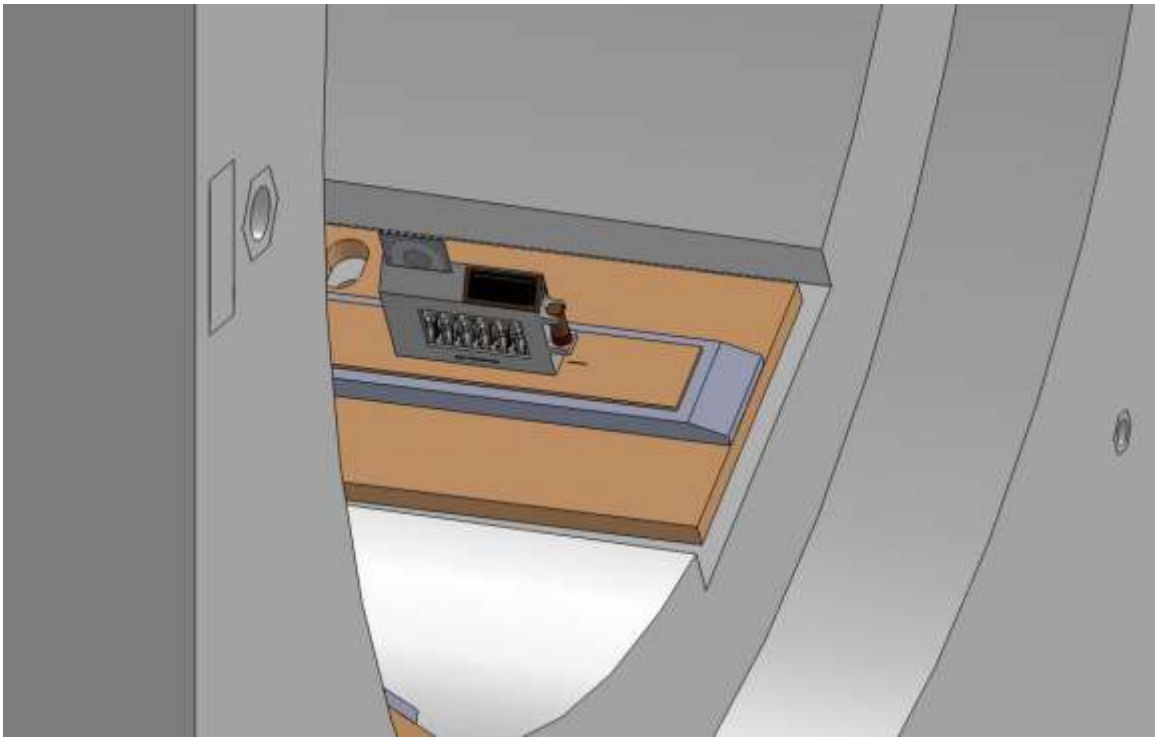

(c)

Figure 4.9. Boise State Barnacle V2 Depicted on a HSM-H Nuhoms Horizontal Storage Module CAD Model. (a) shows the storage module next to a 6 foot tall human to show the scale of the design. (b) shows a zoom in of the mouth of the container where the Barnacle V2 is placed. (c) shows a complete zoom in of the Barnacle sitting on one of the canister rails.

This shows that there are many locations where multiple sensor nodes could be placed to monitor the canister once it is placed inside the storage module.

The unit was turned on and a live demo was shown of the unit reporting data wirelessly. The feedback received was to decrease in size of the unit as well as the shape and sensor layout. A common theme that was discussed during the presentation was to make it “cell phone sized.” This would mean decreasing the size of the sensor node considerably more, but also redesigning the corrosion sensor modules to be even smaller.

Boise State Barnacle V3

As described in the previous section, the Boise State Barnacle V2 had some shortcomings when it came to its size. The V3 design would target the enclosure to be the size of a cell phone rather than that of a tablet. This requirement was the driving force behind revision 3.0 of the corrosion sensor module. Since the corrosion sensors are physically the biggest part of the system, it was surmised that all electronics should be built into it or at least made to be as compact as possible. This was accomplished by mounting a new motherboard design directly onto the back of the corrosion sensor board. Figure 4.10 shows this setup in an exploded view diagram.

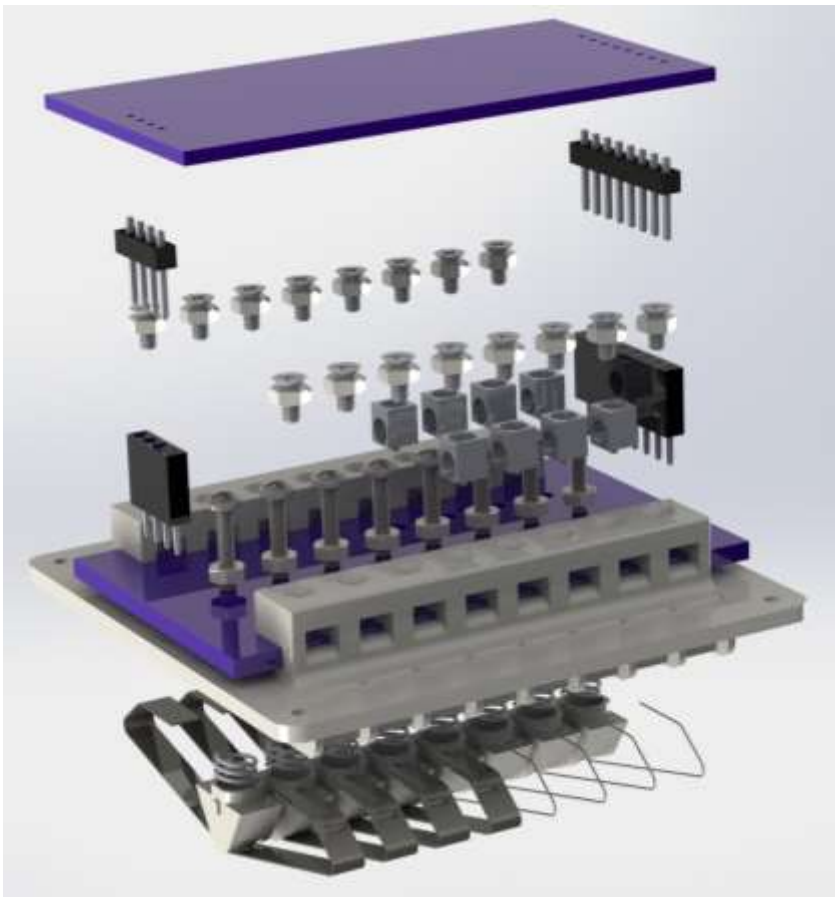

Figure 4.10. Exploded view of the Revision 3.0 Corrosion Sensor Attached to a Motherboard. Instead of using wires to connect this corrosion board to the motherboard, the motherboard has been designed to mount directly onto the back of the corrosion sensor board.

The new motherboard has been programmed and tested to perform as a standalone system or to work in a sensor network. An added benefit to this redesign is that the microcontroller has the ability to be programed remotely over the Ethernet cable. This capability will allow firmware updates to be applied in the field. When working in a radioactive environment, there is always the chance of beta and gamma particles "flipping" bits within the program memory of the main microcontroller which could effectively cripple or destroy the sensor system [37]. Being able to program the microcontroller also means that the entire memory from the microcontroller can be downloaded and compared to what was uploaded. This will allow testing of radiation

shielding to ensure that no bit flipping will occur in the field. Figure 4.11 shows this new motherboard.

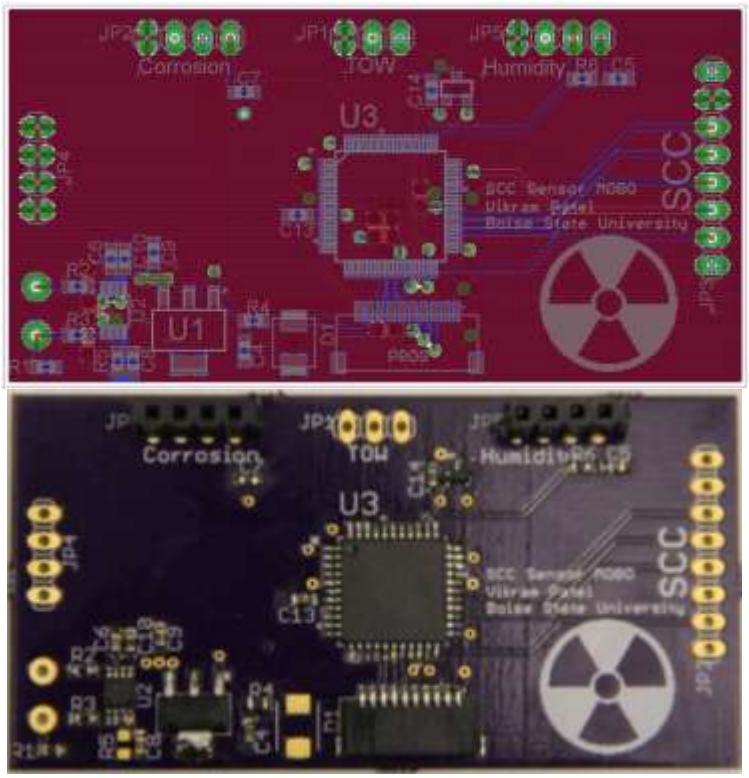

Figure 4.11. Boise State Barnacle V3 Motherboard. The top image shows the layout of the board and the bottom image shows the populated version. This board measures 6.8 cm X 3.5 cm.

The FFC connector passes all the signals from the Ethernet cable to the rest of the system. This includes the power, programming, and communication signals. The main power is passed through a transient voltage suppressing diode and a ferrite chip before it reaches the main regulator which provides a clean 3.3V to the remainder of the circuit. Multiple decoupling caps have been placed near all the sensor IC to aid in keeping all analog signals clean.

Rather than keeping all of the senor ICs on the motherboard, the corrosion and TOW sensors have been moved to their own daughter board. These sensors produce a

millivolt range signal which is susceptible to external noise. In order keep the signal to noise ratio high, the sensing ICs have been moved to be as physically close to the sensor as possible, and the resulting amplified signal is sent to the motherboard ADCs for reading. Figure 4.12 shows images of the populated daughter boards.

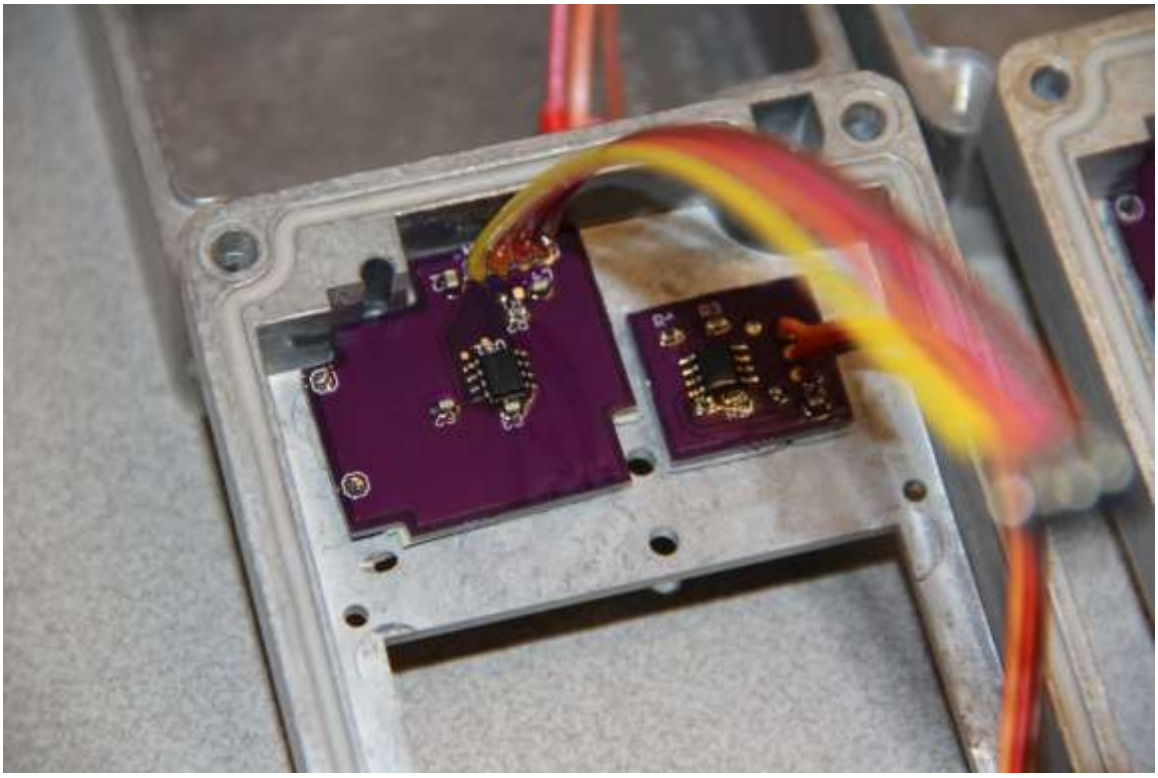

Figure 4.12. Boise State Barnacle V3 Daughter Boards Mounted. The board on the left is the corrosion sensor board and the board on the right is the TOW sensor board.

The analog signals recorded are not fast changing, therefore simple digital low pass filtering is used to average the results. Each analog sensor is read at a rate of 2 kHz and then averaged per sensor report. This is particularly useful for reading temperature signals as a digital low pass filter can be used to remove noise. Implementing this scheme vastly reduces the amount of sensor noise recorded. The remaining digital atmospheric humidity and temperature sensor is limited to reading at 0.5 Hz due to its serial

communication protocol, but it has built in filtering and can be read without the use of averaging.

A 3D printed SLA case is not robust enough to be field tested and would most likely fail mechanically before the completion of the test. However, machining a new case out of any other material would be costly and impractical for an early stage design. Thus, a premade weather proof (NEMA 4) aluminum enclosure was selected that was the appropriate size and shape for the sensor system. This case was also selected because the machining of aluminum is simple compared to other weather proof materials. Figure 4.13 shows a cad drawing of the case with sensors (except for the thermocouple lead).

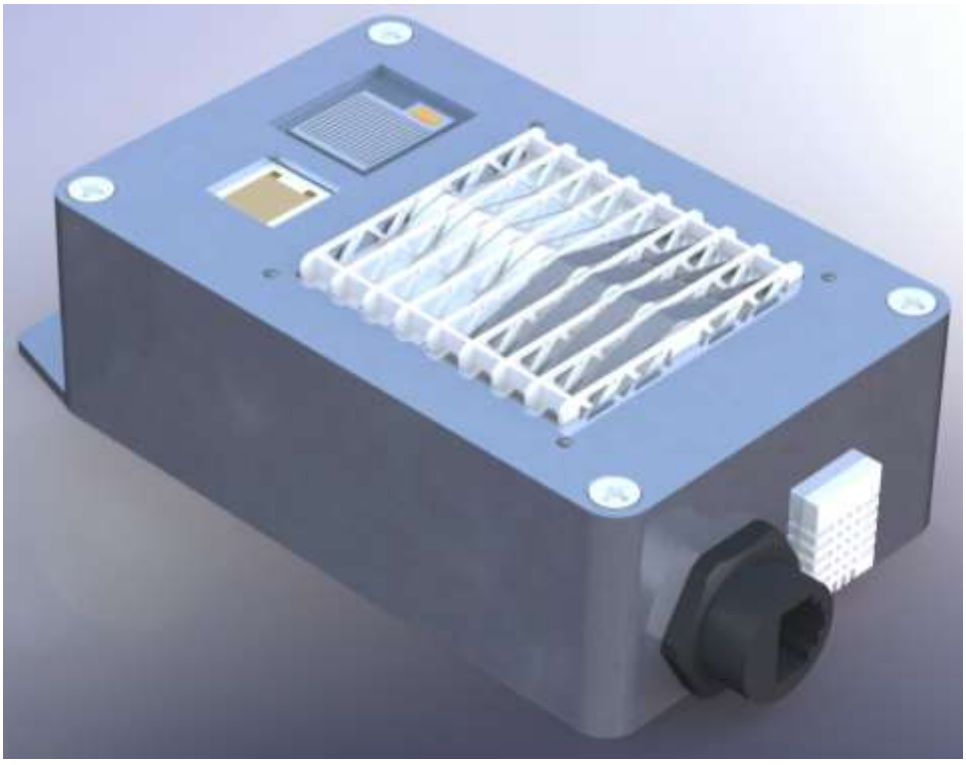

Figure 4.13. Boise State Barnacle V3 Case CAD Image. This image shows the preliminary design for the Boise State Barnacle case with sensor placement.

The miniature time of wetness sensor and corrosion sensor have been implemented on this design, and the Ethernet jack has been replaced with a weather proof version. Figure 4.14 shows a picture of the case with all the sensors present.

Figure 4.14. Boise State Barnacle V3 Case. This image shows the current state of construction for the Boise State Barnacle V3.

The case itself contains a rubber gasket fitted between the two mating halves of the lid and the base which when compressed by the pressure of the lid screws creates an IP66 rated seal. This is acceptable for the application of outdoor monitoring as full immersion in liquid is considered unlikely. Figure 4.15 shows this seal as well as the machined cutouts in the lid.

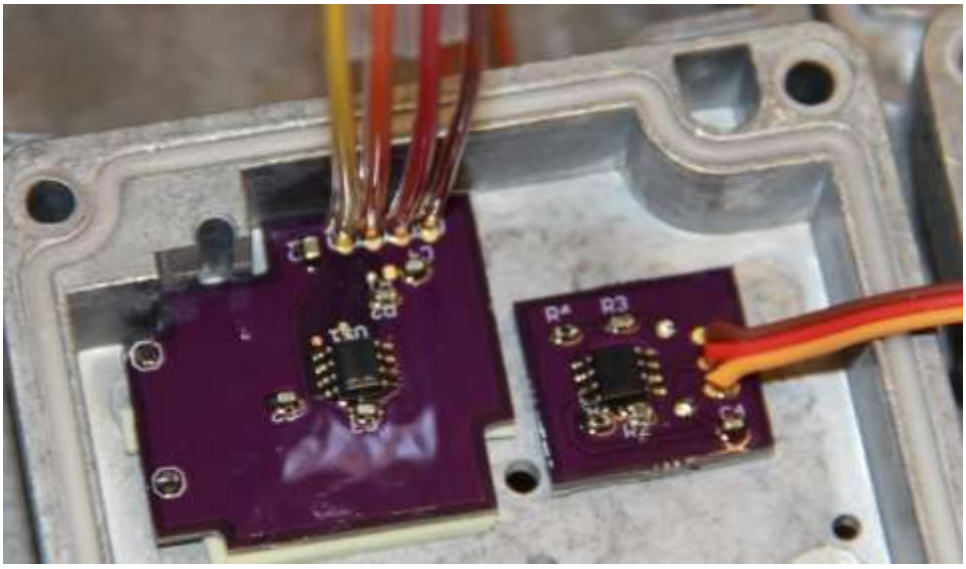

Figure 4.15. Boise State Barnacle V3 Seal and Lid Cutouts. This image shows the rubber gasket seal that surrounds the entire lid as well as the machined cutouts for the sensors.

The weather proof Ethernet jack has standard punch down pin connectors which are wired to a mating FFC converter PCB. The FFC bridges this PCB and the motherboard providing it with power and communication. This method of connection was chosen over directly wiring the Ethernet jack into the motherboard for assembly reasons. By using a FFC, the lid and the base can be quickly separated and connected and very little stress is applied to the connectors and the PCB by the cable. Figure 4.16 shows the Ethernet jack along with the FFC converter PCB.

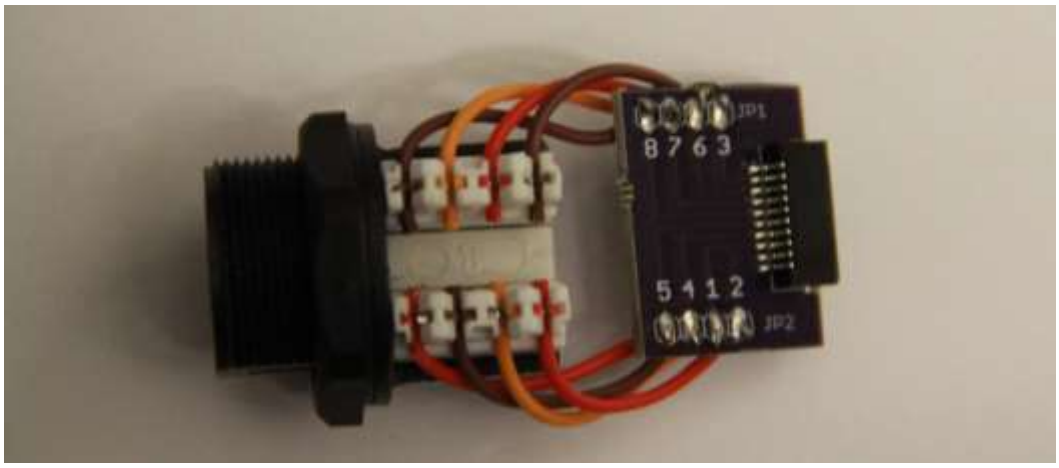

Figure 4.16. Boise State Barnacle V3 Ethernet Jack and PCB. This image shows the weather proof Ethernet Jack and FFC converter PCB.

The atmospheric humidity and temperature sensor is designed such that liquid moisture will not condense upon it within normal operating conditions, but this will not prevent condensed liquids from flowing onto the sensing elements. The optimal position for the sensor when deployed was, therefore, found to be downward facing such that liquids would have to flow upwards in order to saturate the sensor. The mounting hole for this sensor was cut next to the Ethernet jack cutout which is also downwards facing. Figure 4.17 shows this cutout with the atmospheric humidity and temperature sensor mounted.

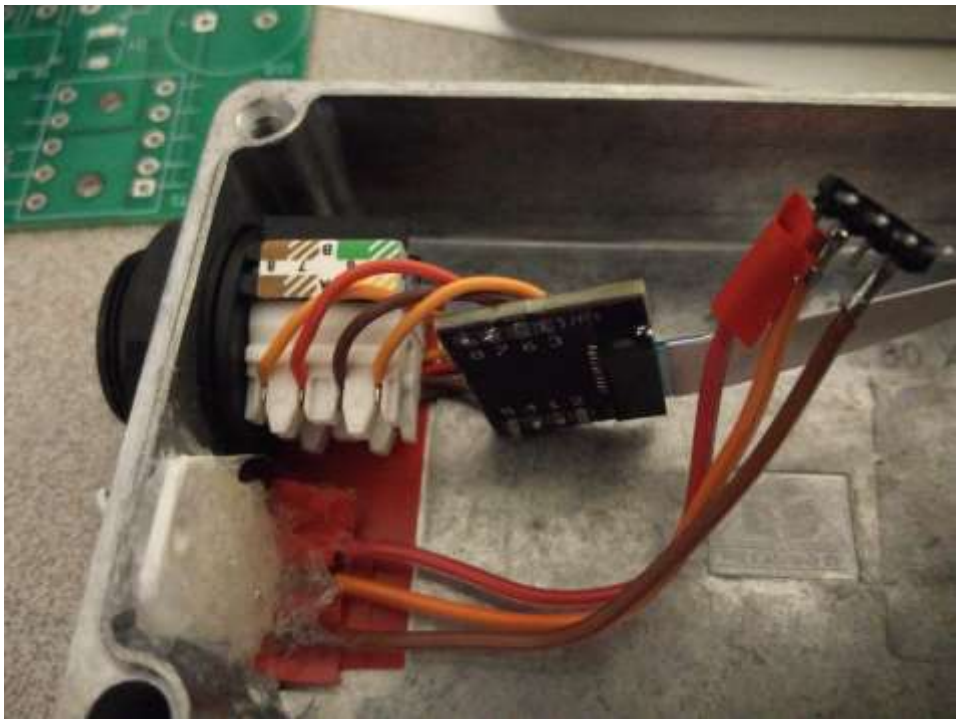

Figure 4.17. Boise State Barnacle V3 Atmospheric Humidity and Temperature Sensor Mounting. This image shows the atmospheric humidity and temperature encapsulated in silicone and mounted into the cutout.

The remaining electronics, which includes the motherboard, corrosion sensors, corrosion sensor, TOW sensor, and thermocouple are attached to the lid. The only electrical connection between the base electronics and the lid electronics is the FFC and the atmospheric humidity and temperature sensor cable. The corrosion sensor has four mounting points that attach it to the lid via screws and fasteners. The motherboard is attached to the corrosion sensor by friction lock headers, and all other sensor cables are directly attached to the motherboard. This allows the lid to be attached or detached from the base quickly and easily during assembly.

The Boise State Barnacle V3 differs from its predecessors in that all of the electrical components have been selected to operate at high temperatures. The previous generations had a maximum operating temperature of 85°C, while the lowest maximum operating temperature of any single component on the V3 is 125°C. This will allow the

electronics to function within an environmental chamber over a larger temperature range and increase the lifetime of each sensor node.

Communication distance has also been improved by taking advantage of the twisted pair lines within the Ethernet connector. By coupling DC voltages with the UART communication lines and limiting the BAUD rate to 9600 bps, successful and continuous communication was achieved through a 1000 foot roll of Ethernet cable. This cross talk reduction even allows each sensor node to be programed over these long distances. The distance between a sensor node and the nearest coordinator is undefined and would be dependent on the deployment pattern of the sensor network. Maximizing the communication distance should allow for more versatile network topographies to be implemented.

CHAPTER FIVE: CORROSION FORECASTING

Corrosion sensors inform the system of the current corrosion levels for each of the electrode geometries; however, it is more beneficial for the system to estimate the point at which each of the electrodes will fail. Prognostic evaluation of a canister's health would allow for need based preventative maintenance rather than scheduled maintenance. In order to accomplish this, all past and present sensor readings must be taken into account and then applied to an expected corrosion curve model. In order to create such a model, the mechanics behind corrosion must be understood and data must be collected.

Causes of Corrosion in Stainless Steel

Corrosion is of particular interest in coastal regions due to the presence of chloride ions. Chlorides in the form of atmospheric salts can deposit on the canister and become the sites of pitting initiation. A multitude of parameters such as temperature, humidity, salt composition, and material properties dictate the initiation and growth of corrosion. ISFSI sites located near coastal regions have been carefully studied to determine the amount of salt deposited on a daily basis. An EPRI report [6] of 13 ISFSI sites and one corrosion test site in Kure Beach, NC showed that deposition rates were as high as 0.855 g/m^2 within a single day. The humidity in these locations was also found to be 75% RH (relative humidity) on a regular basis [6]. These parameters have been shown within the needed initiation parameters for corrosion of stainless steels though various studies. Chloride concentration as low as 0.8 g/m^2 has been shown to cause corrosion in austenitic steels [38]. RH values between 25% and 75% have been shown to cause

sodium chloride to deliquesce on a surface leading to an increased probability of corrosion. Deliquescence is particularly hazardous because a dissolved salt deposit will create a ready transport medium for dissociated ions, driving the dissolution of metal at the metal-solution interface [39].

The microstructural features of welded stainless steel are roughly divided into three distinct zones, weld metal (WM), heat-affected zone (HAZ), and base metal (BM). The cycle of heating and cooling that occurs during the welding process affects the microstructure and surface composition of welds. This produces a significant residual stress field in the weldment which contributes to pitting susceptibility. The HAZ is especially susceptible due to the weld thermal cycling, mixed alloy compositions, and varying grain sizes. Figure 5.1 [40] shows the varying microstructural features caused by the welding process.

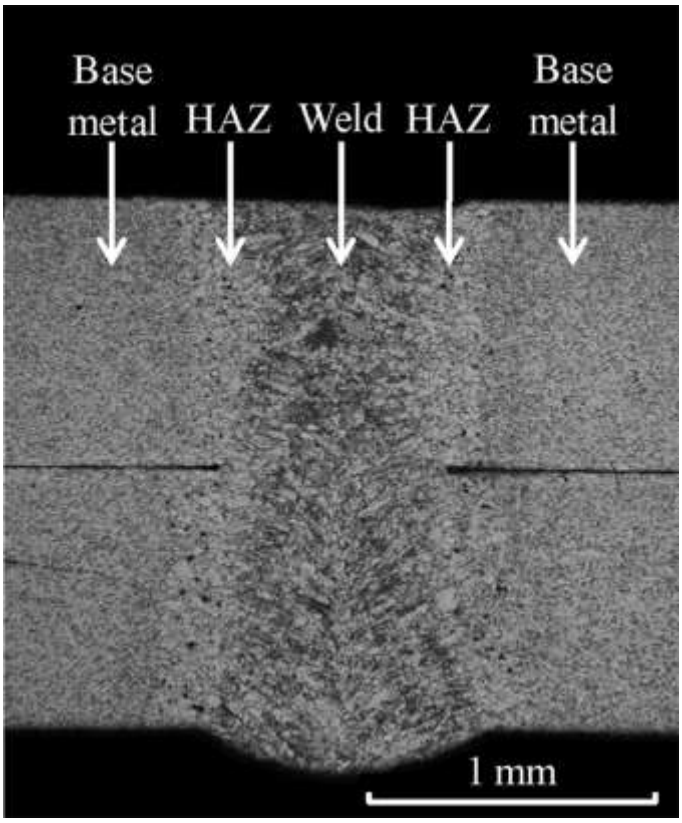

Figure 5.1. Weld Microstructures. This image shows a single weld and the three distinct zones of microstructural features. [40]

In order to replicate these conditions, the corrosion sensor elements can be welded and plastically deformed at their midpoint. This would place the bumper of the corrosion sensor element holder directly below the weld and increase the chances of corrosion occurring.

Corrosion Mechanics

The mechanism of corrosion is a widely debated topic, and several volumes have been written on the subject. It is agreed that the plastic deformation of a metal provides an increased number of active sites on which pitting corrosion can initiate. Static tensile stress, much below the yield stress, is needed to form pits. This stress may be directly applied or residual in nature, but would not develop pits without the addition of a corrosive environment. The source of these stresses can come from external forces such

as centrifugal forces or temperature variation while residual stress come from forming, heat treatment, welding, machining, and/or grinding [41].

Corrosion is initiated by stress concentrations at defects on the material surface. Stainless steel forms an ultra thin passive film (oxide film) over its surface when exposed to oxygen in the atmosphere. This film can be chemically corroded via chlorides deposited on the surface. In marine atmospheric environments, the moisture present in the atmosphere may condense and form droplets and/or thin electrolyte layers containing chloride ions when the temperature drops and relative humidity rises. In contrast, an increase in the temperature and/or fall in the relative humidity leads to evaporation and an increase in the chloride concentration. Should the attacked area received enough aeration, the steel can repassivate or heal the damaged passive film. If not healed and a critical chloride concentration is reached, the exposed steel becomes anodic and the surrounding area of steel is cathodic which results in galvanic corrosion. The electrolyte provides a means for ion migration, whereby metallic ions move from the anode to the cathode. This leads the metal at the anode to corrode and form a pit. Figure 5.2 shows the evolution of a pit.

A

B

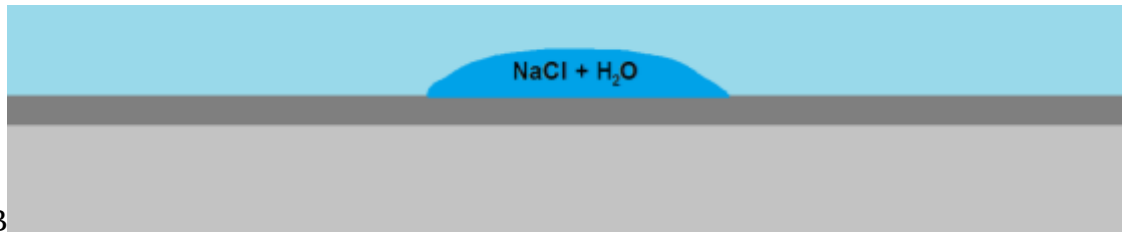

C

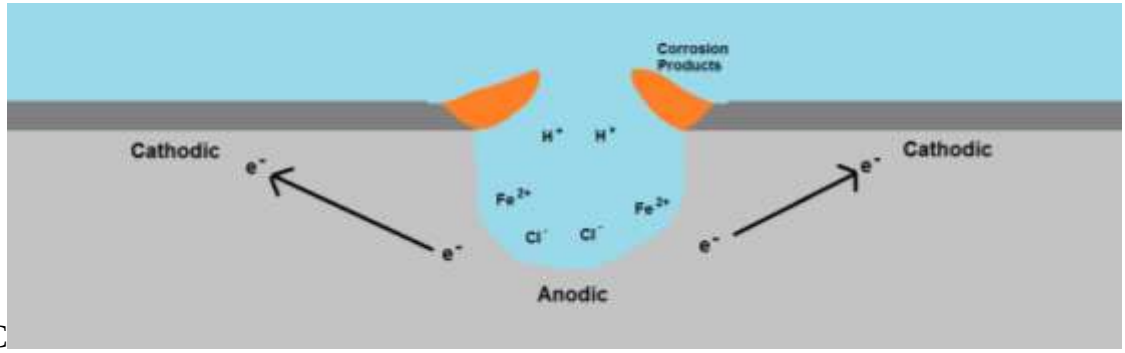

Figure 5.2. Galvanic Pitt Evolution. Image A shows the passive film formed on the stainless steel when exposed to oxygen. Image B shows a drop of salt water on the passive layer. Image C shows the formation of a pit via galvanic corrosion and the formation of the anode.

Using a focused ion beam (FIB) to mill small sections of a pit in order to show its cross section reveals much about the method in which the metal it attacked. Pits can take a variety of shapes and sizes which are normally a function of chloride concentrations and intergranular size and spacing. Figure 5.3 shows a pit that has been milled to show its tear drop shaped topography.

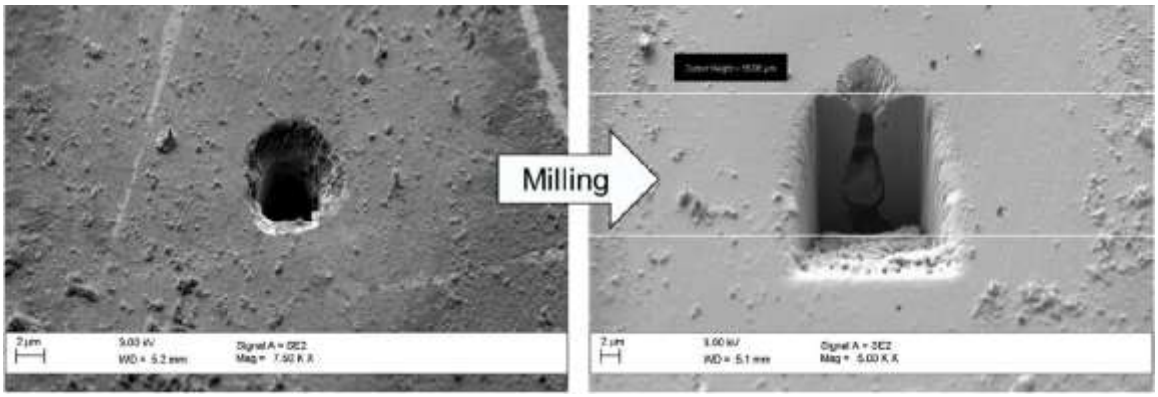

A B

Figure 5.3. Pit Milling. Image A shows a pit formed on SS304L. Image B shows the profile of the pit after being cut using a focused ion beam. The pit depth was measured to be 15 µm with a mouth of 5 µm.

Pits also collect corrosive material such as chlorides which increases their concentration. The build-up of corrosion products within a confined spaced can also generate significant stresses. In some rarer cases the excess individual hydrogen atoms from the pitting process may find their way into the metal where they recombine to form hydrogen molecules, creating pressure from within the metal. This pressure can increase to levels where the metal has reduced ductility, toughness, and tensile strength, up to the point where it cracks open. This process is referred to as hydrogen embrittlement and can compound the stresses effecting the steel. Figure 5.4 shows the formation of a crack at the bottom of a pit [42].

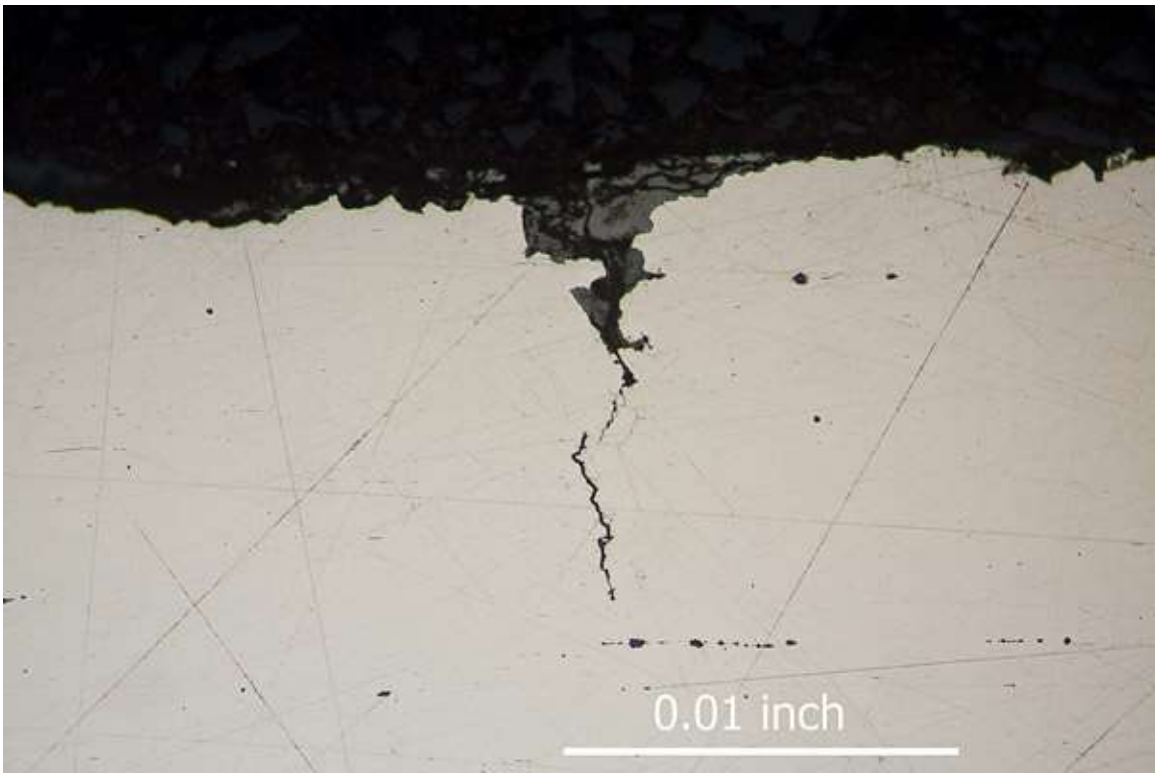

Figure 5.4. Corrosion Pit with a SCC Crack. This image shows a corrosion pit with a SCC crack propagating out of the pit. [42]

Accelerated Testing

Testing of the corrosion electrodes in their target environment would take many years if all geometries were to be accounted for. Instead, a testing apparatus was created to house the corrosion sensor electrode in a very aggressive HCl solution for accelerated corrosion testing. Figure 5.5 shows a cross-sectional rendering of this device which from here on will be referred to as the bathtub.

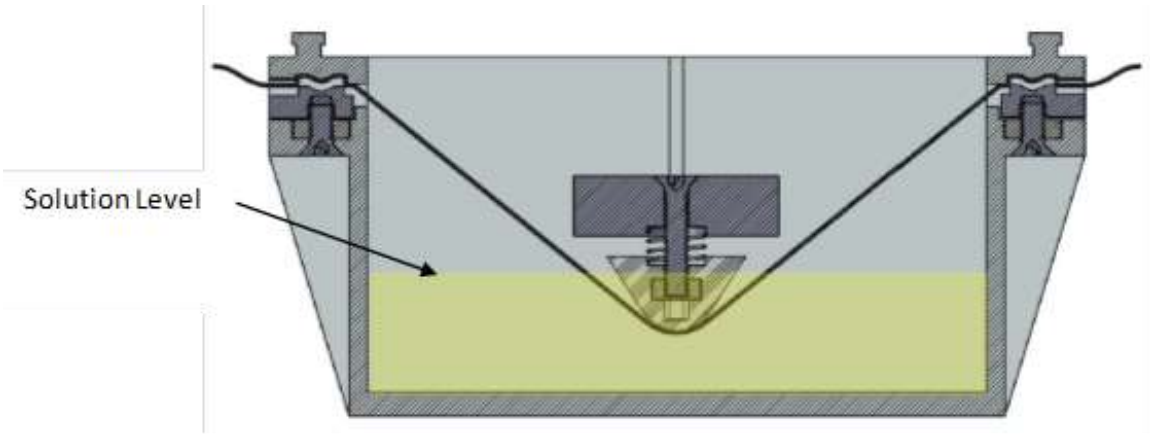

Figure 5.5. Accelerated Corrosion Electrode Tester. A single corrosion test electrode can be placed within this apparatus for corrosion testing.

Similar to the corrosion sensor, the electrodes are placed under constant tension. Earlier versions of the bathtub showed that even if the electrodes had succumbed to a crack, the electrode would fall back together and still remain conductive. The addition of the spring ensures a clean separation and better illustrates the tension on the material when used in a canister. Each electrode is loaded into the tub and clamped down leaving no slack between the clamps. The screw is then released which allows the spring to place a uniform and known amount of force onto the element. A known solution of HCl or NaCl is then poured into the tub to submerge the element, and a four wire ohm meter is used to monitor the resistance as the element corrodes. As time goes on, the resistance of each electrode increases. Figure 5.6 shows a graph of 4 electrode samples being tested concurrently.

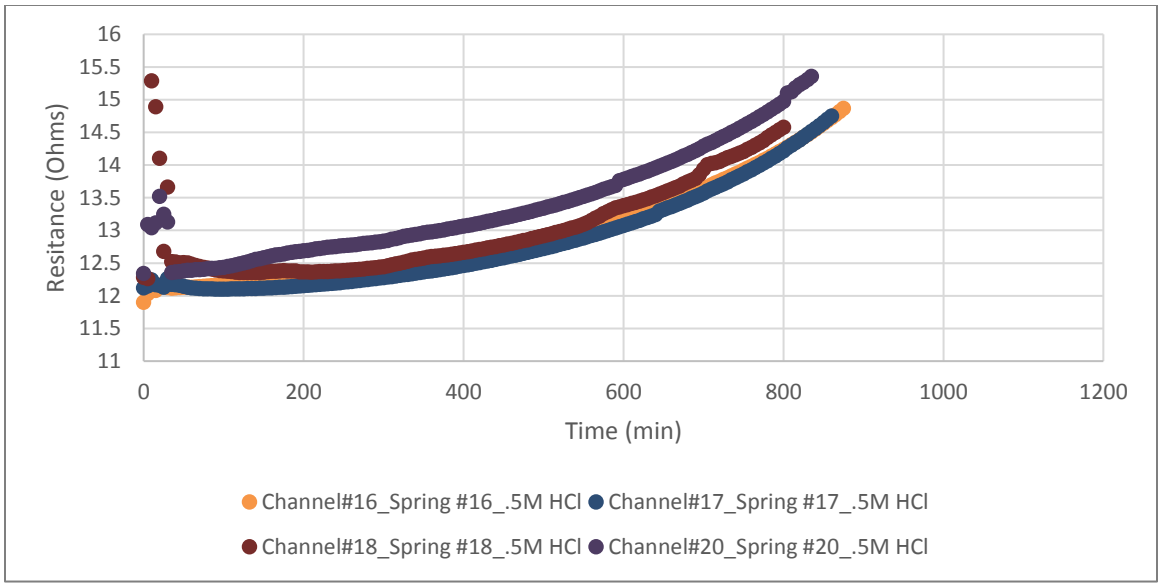

Figure 5.6. Accelerated Corrosion Testing Data: Time to Failure of 4mil SS304 Wires in .5M Solution (3.5M NaCl). Four 4mil wires were tested in the same solution concurrently.

In this graph the resistance values settle between 12 and 13 Ω and then begins to rise exponentially over the next 800 minutes until they begin to fail. Once failed the resistance goes to a theoretical infinity and the wire fully separates. The wires used in the test above were all 4 mils in diameter, but the failure time varied by several minutes. This is most likely caused by the random nature of the cracks formed by the corrosion. Figure 5.7 shows a close-up of a SCC sensor element after it has been broken in an accelerated test.

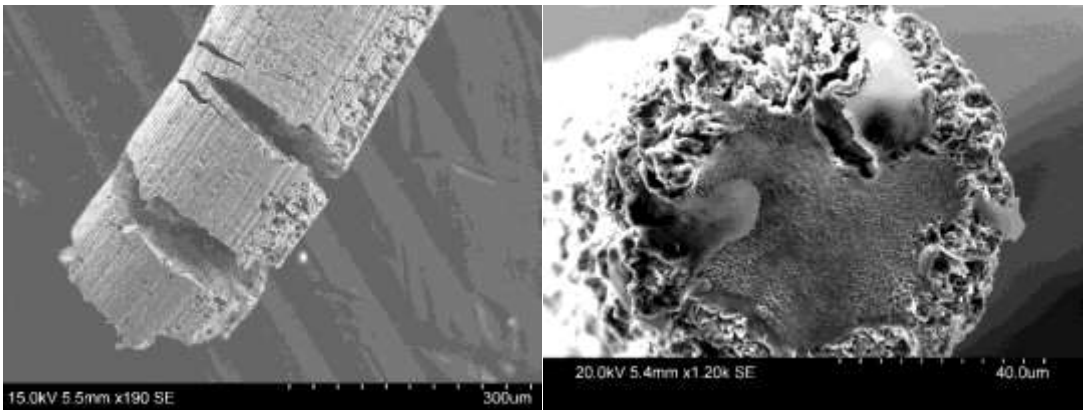

(a) (b)

Figure 5.7. Cracks in Electrode. Taken with a SCM microscope, these images show the cracks formed during corrosion as well as the final break point. (a) shows several cracks formed along a wire. (b) shows the endpoint of the wire.

In the case of stainless steel, the presence of chlorides can initiate crack growth. The higher the localized stress is on surface of the metal the higher the chances of a crack forming. Weld locations are a very common failure point due to SCC because of the residual stress and chromium depletion introduced during the welding process, but even bending points can provide the required start point. Crack growth in stainless steel forms perpendicular to the direction from which the stress is applied. Figure 5.8 below is a finite element analysis of an electrode while under tension by the fully compressed spring.

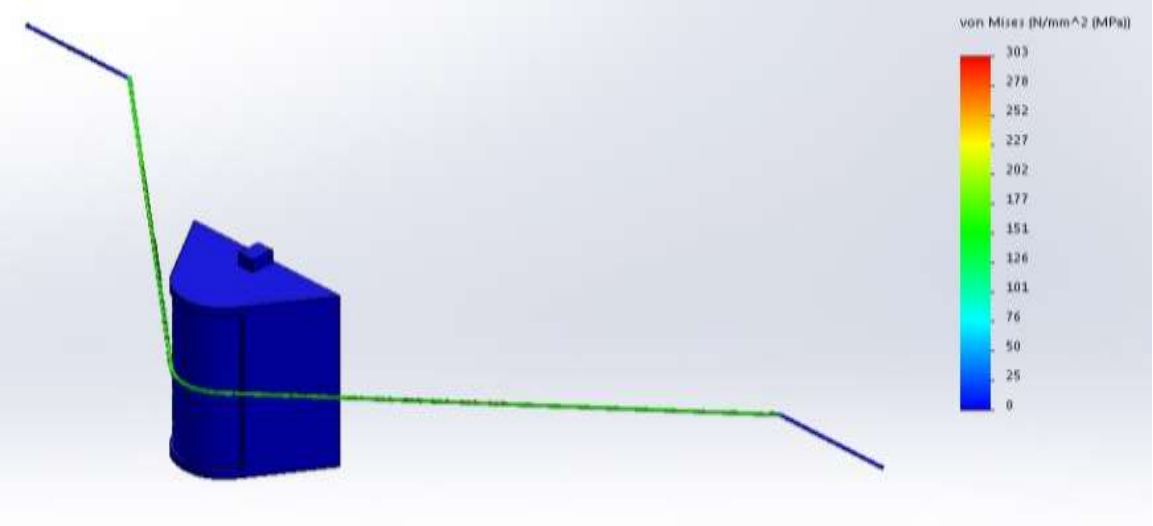

Figure 5.8. FEA of Electrode in Corrosion Sensor. This diagram shows the locations of the highest points of stress on the electrode when it is under tension assuming the element is secure within the holder

The stress on the element is fairly uniform across its length, but during testing, only a small portion of the wire is exposed to the liquid chlorides. This submerged area has the highest chance of forming a crack and breaking. However, great care must be taken to prevent corrosive material from reaching the clamp section which has plastically deformed the wire. This area is also under residual stress, and the oxide layer of the sample may be damaged which would allow for a greater chance of pitting. This can be solved by applying a thin layer of silicone conformal coating to the wire in the clamped area to prevent further corrosion.

The actual fracture in the wire occurs when the cross sectional area of the wire becomes so small that further deformations occur due to the wire tension. Steel is a ductile material, so all deformations beyond the elastic region are plastic in nature. These deformations do not return to their original shape when the material tension is unloaded. When cracks occur, the cross sectional area of the wire reduces until the material surpasses its ultimate strength while under the constant tension. Once this occurs the

electrode will begin necking which rapidly reduces the cross sectional area of the material until a rupture occurs and the electrode breaks.

Resistive Measurements

As shown in the previous section, the cross-sectional area of an electrode becomes smaller as it corrodes and begins to mechanically fail. The amount of current that can flow through an electrode is dependent on its cross sectional area as this directly relates to the electrode's total resistance. The resistance of an electrode depends on its material composition and its shape. The resistance is inversely proportional to the cross-sectional area of an electrode's geometry. For example, a thick copper wire would have a lower resistance than that of an otherwise identical thin copper wire. The resistance of an electrode is proportional to its length; for example, a long copper wire will have a higher resistance compared to that of an otherwise identical short copper wire. This mathematical relationship is expressed in Equation 5.1:

$$R = \frac{\rho L}{A}, \qquad \text{Equation 5.1 [36]}$$

where R is the calculated resistance in Ωs, ρ is the resistivity of the material in Ω-meters, L is the length of the electrode in meters, and A is the cross sectional area in m^2.

If a wire is used as an electrode, then its geometry can be considered to be a long cylinder. In applying Equation 5.1 to this example electrode its material must be defined so the resistivity can be determined. The electrodes used in accelerated testing are a stainless steel ($\rho = 6.90\times10^{-7}$ ohm-meters at 20 °C) wire of five cm length whose diameter is 0.1 mm. This results in a theoretical resistance of approximately 1.098 Ωs. However, when measuring the resistance of a group of 10 electrodes with this geometry using a 4-wire calibrated Ω-meters the average resistance was 12.1 Ωs with a standard

deviation of 0.3 Ωs with no notable outliers. The reason for this difference is due to the crystalline nature of the wire and the grain boundaries within. The resistivity of material is determined by the number of delocalized electrons it has. Grain boundaries in the electrode effectively increase the length of the wire and prevent energy from easily flowing through the material. The electrodes cross section is also in reality not a perfect circle. There are defects all along the length which can either add or subtract to the cross-sectional area of the electrode. A more realistic version of the resistance equation would be shown in in Equation 5.2.

$$R = \int_0^L \frac{\rho}{A(L)} dL, \qquad \text{Equation 5.2 [36]}$$

where R is the calculated resistance in Ωs, ρ is the resistivity of the material in Ω-meters, L is the length of the electrode in meters, and A is the cross sectional area in m^2 and is a function of L.

The function of A(L) will result in the true cross-sectional area at a distance of L from the beginning of the electrode. Unfortunately, it is impractical to solve for this function at it would be different for every electrode.

Resistance measurements are also affected by temperature. The resistivity of a material is directly and proportionally affected by its temperature which is why resistivity values are always given with a specified temperature. The equation for determining resistivity at a temperature is shown in Equation 5.3.

$$\rho = \rho_0[1 + \alpha_0(T - T_0)], \qquad \text{Equation 5.3 [36]}$$

where ρ is the resistivity of the material in Ω-meters, ρ_0 is the resistivity at a reference temperature, α_0 is the temperature coefficient at a reference temperature, T is the target temperature in degrees C, and T_0 is the reference temperature in degrees C.

Substituting Equation 5.3 into Equation 5.2 yields Equation 5.4 below.

$$R = \int_0^L \frac{\rho_0[1+\alpha_0(T-T_0)]}{A(L)}\,dL, \qquad \text{Equation 5.4 [36]}$$

where R is the calculated resistance in Ωs, ρ_0 is the resistivity in Ω-meters at a reference temperature, α_0 is the temperature coefficient at a reference temperature, T is the target temperature, T_0 is the reference temperature, L is the length of the electrode, and A is the cross sectional area in m^2 and is a function of L.

This equation gives a comprehensive method of calculating the resistance of an electrode. As the cross-sectional area of a wire decreases, the resulting resistance will begin to rise exponentially. For instance, if 304 stainless steel wire was used as an electrode (0.05 m long, 0.0001 m in radius, $\rho = 6.90\times10^{-7}$ Ω-meters at 20 °C) then as the wire's cross-sectional area reduced the resulting resistance increase would look like Figure 5.9.

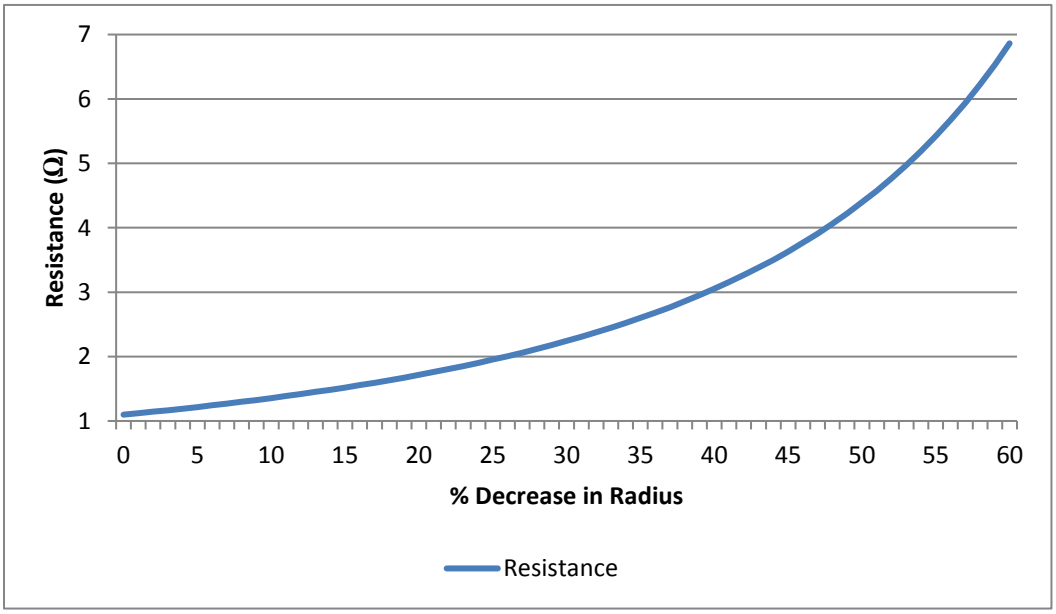

Figure 5.9. Resistance Graph of Ideal Electrode as Cross-Sectional Area Decreases. This graph shows how the resistance of an ideal electrode increases exponentially as its cross-sectional area decreases linearly.

If the shape of this graph is compared to that of the graphs from the accelerated test data, the exponential increase in resistance is present in both. This shows that regardless of the structural differences between the ideal and non-ideal electrodes, the failure mechanism holds, and resistance values will change in the same manner as their cross-sectional areas reduce.

The ideal resistivity of a 304 stainless steel electrode assumes that the entire electrode is a single crystal where there are no grain boundaries such that electrons are uninhibited in their path through the material. Even if this was true, the moment any plastic deformation occurred to the electrode, the perfect crystal shape would be destroyed and the overall resistance of the electrode would increase. From a practical standpoint it is assumed that all electrodes are made of grains of smaller crystals and that these grains have boundaries or gaps between them. Figure 5.10 shows an example of the microcrystalline structure of steel [43].

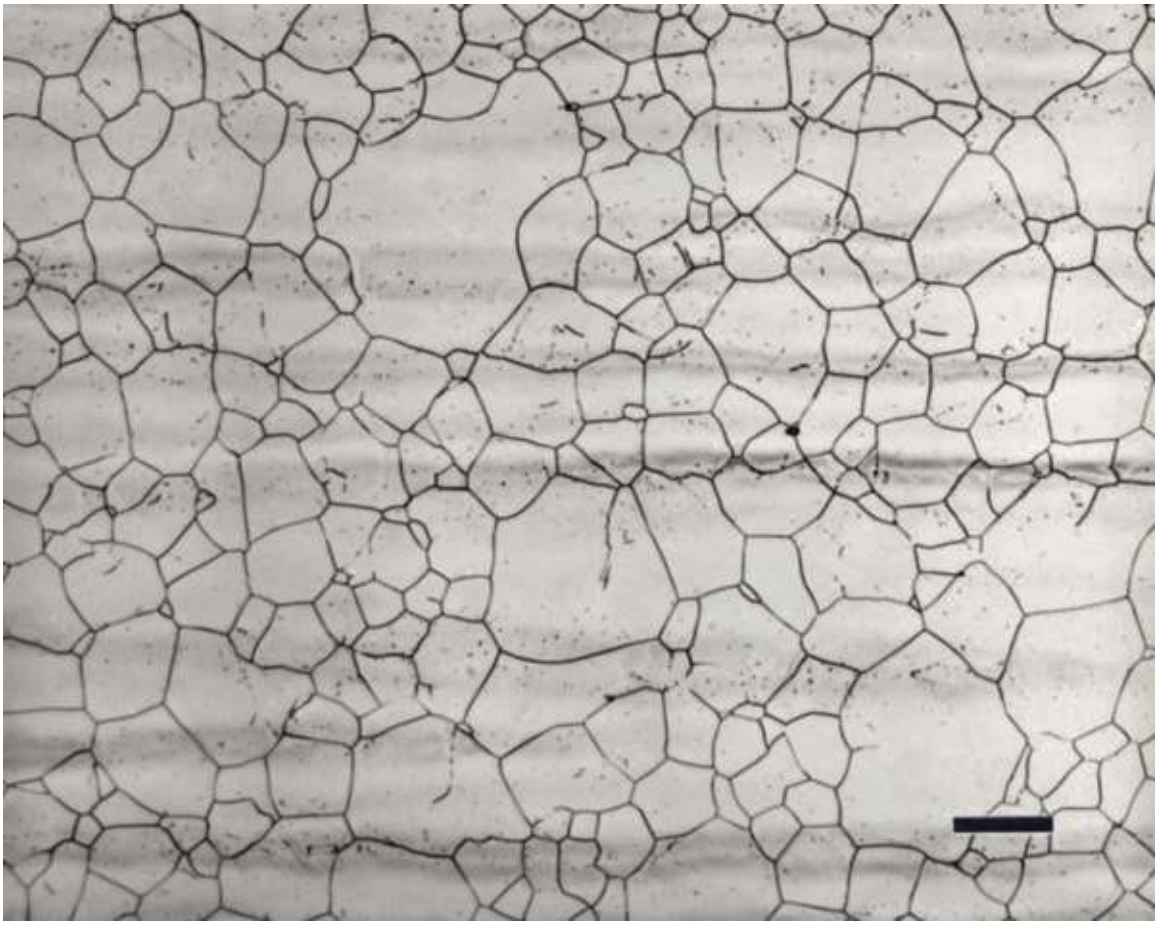

Figure 5.10. Example of Grain Boundaries in 316L Stainless Steel. The image shows the various grains and grain boundaries within a piece of etched 316L stainless steel. [43]

Electrons attempting to pass through the material will move along the path of least resistance through the labyrinth of grains. This effectively increases both the resistivity (ρ) and the distance to travel (L) of each electrode. Figure 5.11 shows these differences between ideal and non-ideal resistance.

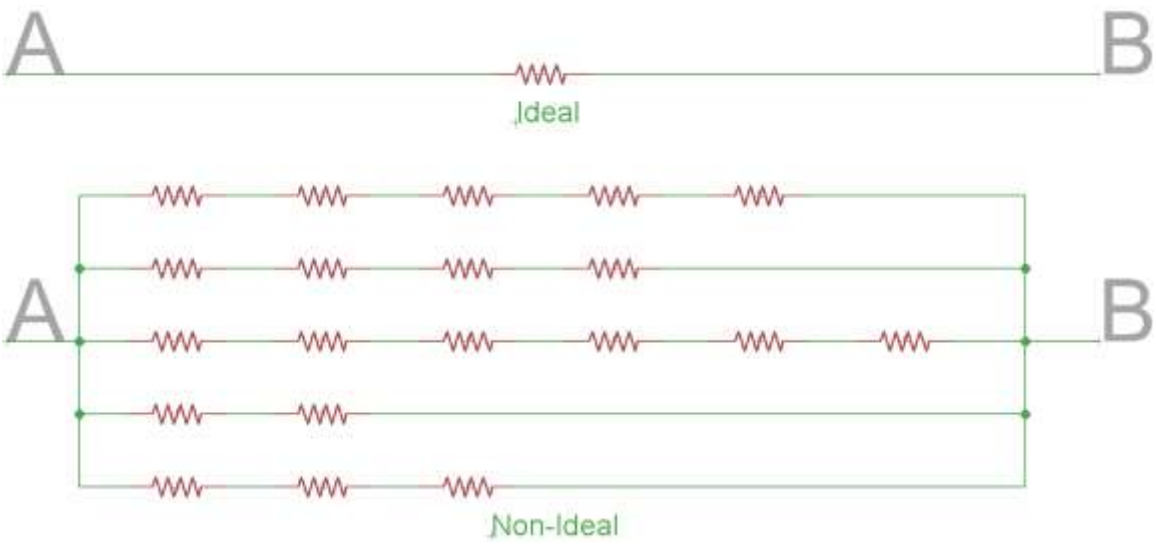

Figure 5.11. Circuit Diagram of Ideal and Non-Ideal Resistances. The ideal circuit is shown above and the non-ideal is shown below. Ideal resistance can be easily quantified as all paths though the material are the same. Non-ideal resistance can be seen as multiple parallel paths with varying lengths and resistivity.

In Figure 5.11, electrons are flowing from A to B. In the ideal circuit there is only a single crystal lattice, and therefore, there are multiple parallel paths for the electrons to take that are all the same length and resistivity. In the non-ideal circuit there are multiple paths in parallel, but each path has a unique length and resistivity. Should a path need to cross a grain boundary from one crystal to another, then the resistance between each grain would need to be accounted for. This results in a resistor network that when reduced, is equal to the true non-ideal resistance of an electrode. Since every electrode has a unique microcrystalline structure, it is assumed that each electrode has a unique resistance. It would also be assumed that this uniqueness would be the root cause of the random failure rate of electrodes with similar geometries.

Corrosion reduces the effective radius of the electrode at one point across the entire length of the electrode. For the purposes of the corrosion sensor this should be indicated by a small increase in resistance per crack. If equation 5.2 is applied to this situation then a corrosion event located at L will result in a smaller Area A(L) at L.

Depending on the amount of corroded material relative to the dimension of the wire, this will result in a varying increased resistance. Smaller dimensioned wires will have a more pronounced increase while larger wires will have a negligible increase. Using Equation 5.4, Figure 5.12 shows what a simulated corrosion event would do to a wire of similar dimensions as described in Figure 5.9 (0.05 m long, 0.0001 m in radius, $\rho = 6.90\times10^{-7}$ Ω-meters at 20 °C) if the resistance values were sampled at regular intervals.

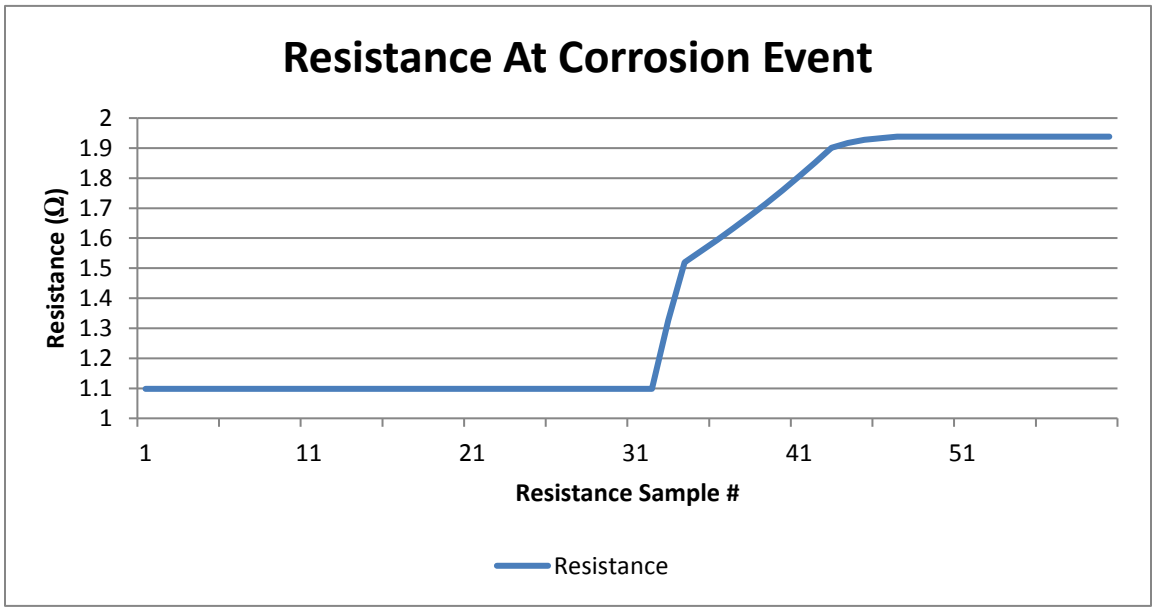

Figure 5.12. Resistance at Corrosion Event. The graph shows the jump in resistance caused by a corrosion event within an electrode. Resistance sampled at regular undefined intervals.

It is clear in this diagram that the resistance increases quickly and then slowly settles into a steady value. What is assumed is occurring is a relatively quick corrosion event causing the initial spike in resistance followed by a strain relieving plastic deformation of the wire. In order to detect the occurrence of a corrosion event from this information it is helpful to look at the mathematical derivative (δ) of the resistance data with respect to sample number pictured in Figure 5.13.

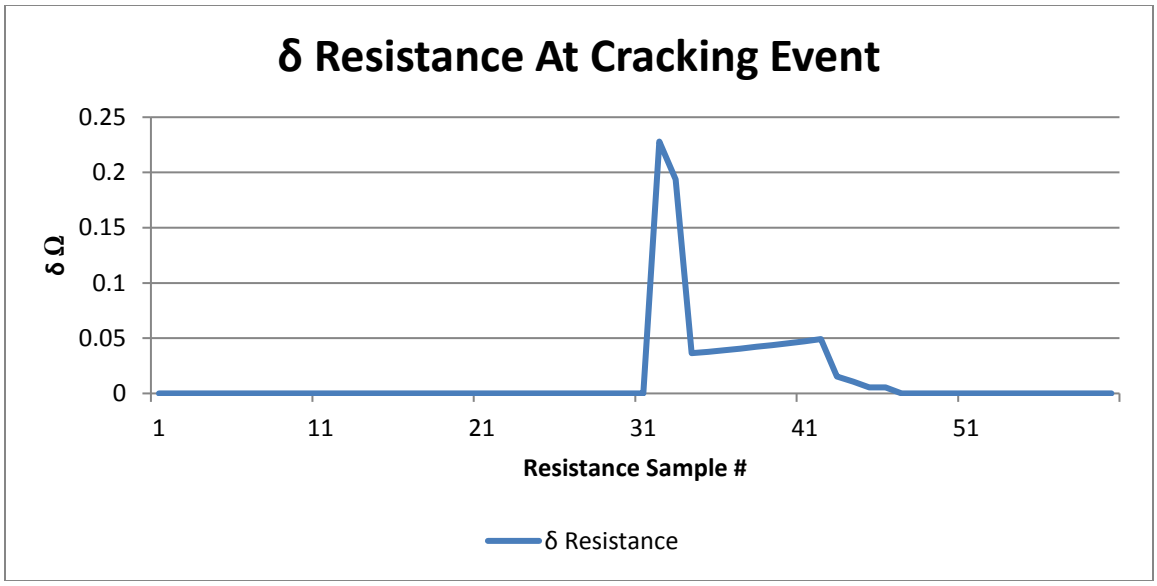

Figure 5.13. δ Resistance at Cracking Event. The graph shows the mathematical derivative of the data in Figure 5.12. The spike indicates the presence of a cracking event.

The spike in the rate of change in resistance indicates that a corrosion event has occurred, and the subsequent strain relieving period can be seen in the samples following the spike. Monitoring the resistance of each electrode for this pattern will reveal if corrosion has occurred. A small electrode geometry will have a larger jump in resistance when corrosion occurs while a larger electrode geometry will have a much smaller jump in resistance. Therefore, each electrode geometry should have a threshold value that indicates when corrosion has occurred.

Mechanically this pattern will not hold for the entire length of the electrode's life. Each electrode is loaded into the corrosion sensor under tension to provide a suitable environment for corrosion growth. However, as the electrode corrodes and with each subsequent plastic deformation the tension on the electrode is relieved. This relief occurs faster in smaller geometries such as wires and slower in larger geometries such as strips. It is possible for the tension to relive it to the point where the wires may no longer be under any kind of strain which would no longer simulate the expected conditions of a

weld joint. With this in mind, wire geometries should be monitored for a one time increase in resistance, and subsequent events should be handled as an unknown condition and ignored. Strips, however, will not be affected in the same way and can be monitored for multiple events.

An underlying fact that cannot be escaped when dealing with corrosion is the random nature in which it occurs. Two similar electrodes exposed to the same environment may corrode at totally different times due to the probability of chlorides being deposited in the exact right place on the surface of the strained steel such that a pit can form. In essence, several things with their own random probability must coincide for corrosion to occur, and therefore, any meaningful output from this sensor system must be in the form of a probability rather than a hard indication that corrosion has occurred on a canister weld.

Curve Model

Sensor fusion is a process by which data from several similar or different sensors are "fused" to compute something more reliable than could be determined by any one sensor alone. It is sensor partnerships or data groupings readily available in this sensor system that will help provide additional information about the environment that a single sensor could not. For example, Equation 5.4 helps compensate resistance measurements for temperature changes, something that neither sensor could do on its own. There are several more theoretical interactions of sensors that need to be proven that will help forecast the rate of corrosion. These sensors are the atmospheric corrosion sensor, the time of wetness sensor, and the humidity sensor.

Stainless steel corrodes in the presence of chlorides, and this process is accelerated in the presence of water, however water alone will not corrode stainless steel. For instance, TYPE I ultra pure water (Milli-Q water) will not react with the passivation layer or chromium oxide in stainless steel. Assume rain falls on the corrosion sensors on the first day they are deployed, and the atmospheric corrosion sensor registers no change even though the time of wetness and humidity sensors are registering high values. This would mean that no noteworthy amount of chlorides have been deposited onto the corrosion sensors and no corrosion has occurred. However, a few weeks down the line after chlorides have been deposited on the corrosion sensors via atmospheric deposition and it rains, there would then be noteworthy reading on the atmospheric corrosion sensor, and from that point one could then assume whenever the time of wetness sensor or the humidity sensor registered a higher than normal reading that the rate of corrosion had increased. These sensor interactions can be used to determine the probability that corrosion could potentially form on the corrosion sensors as well as the weld joints the sensor system is monitoring. In order to generate this probability, an event detection framework needs to be created to monitor for patterns such as these to provide additional data beyond the scope of any individual sensor.

The goal of the corrosion sensor event detection system is to provide a framework for recognizing and alerting users to an event that has occurred on the canister. Currently, should an event occur a user would have to monitor the data coming from all the sensors on the system and interpret what bearing that data had on the health of the canister. If multiple sensor systems are placed in different locations around the canister, then a user would have to correlate the data from each sensor system. The goal of this framework is

to assist the diagnosis of the corrosion rate of the canister and monitor the progress of corrosion within each of the corrosion sensor electrodes and, therefore, the canister surface. As such, the framework must have the following features:

- The ability to detect an event in real-time
- A pattern of sensor activity that leads to each event
- A method of generating a probabilistic estimate of how much corrosion has occurred
- A method of alerting a user as to when an event has occurred

Events on the system could be defined as an electrode breaking or the first sign of activity on the atmospheric corrosion sensor indicating the presence of corrosive substances on the canister. Patterns that lead to this activity could be increases in moisture with the presence of chlorides or the slow increase of resistance on a corrosion electrode.

Generating a probabilistic model of how much corrosion has occurred will require analysis of experimental data within an environmental chamber. Event detection and patterns that lead to event detection will play a key role in determining the rate at which the electrode is corroding. Table 1 shows some of these relations.

Table 2. Event Detection Patterns. This table shows some of the theorized interactions between the sensors that can be used to determine the rate of corrosion. All integrals are taken with respect to time(t).

Sensor	Type of Data	Relation to the Rate of Corrosion
Atmospheric Corrosion (C)	Current from galvanic sensor indicates presence of chlorides and corrosion	$\int_0^t Cdt$
Time of Wetness (TOW)	Boolean data that defines if the corrosion sensors are wet or not. Should the atmospheric corrosion sensor be active at all over the lifespan of the sensor system then this should increase the rate of corrosion	$\int_0^t Cdt * \int_0^t TOWdt$
Humidity (RH)	Relative humidity that determines how much moisture is in the air. Should the atmospheric corrosion sensor be active at all over the lifespan of the sensor system then this should increase the rate of corrosion	$\int_0^t Cdt * \int_0^t RHdt$
Temperature (T)	Temperature increases the rate of chemical reactions. Should chlorides be present and enough moisture is present as well the rate of corrosion should increase.	$T*\left(\int_0^t Cdt * \int_0^t TOWdt + \int_0^t Cdt * \int_0^t RHdt\right)$

Each of the equations in the table above relates to a sensor pattern that will cause an increase in the rate of corrosion of the corrosion sensors. Each integral is taken with respect to time since the longer the system runs the higher the chance of corrosion occurring. A final culminating equation would be presented as a probability density function (PDF) that would report the odds of corrosion occurring on the surface of the canister within a set limit.

An example of how these equations relate can be understood by comparing the prerequisites of stainless steel corrosion with the available sensors. Corrosion requires the

presence of both water and a corrosive material such as a chloride. The resistance of the electrode should remain unchanged should neither of these be present. By integrating the atmospheric corrosion sensor readings over time (atmospheric corrosion equation from Table 1), the amount of corrosive material buildup on the sensor node can be monitored. By comparing the amount of moisture present to the amount of corrosive material (TOW and RH equations from Table 1), a corrosion coefficient can be calculated which can be used in the creation of the PDF function.

The PDF function will provide the probability of surface corrosion based on the experimental data models and field measurements. A probability model was chosen to estimate the amount of corrosion due to the random nature of its formation combined with inconsistencies in the manufacturing of the electrode material. Once a measurable amount of corrosion is detected by any of the sensors, a PDF curve can be generated based on all data available to date. Figure 5.14 shows an example PDF curve for a 1000 day estimation.

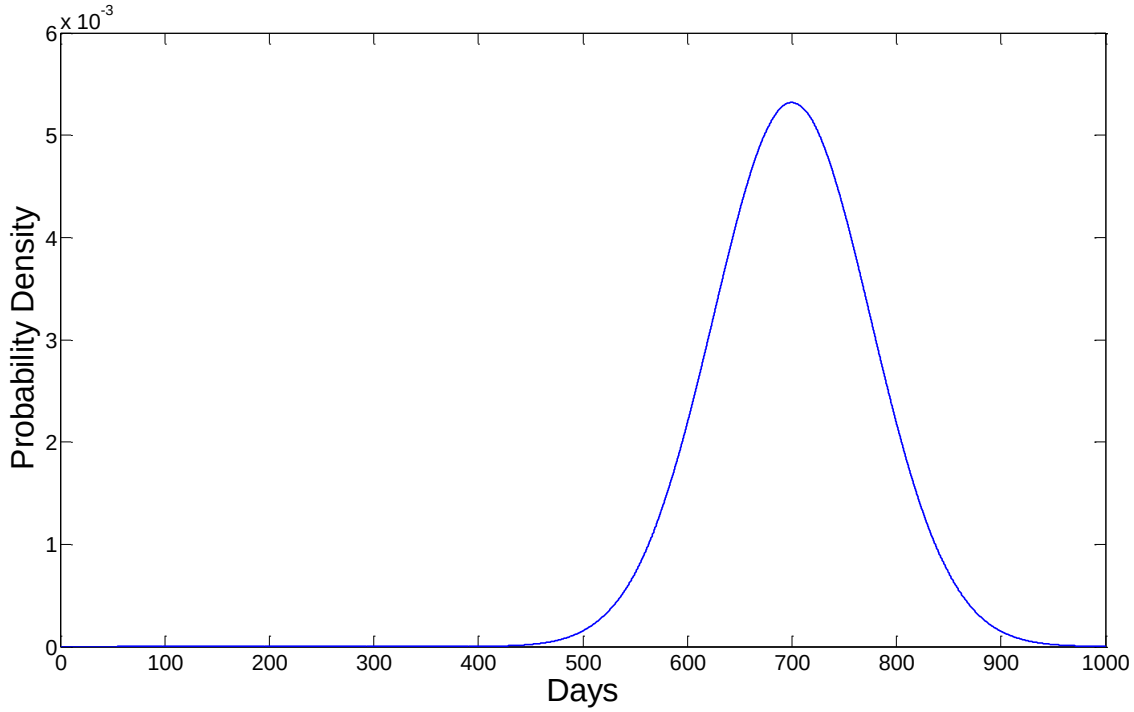

Figure 5.14. Example PDF Curve. This image shows a PDF curve for a 1000 day estimate.

According to Figure 5.14 the probability of the electrode failing in the next 500 days is 0.38% should no further events occur. However, if an event does occur, such as more activity on the atmospheric corrosion sensor, then the PDF would update with this new data. The resulting shift in the PDF curve would be similar to Figure 5.15.

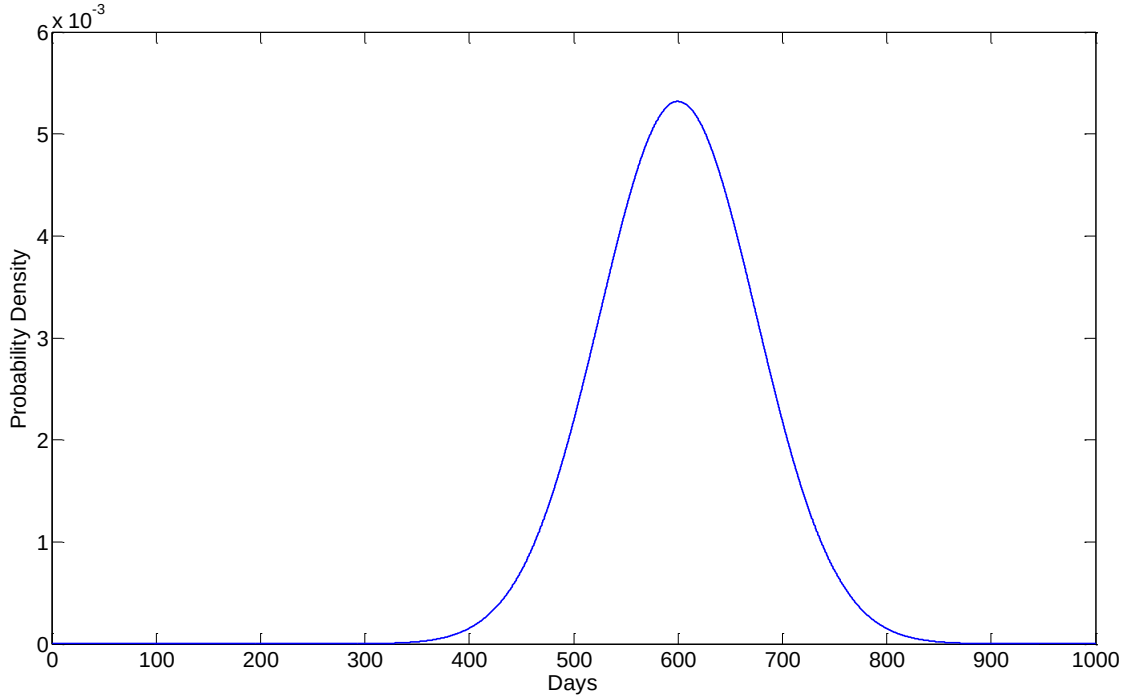

Figure 5.15. Updated Example PDF Curve. This image shows a PDF curve for a 1000 day estimate after additional corrosion was detected.

This additional sensor activity has increased the probability of the sensor failing in the next 500 days to 9.11%. As new events occur the mode of the function (highest point) will move further left on the PDF graph. This is representative of the electrode corroding and the probability of it breaking increasing as corrosion occurs and as time passes.

As Table 1 demonstrated, multiple sensors need to be consulted simultaneously, and past values need to be considered to determine the probability of corrosion. Each sensor monitors a different element in the environment, and it is only when these elements come together in certain order and strength do the right conditions appear for corrosion to occur. The following sections will discuss each of the sensors and the order in which each of them must detect their specified environmental element.

Atmospheric Corrosion Sensor

The atmospheric corrosion sensor is used to detect the presence of corrosive materials in the environment such as sodium chloride and is much more sensitive to the effects of corrosion than the stainless steel canister. The primary function of this sensor is to determine if these corrosive chemicals are present which will then allow the sensor system to determine if corrosion is even possible. For instance, if the corrosion sensor never detects any amount of corrosion, it is safe to determine that the necessary conditions for corrosion to occur have not been reached, and the probably of the canister failing due to corrosion is 0% (within reason). This would also mean that any of the other sensor's readings will not contribute to corrosion as the necessary materials needed for corrosion are not present. An example would be if the canister was rained upon continuously in a region not close to a large body of salt water. The TOW sensor and humidity sensors would register an ample amount of water, but without the presence of chlorides the stainless steel will not corrode.

The amount of corrosive material deposited on the sensor will increase the rate of corrosion of the sensor and, therefore, generate more current. If the amount of current generated by the sensor is integrated over time, then the total amount of corrosion of the sensor can be monitored. The higher this integrated value gets the higher the probability that corrosion on the canister can occur. Figure 5.16 shows what the total assumed probability would be if no corrosion was present on the atmospheric corrosion sensor.

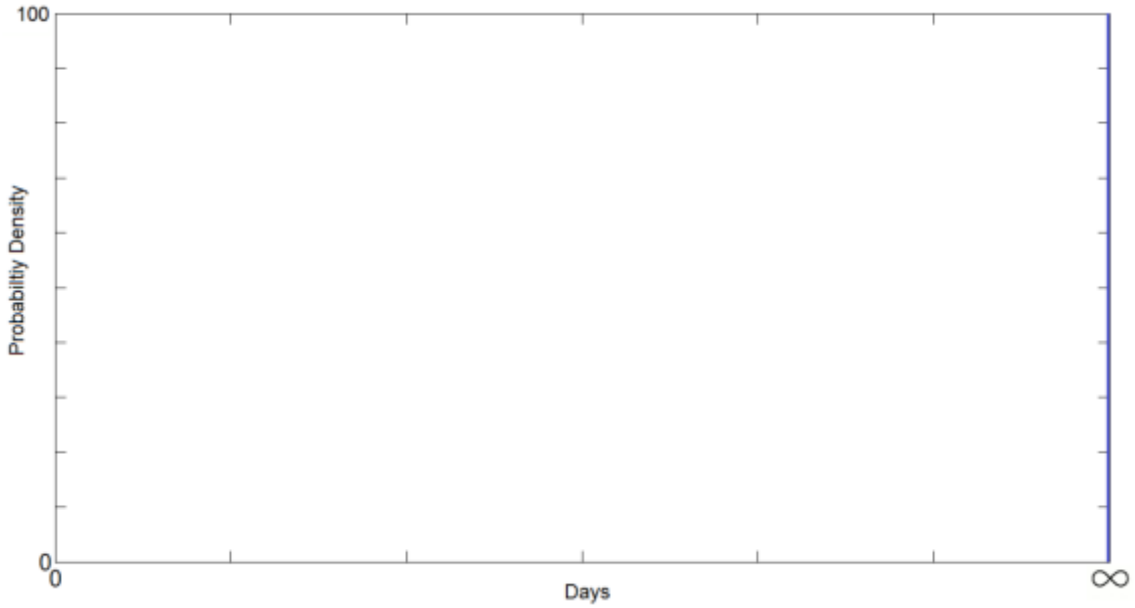

Figure 5.16. PDF When No Corrosion Has Occurred On the Atmospheric Corrosion Sensor. This PDF shows that the probably of corrosion on the canister is 0% in the near future and 100% at infinity.

The integral of a PDF over its range of values must be equal to 1, but in the case of Figure 5.16 the probability of the canister corroding over any time in the near future is 0% due to the lack of chlorides. The very farthest point in time of the graph must contain all of the probability that this event will occur in order to meet the requirements of the graph. This is the best way to show zero probability of an event with this type of graph. Once any amount of atmospheric corrosion is detected, however, the topography of this graph changes and the bell curve topography appears. Figure 5.17 shows what the PDF function will look like once activity of the atmospheric corrosion sensor has been detected.

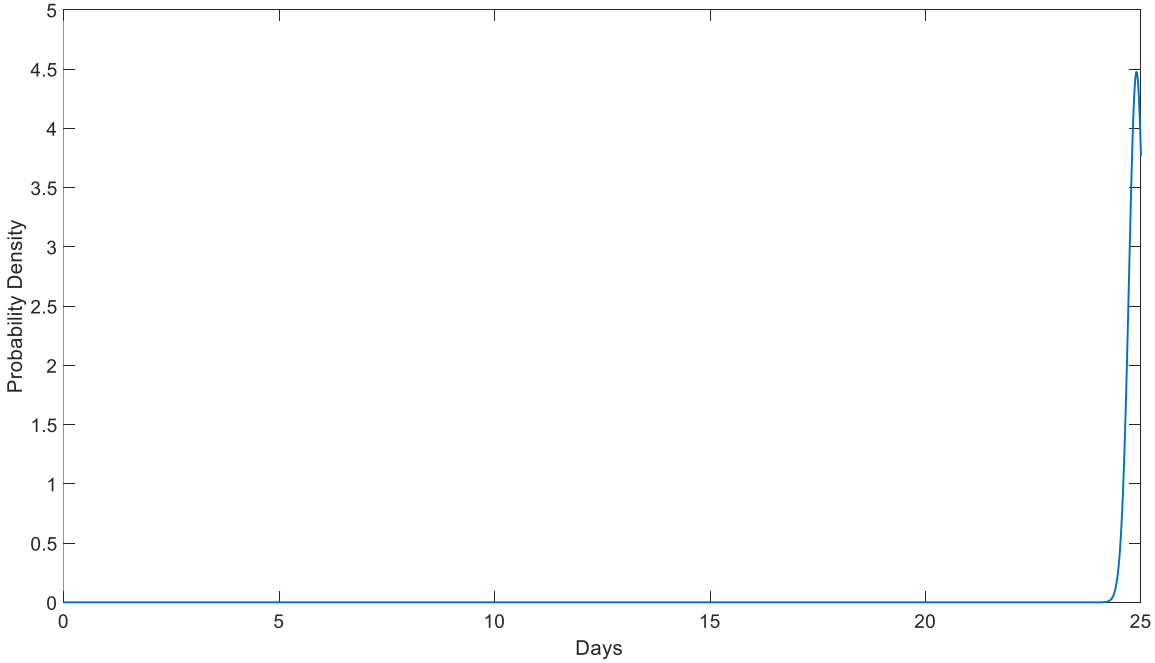

Figure 5.17 PDF Once Initial Activity on Atmospheric Corrosion Sensor Is Detected. This PDF graph shows that the probability that corrosion will occur on the canister has increased and the amount of time before it occurs has drawn closer.

The bell curve shows that the probability of corrosion on the canister has increased and the median of the curve now represents the estimated time in which it will occur. Since the corrosion is random in nature and the failure time of the stainless steel is not constant, a bell curve properly represents the possibility that the actual event of corrosion may occur before or after the median of the curve. It should also be noted in this curve (Figure 5.17) that the Days axis is no longer going from 0 to infinity, because it is assumed that this corrosion will continue and the steel will eventually fail. The maximum time of 25 days was chosen as an arbitrary end point.

In order to detect the onset of corrosion, the Atmospheric corrosion sensor must be monitored for current spikes, which would indicate that portions of the sensor have made contact. This would then indicate that an aggressive corrosive agent is present and

would also be the first event of note for the sensor system. This will be indicated by the following equation:

$$\delta C_{Thresh} > (C_t - C_{t-1}), \quad \text{Equation 5.5}$$

Equation 5.5 indicates the conditional where a corrosive substance has been detected. C_t and C_{t-1} are consecutive corrosion current samples and δC_{Thresh} is the current threshold at which the event occurs. After this event occurs, then the value of C should be integrated via the equation in Table 1.

Humidity Sensor

Airborne vapor can contain more than just water especially in marine environments. The humidity sensor can monitor the relative humidity of the canister environment but will not determine what other chemicals are mixed in with the water vapor. The surface temperature of the canister can be very high which would cause most liquid forms of water to evaporate quickly. This additional water in the air will condense on any airborne particulates and can subsequently deposit the particulates on the canister surface. In marine environments these particulates can contain sea salt which will attack the passivation layer of the stainless steel. The additional water in the air will slow the rate of aeration of the steel and, therefore, prevent repassivation of the steel.

Humidity alone cannot initiate corrosion without the presence of chlorides and, therefore, should not be taken into account until after the atmospheric corrosion sensor has registered the presence of chlorides. After this event, however, it can be assumed that chlorides have been deposited on the surface of the canister and the water vapor in the air can condense on the canister which may lead to corrosion. The relative humidity will vary over time as water is introduced and removed from the canister environment. By

integrating the relative humidity sensor readings with respect to time after the presence of chlorides has been detected the cumulative effect of the water vapor in the canister environment can be accounted for. Equation 5.6 shows a modified version of the equation from Table 1 that includes this requirement.

$$Total\ Relative\ Humidity = \int_{Ct_0}^{t} RHdt, \quad \text{Equation 5.6}$$

Equation 5.6 shows the calculation of the relative humidity concentration over time starting from Ct_0 (time at which δC_{Thresh} is reached). As new sensor readings are taken after atmospheric corrosion has been detected, this integrated value will increase and can be directly compared to previously captured data to produce a PDF.

Time of Wetness

The dew point of water vapor is defined as the temperature at which the air must be cooled to be saturated. Below this temperature, the water vapor in the air will condense to form liquid water. The time of wetness sensor will detect this condensation and monitor the length of time it remains on the surface of the canister. If the atmospheric corrosion sensor has detected corrosive elements in the canister environment then the condensation event has provided the optimal environment for corrosion to occur. The condensed water will prevent the repassivation of the oxide layer of the stainless steel which will allow chlorides to deposit within direct contact of the pure stainless steel. This process can lead to galvanic corrosion and the formation of a pit. Equation 5.7 shows a modified version of the equation from Table 1 that includes this requirement.

$$Total\ Time\ of\ Wetness = \int_{Ct_0}^{t} TOWdt, \quad \text{Equation 5.7}$$

The time of wetness sensor represents the point where the relative humidity is considered a saturated value and therefore no longer relevant. At this point corrosion is not guaranteed, but it does represent a condition in where it is highly likely and only adds to the probability of it occurring. Figure 5.19 shows how the PDF is affected by the presence of condensed water.

Calculating Probability

In order to calculate probability of when one of the sensor elements will break, there needs to be previous data to compare to. For instance, if the resistance at which a particular type of sensor element breaks is a known value with a statistically low standard deviation, one could actively compare a similar sensor element to that data and estimate when it will fail. Broadening this to also include the amount of corrosion, humidity, and time of wetness will improve the accuracy of the prediction.

The resistance PDF calculation can be performed by first gathering experimental data from a known sensor element geometry. If several sensors are corroded and all have similar resistance profiles with similar breaking points, then an average (μ) and a standard deviation (σ) can be calculated from that data. This in turn could be applied to a normal distribution PDF calculated as follows in Equation 5.8.

$$f(x|\mu,\sigma^2) = \frac{1}{\sqrt{2\pi\sigma^2}} e^{-\frac{(x-\mu)^2}{2\sigma^2}}, \qquad \text{Equation 5.8 [44]}$$

Figure 5.18 shows a graph of sample resistance data from 3 sensor elements as they corrode over time.

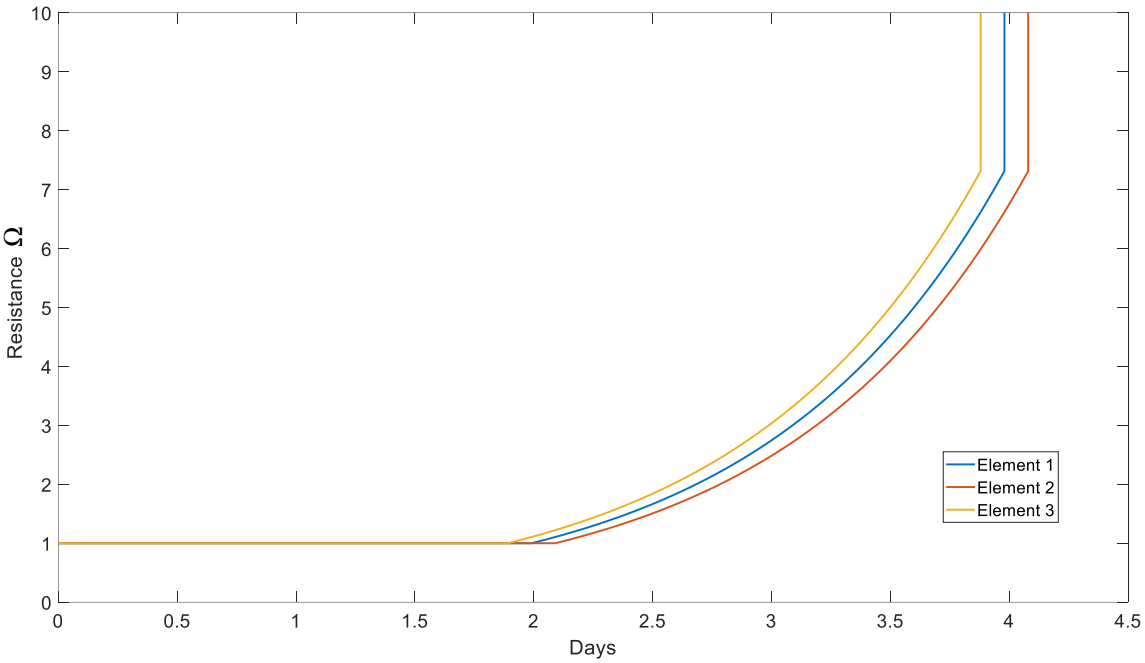

Figure 5.18. Sample Resistance Data for 3 Sensor Elements

The sensor elements in Figure 5.18 all begin at 1 Ω and break around 7 Ωs, but all break at different times. The standard deviation for these break times is 0.1 Days making the variance (σ^2) 0.01 Days. Appling this data to Equation 5.8 and using 0 as the mean, the PDF plot in Figure 5.19 was generated.

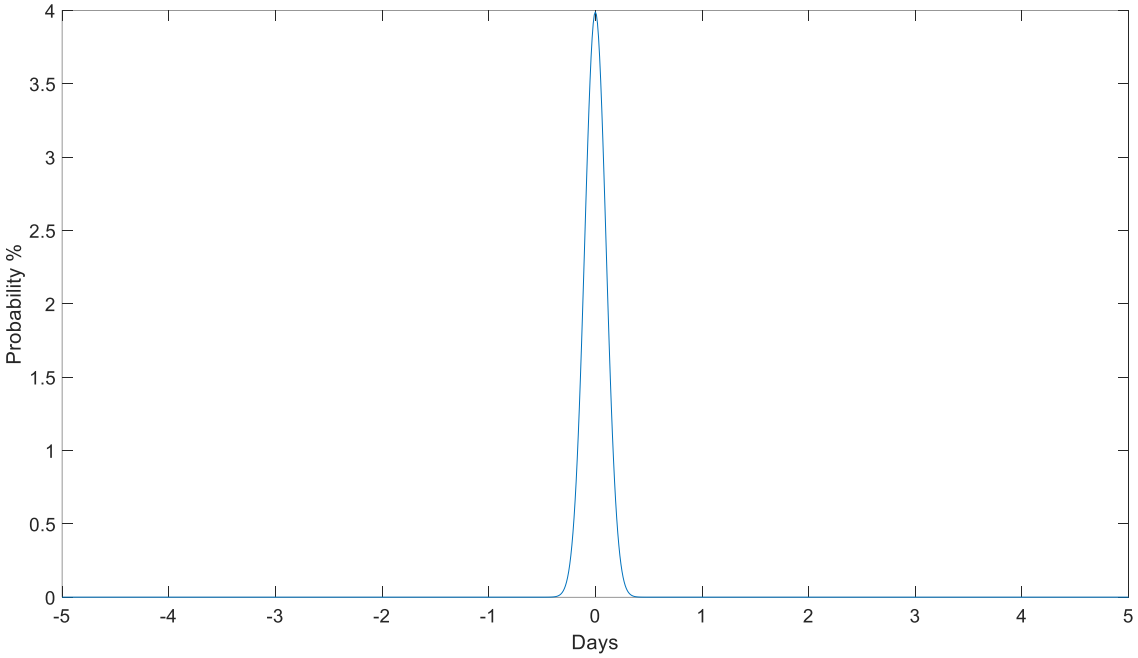

Figure 5.19. PDF Plot of Sample Resistance Data from Figure 5.18.

This distribution can be used to determine the probability sensor failure by using the average break resistance of the sensor element and the progression of that element. For instance, assume Element 1 from Figure 5.18 was being monitored as live data. On day 3 the corrosion process has begun, and the resistance has increased by approximately 2 Ωs. Using the calculated distribution from this data, the probability of the sensor element failing within the next few days can be calculated. Figure 5.20 shows the PDF from Figure 5.19 applied to these conditions.

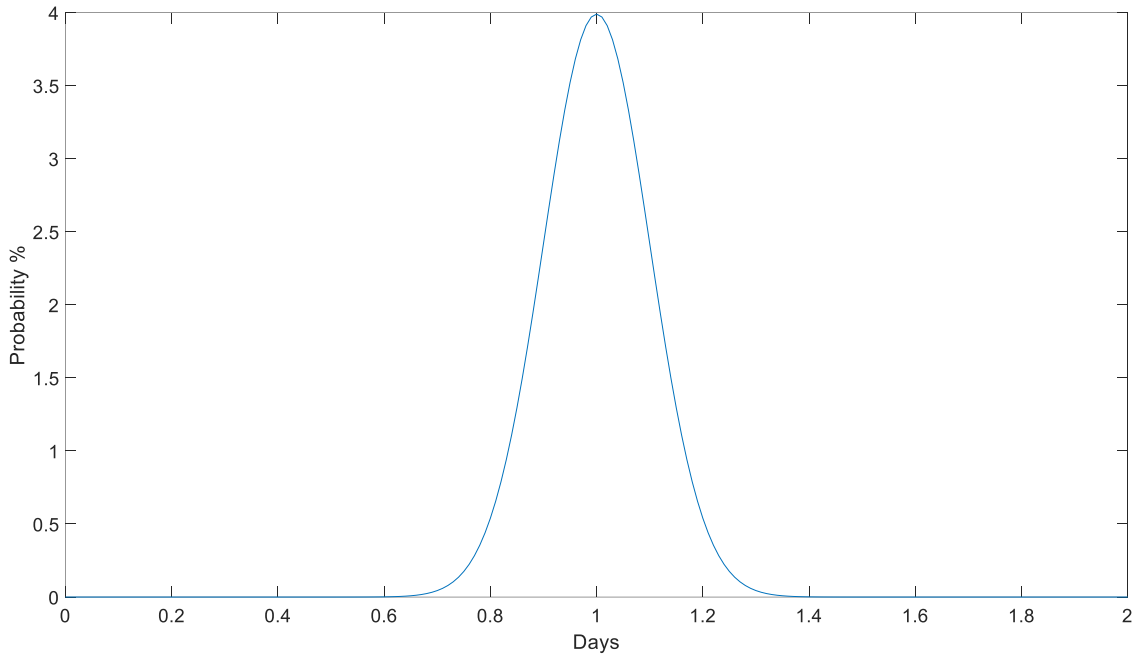

Figure 5.20. PDF Plot of Sample Resistance Data of Element 1 On Day 3 from Figure 5.18.

Figure 5.20 shows the probability of failure of Element 1 over the next 2 days assuming the data is being viewed on day 3. Integrating the PDF from 0 to 0.5 days shows that there is a statically unlikely chance (near 0) the sensor will fail in the next half day. Integrating the PDF from 0 to 1 days shows that there is a 50% chance that the sensor will fail within the next day. Integrating the PDF from 0 to 2 days shows that there is a near 100% chance the element will fail in the next two days. Comparing these probabilities to the data in Figure 5.18 shows a strong correlation.

Expanding this method to other sensor types is possible. If the time of wetness is integrated from the start of the corrosion till the time of each wire break, then the average of these accumulated times can be used to create a PDF. These various PDFs can be combined by adding the sums of the weighted PDFs.

Equation 5.9 shows the summation of the weighted PDFs and the requirement that the sum of the weights (W) must also equal to 1 for the result to be a PDF. The value of n indicates the number of PDFs in the summation.

$$f(x|\mu_i, \sigma_i^2) = \sum_{i=1}^{n} W_i \frac{1}{\sqrt{2\pi\sigma_i^2}} e^{-\frac{(x-\mu_i)^2}{2\sigma_i^2}} \qquad \text{Equation 5.9 [44]}$$

$$\sum_{i=1}^{n} W_i = 1$$

The weights are assigned based on their importance to the current state of the system. For instance, if the TOW sensor is saturated then the amount of humidity in the environment will not have a great effect on the rate of corrosion and should, therefore, be weighted less. If the opposite is true, then the humidity level should weigh more. The resistance of the sensor element provides the most direct measurement of the level of corrosion present and should have the highest weight. This is even more important when the sensor element is approaching the breaking resistance. The majority of the data acquired for this research was done within environmental chambers and the level of relative humidity was kept near 100% for the duration of the test which also saturated the TOW sensor. This was done to simulate a worst case scenario, and so the weights chosen for the PDFs were as follows:

- Resistance: 80%
- TOW: 15%
- Humidity 5%

These values could be changed based on a canister's environment and should be done at the discretion of the canister setup.

CHAPTER SIX: RESULTS

In situ environmental testing was a primary goal for this dissertation as it would experimentally demonstrate the abilities of the corrosion sensor modules and networking electronics. A series of tests were conducted to show the sensor module's environmental resistance and ability to record sensor data under harsh conditions. After each test the results were analyzed and the next test was designed based on those results. This section will cover the goal of each test, the experimental setup, the data recorded, and the analysis of the results for all conducted tests.

Environmental Chamber Test 1

Goals

The first test was designed to verify the sensor system could operate in the expected environment without suffering from water damage. Many of the components inside the sensor systems are sealed against water or other chemicals that may reduce the lifespan of the system as a whole. Long term testing requires proper vetting of the seals and coatings around these parts to ensure the unit will function correctly for extended periods and not fail prematurely thus voiding test data.

Experimental setup

An environmental chamber was used to simulate the needed corrosive environment to initiate corrosion on the sensors. This chamber has the ability to control both humidity and temperature. The model number of this chamber is Delta Design 6400 and is pictured in Figure 6.1.

Figure 6.1 Delta Design 6400 Environmental Chamber. This image is of the environmental chamber used for this test.

The temperature is maintained using a built in feedback controller that uses an electronic relay to turn the chamber heating elements on and off. The temperature can be set using the controls on the chamber panel, and the current chamber temperature is displayed on a readout. The humidity is maintained by an external boiler located adjacent to the chamber. Figure 6.2 show an image of the boiler.

Figure 6.2 Environmental Chamber Boiler. This image shows the boiler used to generate humidity for the environmental chamber used in this test.

The heat for the boiler is controlled by a 220V Watlow heating element located at the base of the boiler. Adjusting the amount of heat generated by the boiler will adjust the humidity in the chamber. The humidity system does not use a feedback controller, therefore manual adjustments are required to change the humidity. To ensure the humidity levels reported by the sensor system were correct, a humidity probe was inserted into the chamber, and a meter was connected to ensure the reported values were correct. This meter is pictured in Figure 6.3.

Figure 6.3 Humidity Meter with Probe. This image shows the humidity meter and probe used to verify the conditions within the chamber.

The sensor system is mounted in a vertical position in the middle of the chamber such that the Ethernet cable points downwards. This cable is then routed out a port on the side of the chamber where a power supply and data logging computer are located to power and record sensor readings from the chamber.

Sensor System Configuration

For this test the sensor system was configured to carry all sensors except for corrosion strip sensors. 4 wire electrodes were loaded onto the sensor system with assumption that they would break quickly. Each wire was coated by paint brush in a saturated NaCl and isopropyl alcohol solution in order to provide the needed chlorides to initiate corrosion. The temperature in the system was set to 70˚C with a relative humidity of 70% with minor adjustments made to maintain these conditions. The length of the test

was set to be until visible heavy condensation formed on the sensor unit and associated warmup and cool down times had passed.

Test Results and Analysis - First Attempt

This test was run twice due to a malfunction with the environmental chamber. All test data was lost from the first run and the sensor system was destroyed within the chamber. Failure analysis of the chamber showed that the temperature feedback controller entered a runaway state where the feedback thermocouple consistently reported a temperature lower than 70˚C which the system was set to. This caused the heating element to remain constantly on which drove the temperature within the chamber above the ratings of many of the materials used to construct the sensor system. The exact temperature is unknown as the chamber was shut down for safety reasons before any readings could be taken. Figure 6.4 shows the remains of the sensor system within the chamber after an extended cool down period.

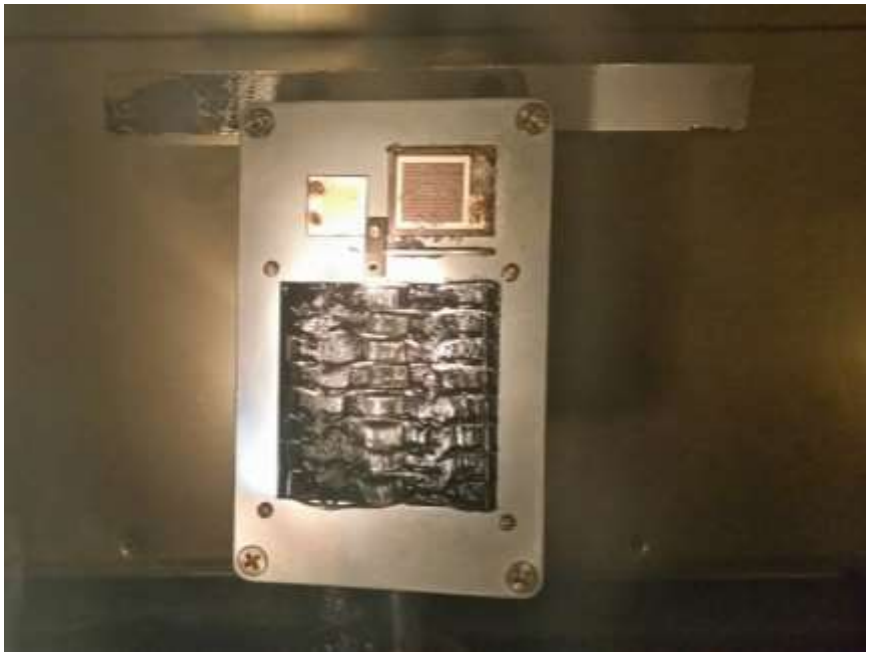

Figure 6.4 Failed Sensor Unit. This imaged shows the remains of the sensor unit after the first environmental chamber test.

The temperature in the chamber reached the point where the SLA reached the melting and combustion point. All materials made of plastic or silicone also reached the combustion point. This combustion destroyed the electronics contained within the system as every PCB surface was covered in silicon conformal coating. After pulling the unit apart it was also found that the temperatures reached the point where the adhesive used in the PCB manufacturing process melted which allowed the copper traces on each PCB to detach causing the electronic components to leave the PCB. The temperatures, however, did not pass the point of melting the solder joints. The need for high temperature PCB material had not been considered at this point and will be addressed in future versions of the electronics. Figure 6.5 shows the remains of the sensor system internals.

Figure 6.5 Failed Sensor Unit Internals. This image shows the internal remains of the sensor unit after failure.

Test Results and Analysis - Second Attempt

The second attempt to perform this test suffered no equipment failures and lasted approximately six hours. The sensor system recorded a sample every two seconds for a grand total of 19534 samples (5.42 hours) which were recorded to an external laptop. The chamber was set to 70˚C with a relative humidity of 70% at the start of the test and allowed to come up to temperature before the sensor unit was inserted, and the chamber was turned off after 4 hours.

The atmospheric data collected is shown in Figure 6.6. The control loop on the boiler can be seen in the oscillating pattern of the relative humidity signal.

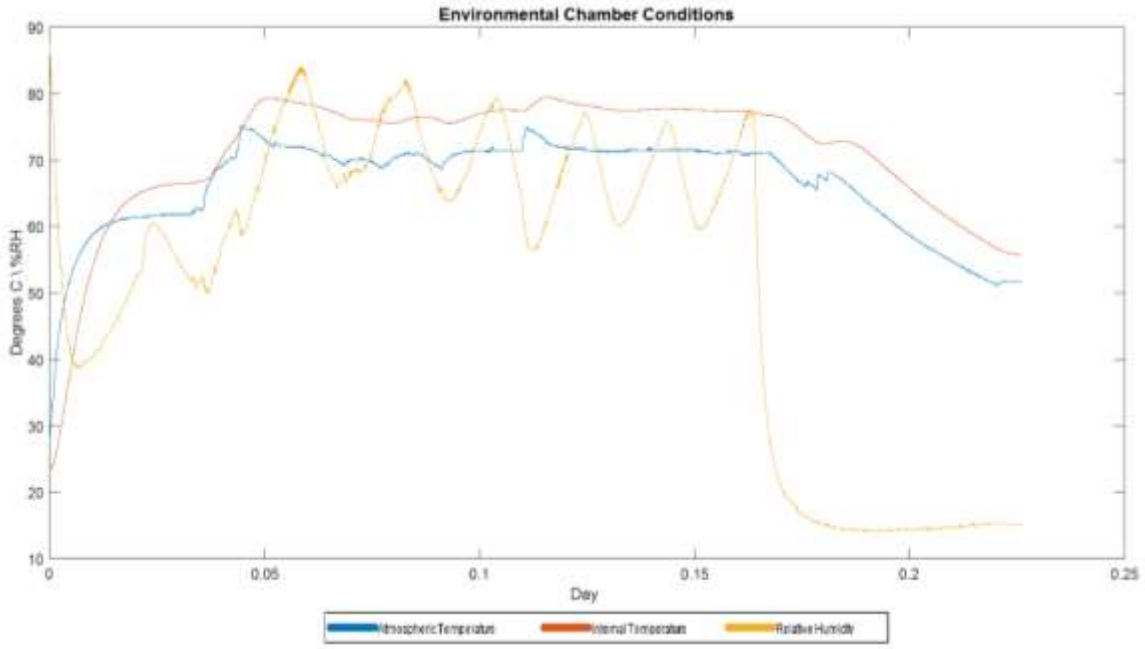

Figure 6.6 Environmental Chamber Conditions During Second Chamber Test. This image shows the atmospheric and internal temperature of the sensor unit as well as the relative humidity.

The humidity level dropped after the chamber was opened for the sensor unit to be inserted. The humidity in the chamber returned quickly and the relatively cold metal

of the sensor unit quickly attracted condensation as is shown by the TOW sensor data in Figure 6.7.

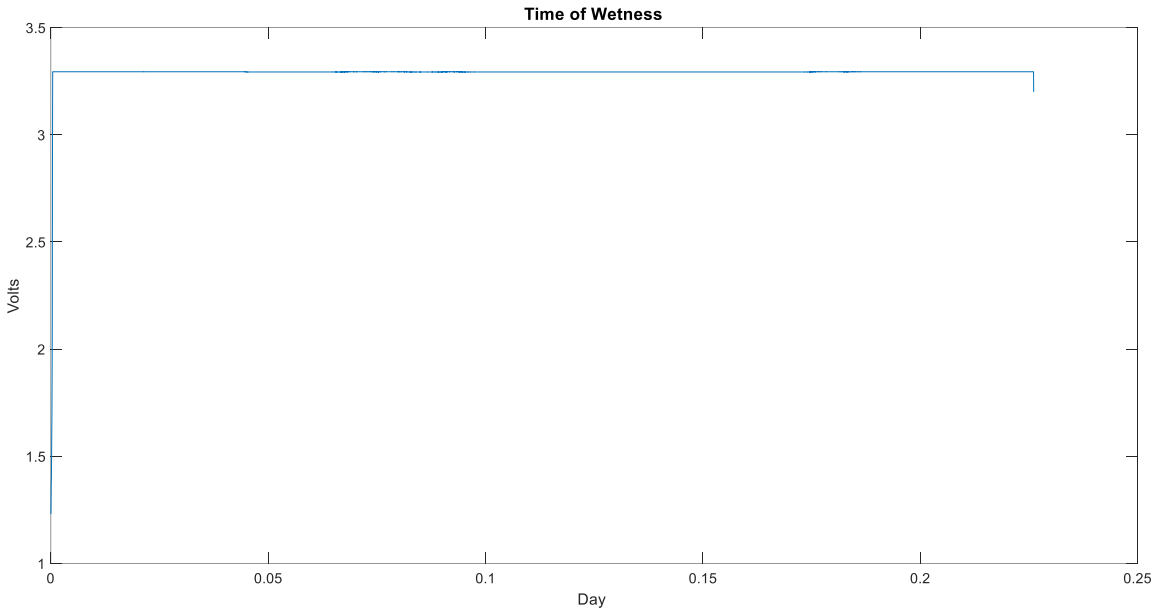

Figure 6.7 Time of Wetness Data During Second Chamber Test. This image shows the data from the time of wetness sensor is saturated at all times except for the beginning and end of the test.

The time of wetness data shows that the sensor was saturated within two minutes of entering the chamber and remained so until the door of the chamber was opened.

The short duration of this test and the lack of chlorides introduced to the chamber resulted in little to no activation of the atmospheric corrosion sensor, but did reveal a flaw in the sensor system design. The resistance sensors did not have good data come through due to thermal expansion of the sensor elements causing intermittent contact on the wire terminals. This was solved by incorporating a conductive adhesive to the wire terminals and strip pads to improve their ability to move with the thermal expansion and keep a constant electrical contact.

This test shows that the electronics and communications of the sensor module can survive and operate with the environment of the test chamber and longer tests can be done. The sensor system seals also survived this test and had no sign of water breaching.

Environmental Chamber Test 2

Goals

With the eventual success of the first test, the second test was designed to quickly initiate corrosion to ensure that the sensor system would correctly operate when exposed to chlorides. The fastest way to initiate corrosion is expose the sensor unit to a concentrated chloride solution and provide the needed environment for corrosion to occur.

Experimental setup

The environmental chamber was changed to an ESPEC BTL-433 which was directly connected to a DI water supply in order to reduce maintenance. This chamber allows for the control of both temperature and humidity and is programmable for a variety of test sequences. A sensor module was mounted inside the chamber for testing which is pictured in Figure 6.8.

Figure 6.8 ESPEC BTL-433 Environmental Chamber. The new environmental chamber is shown on the left and the mounted sensor system is shown on the right.

The sensor module was loaded with four 127um wires to expedite the test. All sensors were repeatedly coated in a supersaturated salt and isopropyl alcohol solution in order to deposit chlorides directly onto the corrosion and corrosion sensors. In addition, the module was sprayed with an ASTM D 1141 synthetic sea water solution to simulate rain and deposit additional corrosive material.

Test Results and Analysis

The test lasted 17 days and all 4 sensor elements corroded and broke. During the test the temperature and humidity levels were adjusted at the beginning of day 2 to increase the amount of condensation on the sensor elements to improve the odds of corrosion occurring. Figure 6.9 shows a graph of the environmental conditions in the chamber during the test.

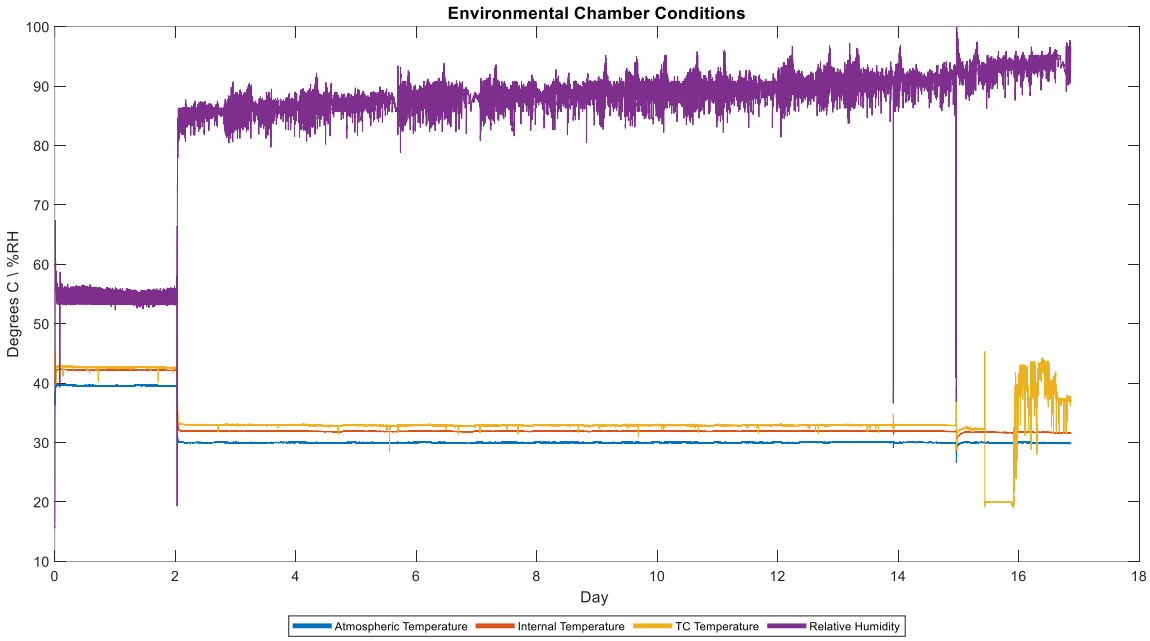

Figure 6.9 Environmental Conditions Within the Chamber. At day 0 the temperature was set to 40˚C and humidity was set to 55 %RH. On day 2 this was adjusted to 30˚C and 90 %RH.

Figure 6.9 shows a single change in the environmental settings over the course of the test which resulted in an increased humidity level. The noise visible on the humidity data is periodic and is introduced by the chamber's PID controller in an attempt to keep the humidity constant. The chamber itself has a humidity and temperature readout which is routinely compared to the sensor module's readings to ensure the chamber is running at the desired settings. The opening and closing of the chamber causes immediate dips in the temperature and humidity and can be seen throughout the plot. At day 15 the sensor system was sprayed again with the synthetic sea water and the external TC failed due to wire corrosion caused by a faulty silicone seal, which was reinforced in the future tests.

The corrosion sensor performed well over this time and indicated the presence of chlorides the moment the sensor system was turned on. Over the 17 days the current generated by the sensor was integrated and produced the following graph in Figure 6.10.

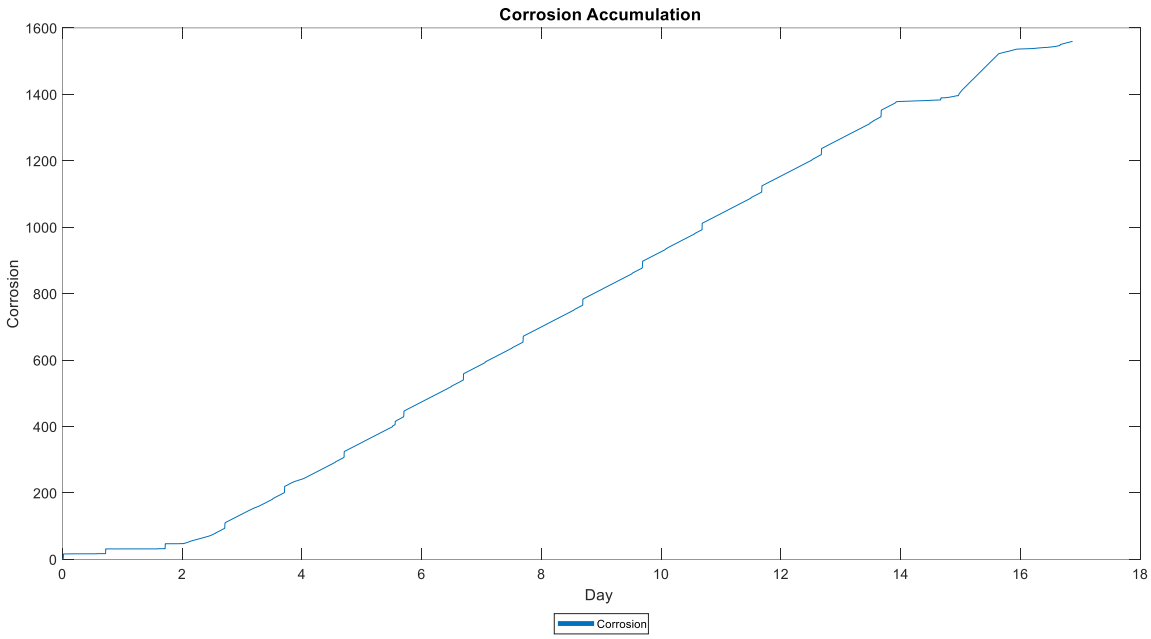

Figure 6.10 Corrosion Sensor Output. The graph shows the integrated current (corrosion) from the current sensor over the 17 day test.

The galvanic senor immediately produced a small amount of current when the system was first sprayed with the synthetic sea water and by day 3 was producing a near constant amount of current that can been seen in the slope of the line. This trend appears as if it will continue well past the 17 day mark indicating the lifespan of this sensor is longer than the length of this test.

The TOW sensor also worked well over the test and showed that the amount of condensation forming on the sensor itself was not very high. The humidity in the chamber was very high, but the saturation of water in the air was not high enough for the sensor to trip. Figure 6.11 shows the data from this sensor.

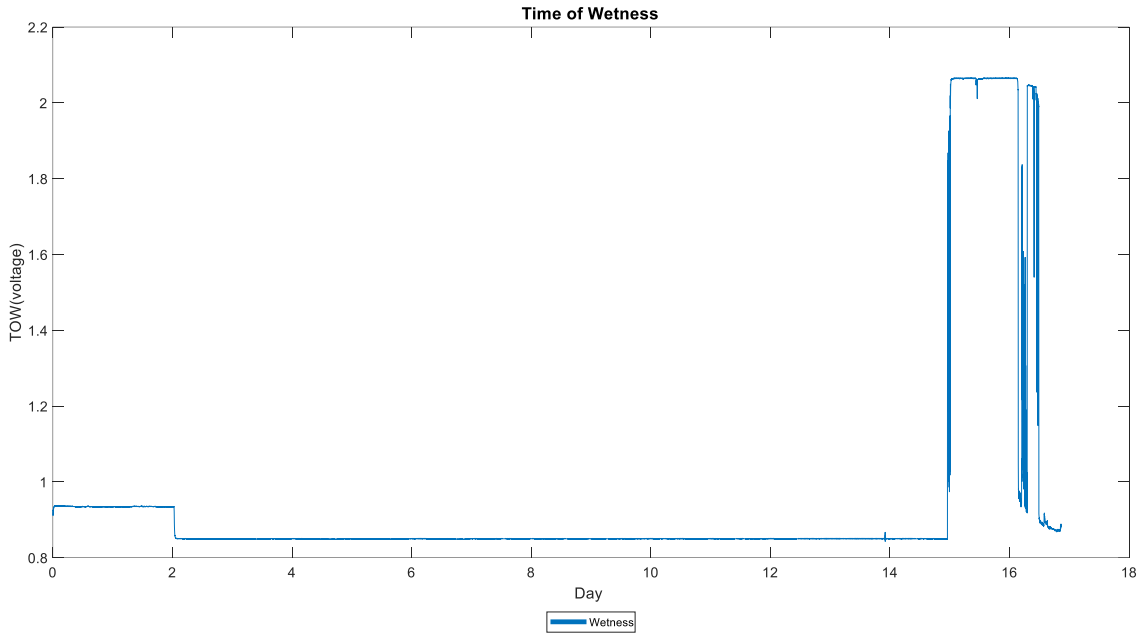

Figure 6.11 TOW Sensor Output. The graph shows the voltage read from the TOW sensor over the 17 day test.

On day 15 the sensor system was sprayed with synthetic sea water which immediately appeared on the TOW sensor as expected and remained wet for a whole day. This indicates that if condensation forms in the chamber at these settings that it will evaporate very slowly and not remain. The chamber needs an adjustment in settings to ensure the sensor system remains saturated with water.

The corrosion sensors broke within an hour of the second synthetic sea water spray on day 15. This however did not happen as planned. As Figure 5.8 shows, the location of the stress placed on the sensor element is concentrated on the bump and at the clamping points. The clamp areas also provide a space for the sprayed material to congregate and prevents evaporation while the bump provides neither. Figure 6.12 shows a comparison of the corrosion sensors before the test and after the test.

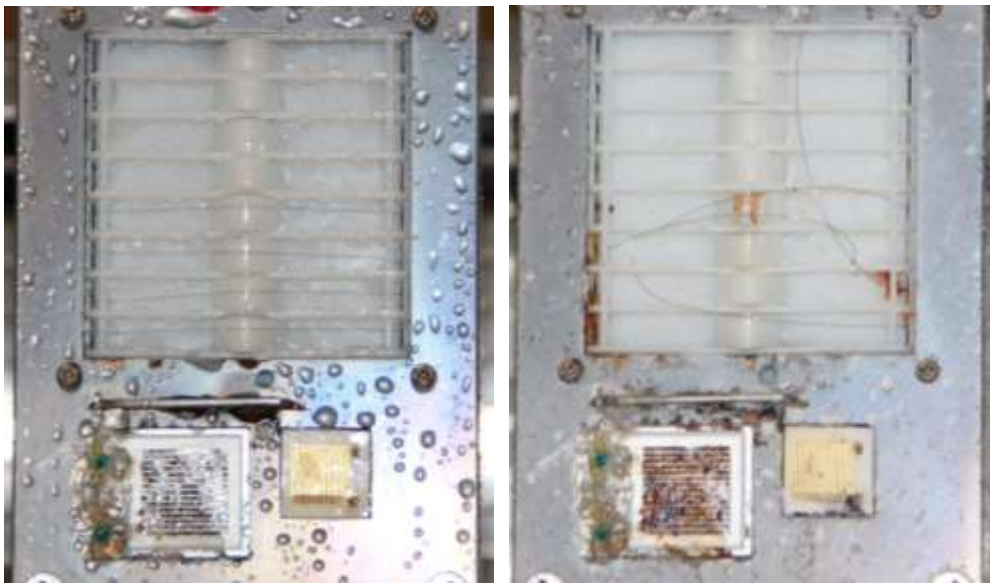

Figure 6.12 Sensor System Before and After Test. The image on the right shows the sensor system at the beginning of the test after it is sprayed with synthetic sea water. The image on the left shows the sensor system at the end of the test.

None of the sensors have broken at the desired bump location, and in some cases the broken wires have electrically shorted together which has corrupted the sensor data. This problem was fixed by adding a silicone seal to the clamp area preventing both water and chlorides from reaching the clamp area. The data from the corrosion sensors was, however, a complete waste as it did show that all the wire sensors broke at nearly the same time. Figure 6.13 shows the data from these sensors.

Corrosion Sensors

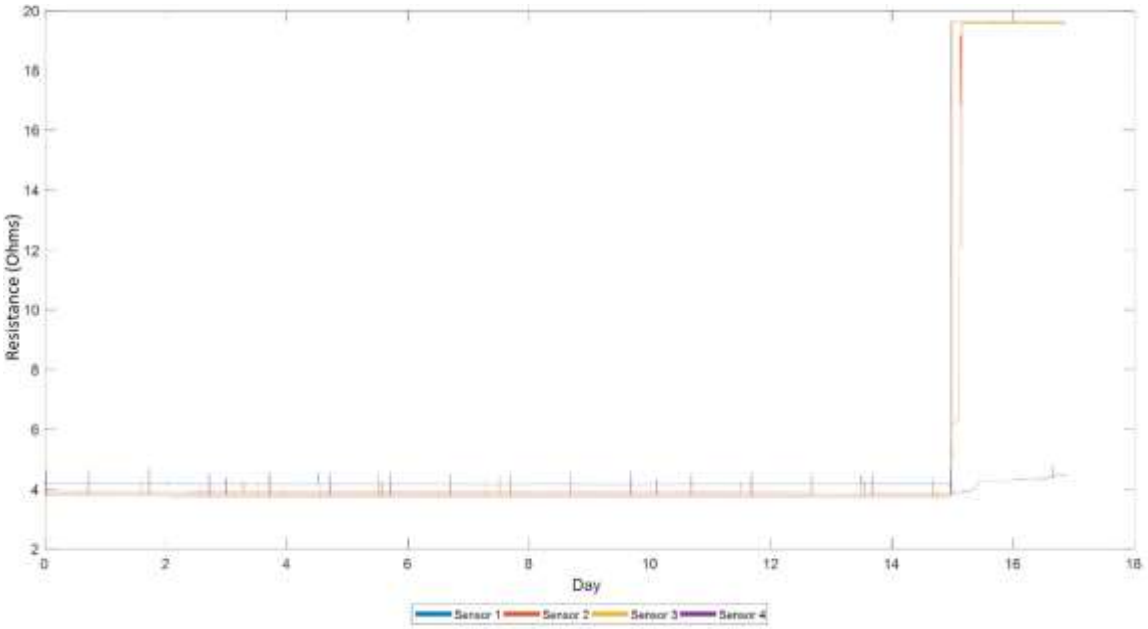

Figure 6.13 Corrosion Sensor Data. The graph shows the resistance measurements from the 127um wire corrosion sensors over the 17 day test.

The data in Figure 6.13 shows that the sensors maintained their resistance for 14.96 days before any major change occurred. The TOW sensor shows that the sensor unit was sprayed at approximately 14.91 days. Figure 6.14 shows a zoomed in section of this graph detailing this interesting period.

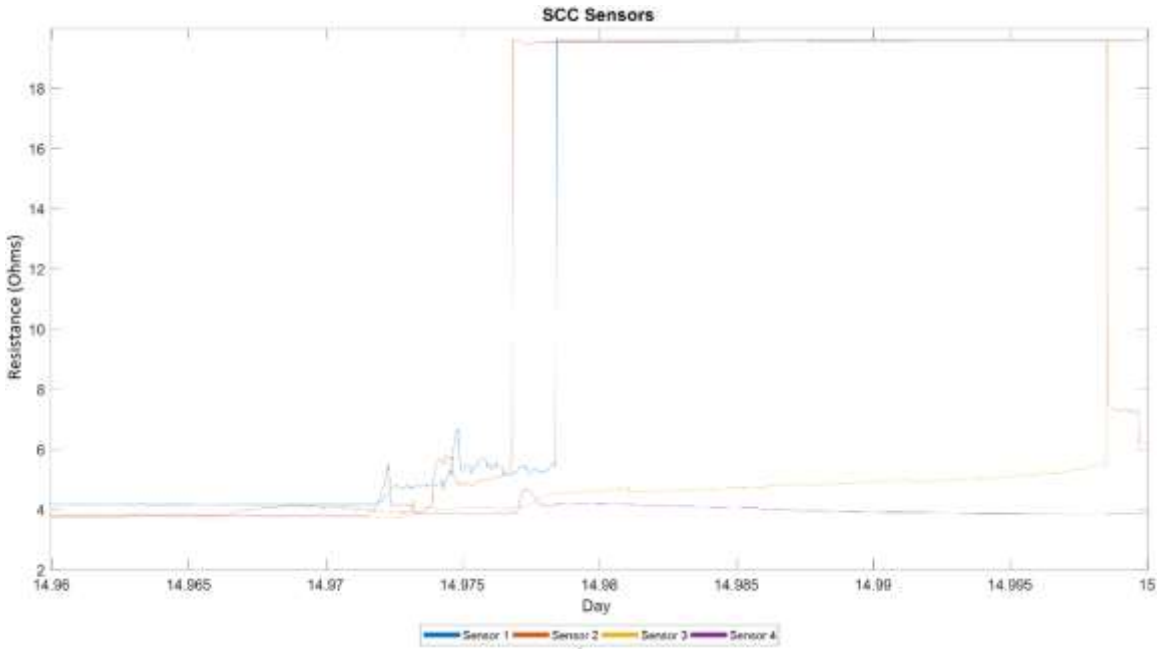

Figure 6.14 Corrosion Sensor Data Breaking Point. The graph shows the resistance measurements from the corrosion sensors near the breaking point.

From Figure 6.14 sensor 2 breaks first and is followed by sensor 1 a few minutes later. Sensor 3 breaks a few minutes after that, but shorts to sensor 2 at which point all data from Sensor 2 and 3 becomes invalid. Sensor 4 breaks 10 hours (Day 15.44) later and shorts to the case ground making its data invalid from that point. Three of the sensors broke within an hour of each other which is a very promising data point, however none of them broke in the anticipated way which points to a stochastic behavior.

Environmental Chamber Test 3

Goals

After several iterative improvements for both long-term survivability and accuracy, the first long term test for the sensor module was attempted. This test was designed to replicate the installation and operation of the sensor module on a canister. The sensors would not be pretreated with chlorides, but rather exposed to corrosive material within the chamber. From previous data gathered from the accelerated corrosion

testing it was estimated that this test, if not subject to premature failure, would last several months. This test would also serve to test the predictive model's accuracy and ability to detect events.

Experimental setup

The ESPEC BTL-433 environmental chamber was again used in this test, and the same mounting mechanism was put in place. The sensor load out was changed to have both 127um wires and 127um thick strips as shown below in Figure 6.15.

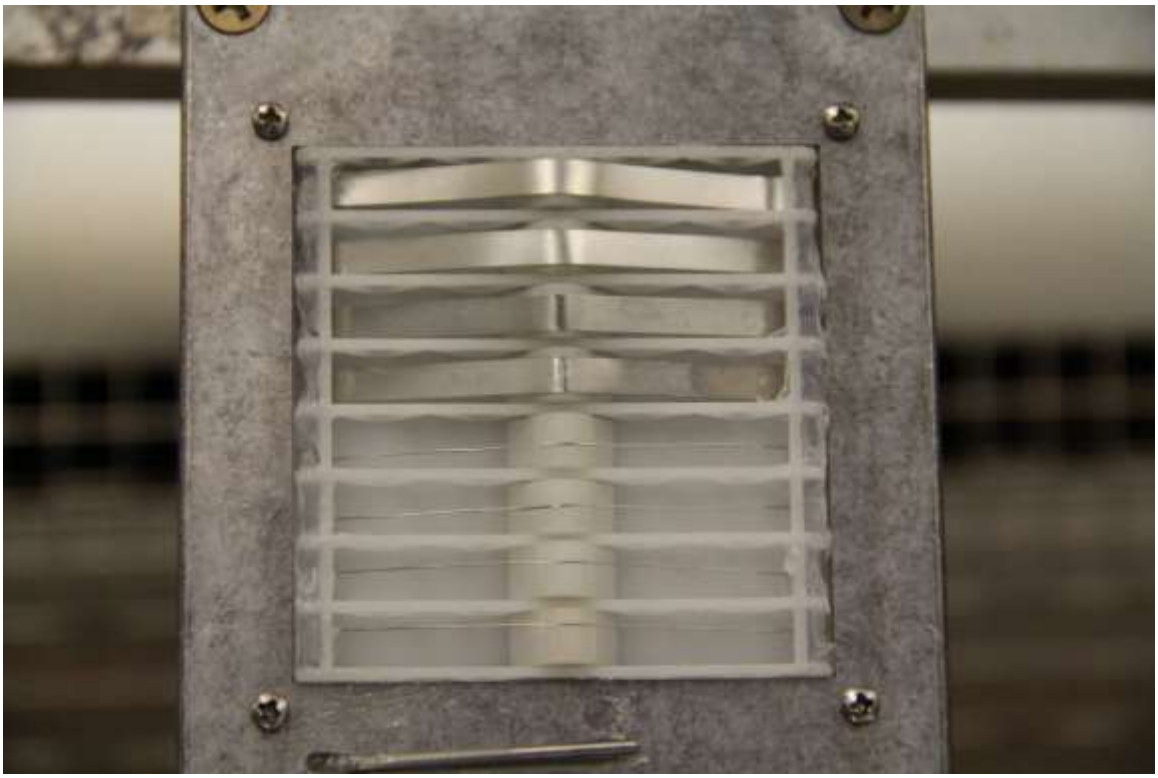

Figure 6.15 Corrosion Sensor Configuration. This image shows the corrosion sensor configuration for the third test.

The sensor unit was sprayed with synthetic sea water every few days and the humidity in the chamber was set to 100% RH and 30°C. This was done keep the sensors wetter than the previous test to encourage corrosion.

Test Results and Analysis

The test lasted 186.5 days, and the four wire sensor elements broke, however the strip sensors did not. The environmental chamber worked as expected over this time, and the humidity and temperature sensors all survived. Figure 6.16 shows a graph of the environmental conditions in the chamber during the test.

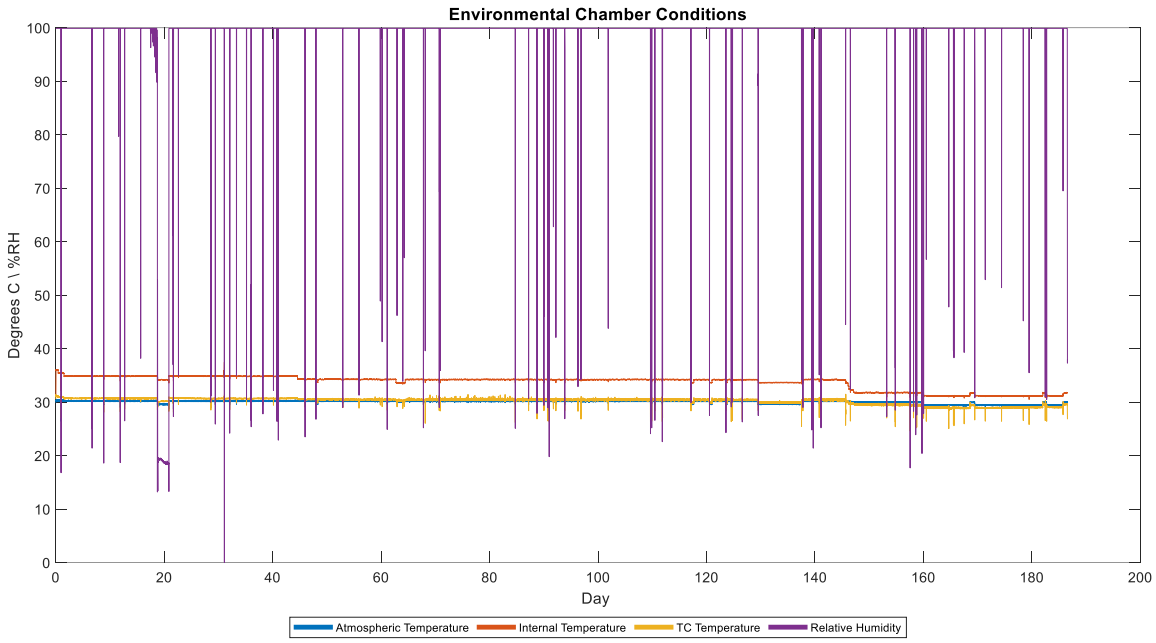

Figure 6.16 Environmental Conditions Within the Chamber. At day 0 the temperature was set to 30˚C and humidity was set to 100%RH. Humidity levels temporarily drop when the chamber is opened to be sprayed or maintained.

The drops in humidity are due to the chamber being opened for inspection or spraying. The overall temperature in the chamber remained constant throughout the test and did not change remarkably even when the chamber door was opened. The humidity data is directly related to the time of wetness, however even though the humidity remained close to 100%RH for the duration of the test the TOW sensor was not constantly saturated. Figure 6.17 shows the TOW sensor data from this test.

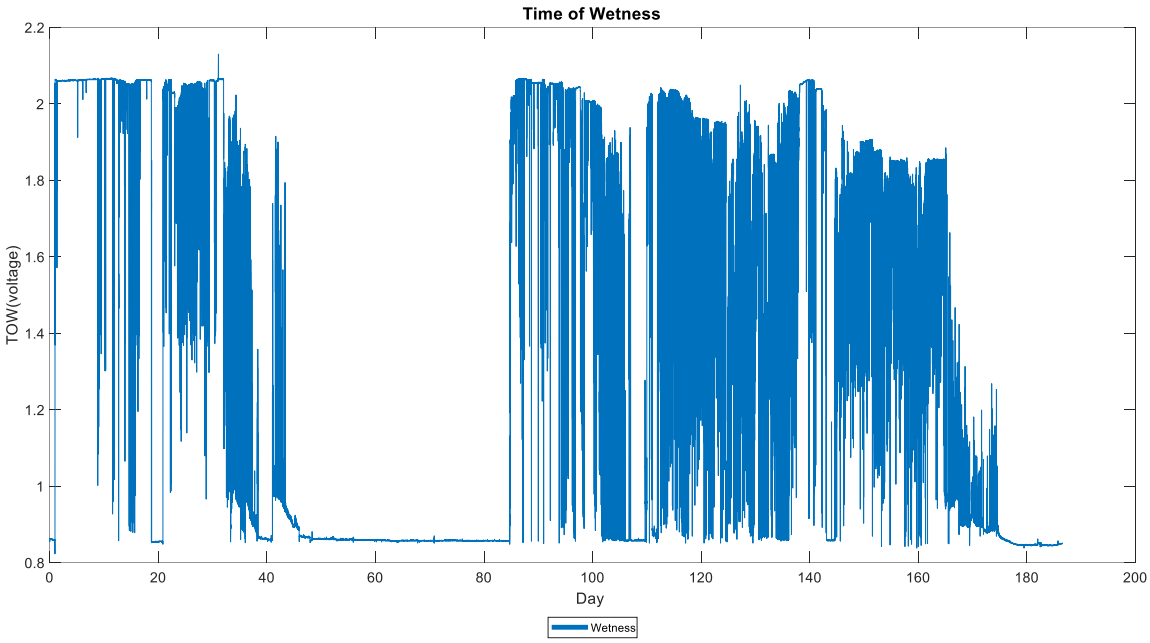

Figure 6.17 TOW Sensor Output. The graph shows the voltage read from the TOW sensor over the 186.5 day test.

Initially the TOW sensor is saturated, but over time water appears to condense less and less often on the sensor. There is a period of over a month where no condensation was detected at all. There are many factors that contribute to condensation and dew point, and there is not enough data to explain this dry period. It would appear from the data that the factors that affect condensation result in a marginally stable system that occasionally allows and disallows condensation to form.

The corrosion sensor functioned correctly during this test and the first detection of corrosive material occurred on day 126. The primary difference in test setup for this test was that the sensors were not pretreated with a supersaturated salt and isopropyl alcohol solution. This resulted in nearly four months passing before the corrosion sensor was corroded enough by the sea water to connect the galvanically coupled materials in the sensor. Figure 6.18 shows the data form the corrosion sensor.

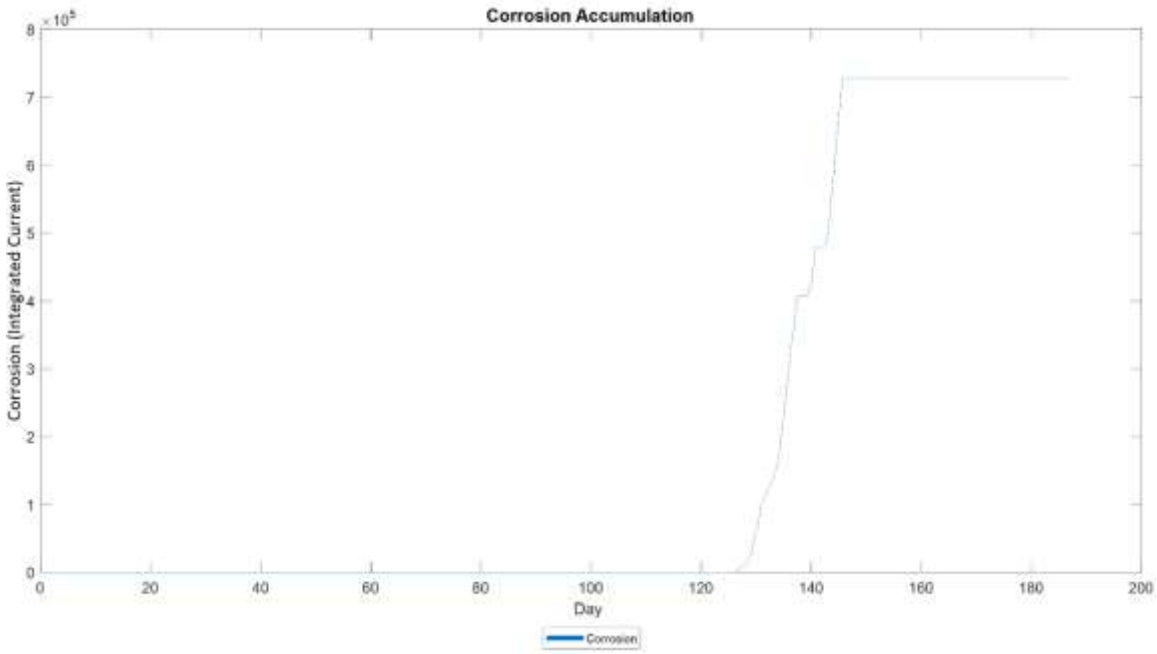

Figure 6.18 Corrosion Sensor Output. The graph shows the integrated current from the current sensor over the 186.5 day test.

The sensor corroded to the point of failure upon which the current produced dropped to 0. Using Equation 5.5 the detection of corrosive material occurred on day 126 and from this point the environmental readings from the TOW and humidity sensors would be applied to Equations 5.6 and 5.7.

The remaining probability weight is based on the individual corrosion sensors. The wire corrosion sensors all broke within the same day. However, the rate of change in resistance indicated by the sensors was not very long. Figure 6.19 shows the resistance data from day 125 to 150 which is the time in which the corrosion sensor showed activity before failing.

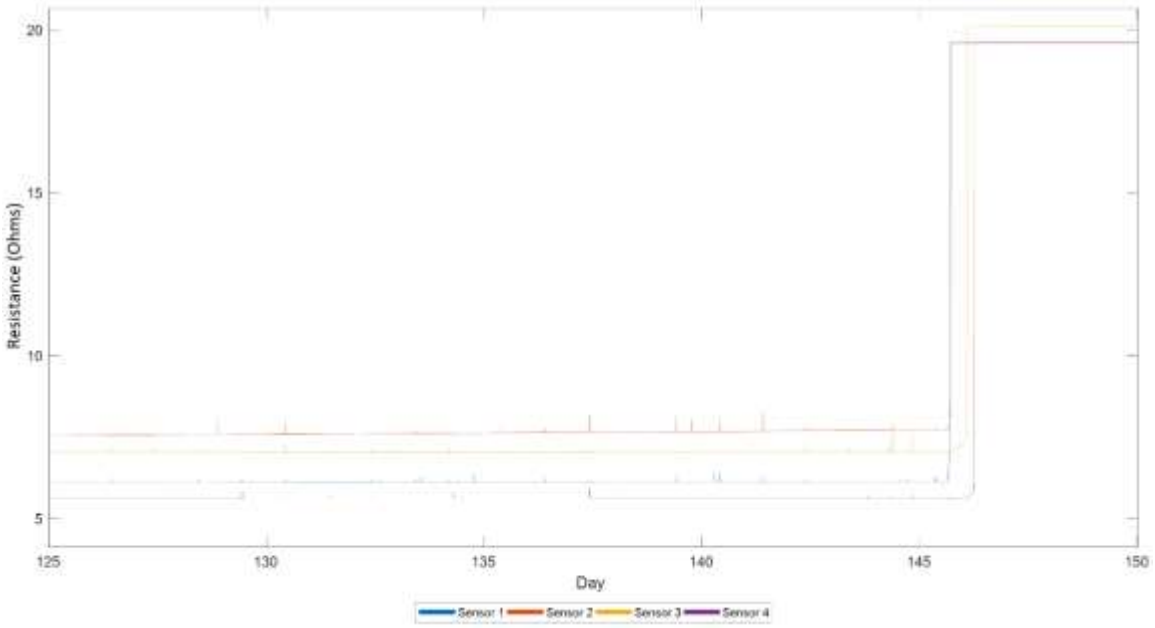

Figure 6.19 Wire Corrosion Sensor Data. The graph shows the resistance measurements from the wire Corrosion sensors after corrosion was detected and after the sensors broke.

In order to apply the PDF equations from Chapter 5 the data from the previous test must be used as a reference point. The humidity and TOW sensor readings from the point of corrosion from Test 2 must be used as a reference to compare the progression of corrosion. It took approximately 15 days from the point of corrosion in Test 2 for the wires to break. Integrating the Test 2 sensor readings over this 15 day time and comparing them to the values seen in Test 3 will give the μ and σ values for both the humidity and TOW PDFs. Using the corresponding corrosion resistance values from Test 2 will also allow for the resistance PDF to be generated. Figure 6.20 shows the data from wire Corrosion Sensor 1 near the breaking point and the corresponding PDF data generated using Equation 5.9 estimating over a 25 day period.

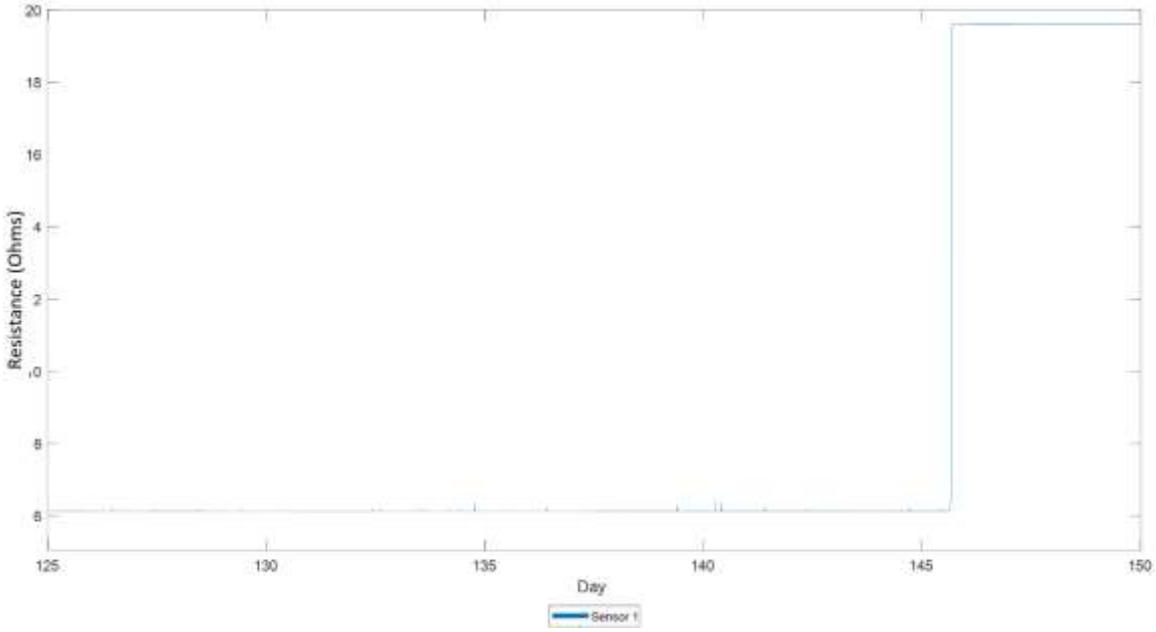
Resistance (Ohms)
Day
Sensor 1

(a)

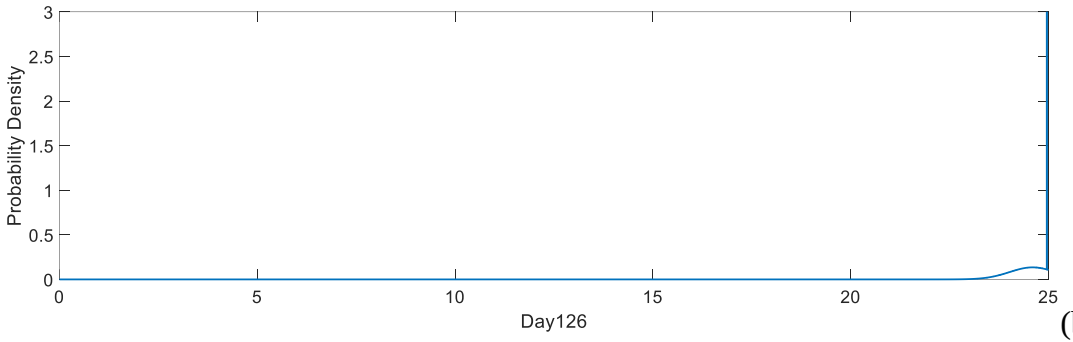
Probability Density
Day126

(b)

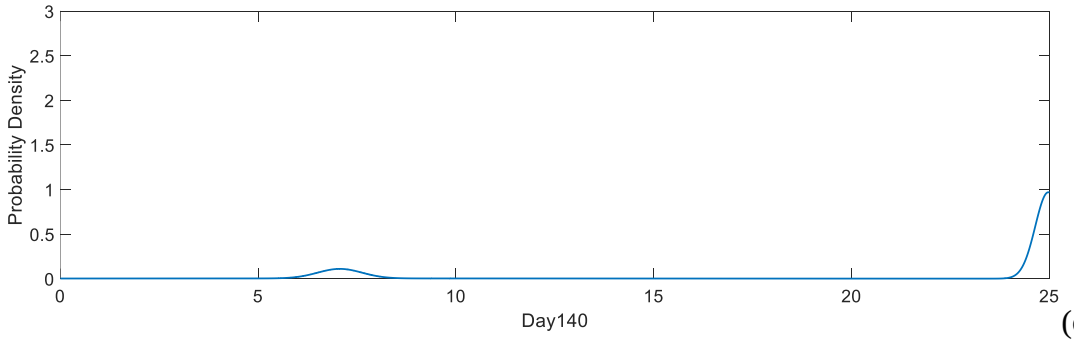
Probability Density
Day140

(c)

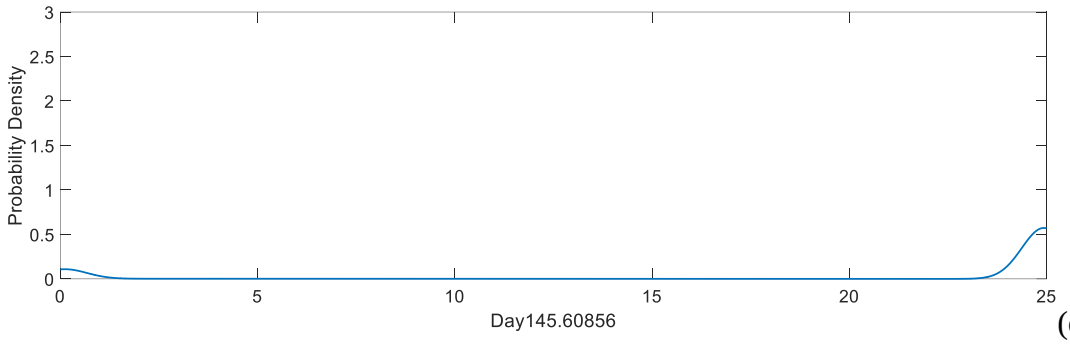
Probability Density
Day145.60856

(d)

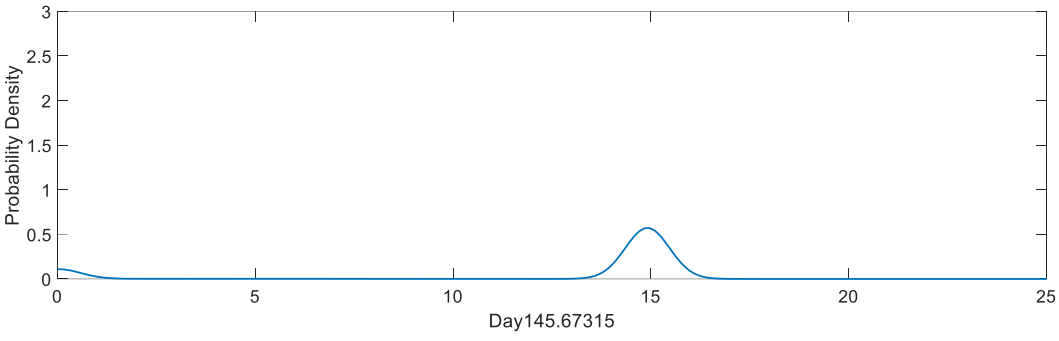
Probability Density
Day145.67315

(e)

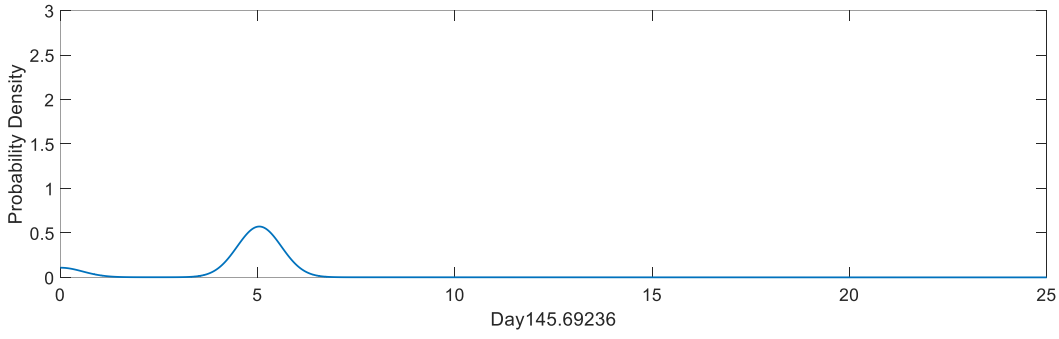
Probability Density
Day145.69236

(f)

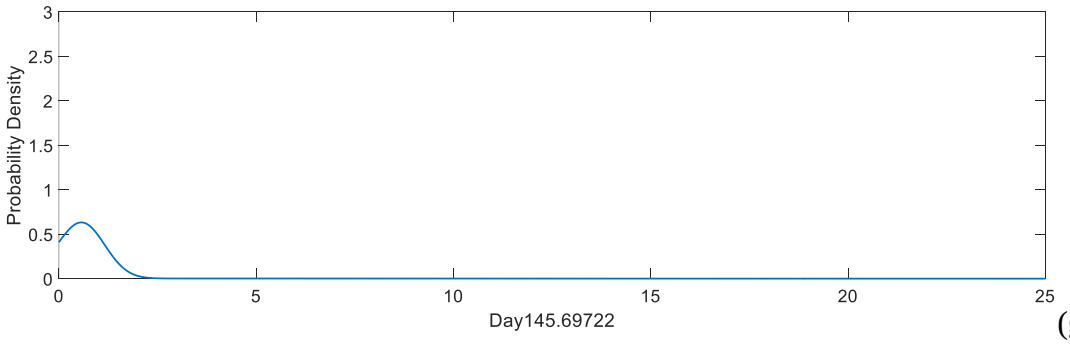
Probability Density
Day145.69722

(g)

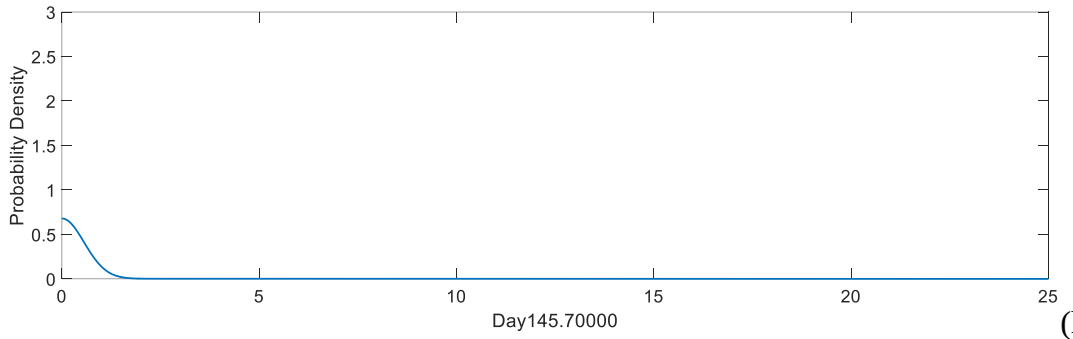

(h)

Figure 6.20 Wire Corrosion Sensor 1 PDF. Graph (a) shows 25 days of resistance data after the atmospheric corrosion sensor has detected chlorides for corrosion sensor 1. Graphs (b) through (h) show how the probability of sensor failure increases as the sensor nears the breaking point.

The PDFs above track the probability of sensor failure very closely. The initial bump seen in Figure 6.20(b) is the probability of failure related to the TOW and humidity data. The sensors in Test 2 failed in 15 days after the corrosion sensor detected chlorides while Test 3 sensors failed nearly 20 days after that point. Because of this, the probability of failure related to TOW and humidity tracks several days ahead of the resistance values.

The difference in time between Figure 6.20(d) and 6.20(h) is very small because Corrosion Sensor 1 broke very quickly. Figure 6.21 shows a zoomed in graph of Figure 6.20(a).

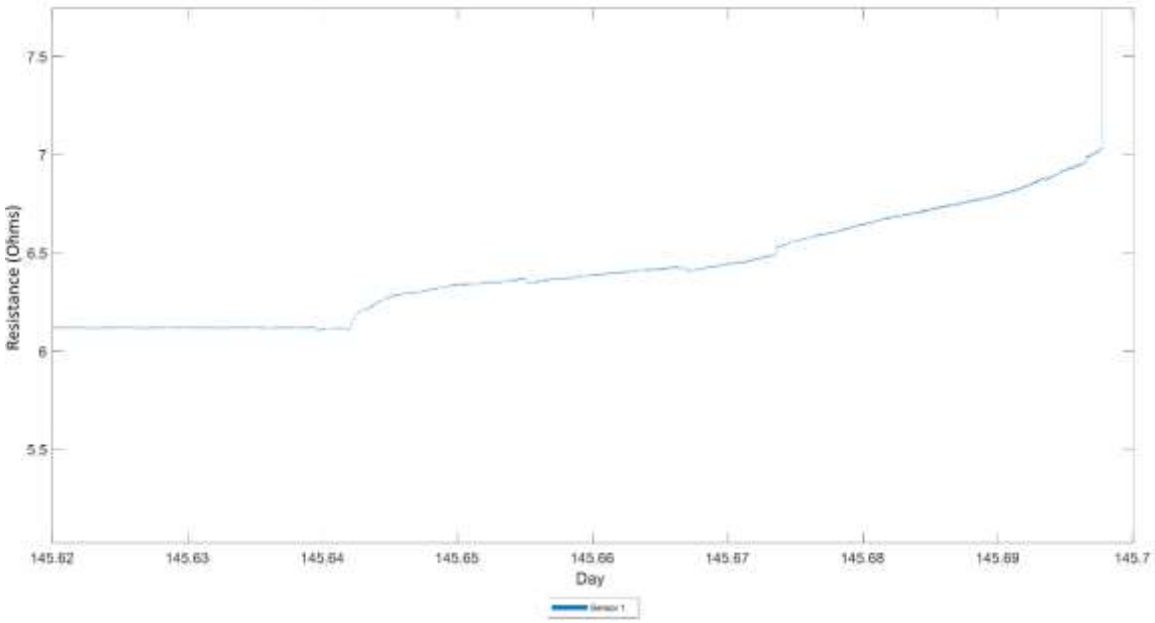

Figure 6.21 Wire Corrosion Sensor 1 Resistance Data Near Break. This graph shows the resistance data from wire Corrosion Sensor 1 near the break.

The resistance of the senor increased very quickly and did not give much warning before the crack. The PDF equation was able to forecast the break but not very far ahead of the break. Wire Corrosion Sensor 4 had the most gradual break over 4 hours and gave the most precise probability estimates for Test 3. The zoomed in resistance break data for Sensor 4 is in Figure 6.22.

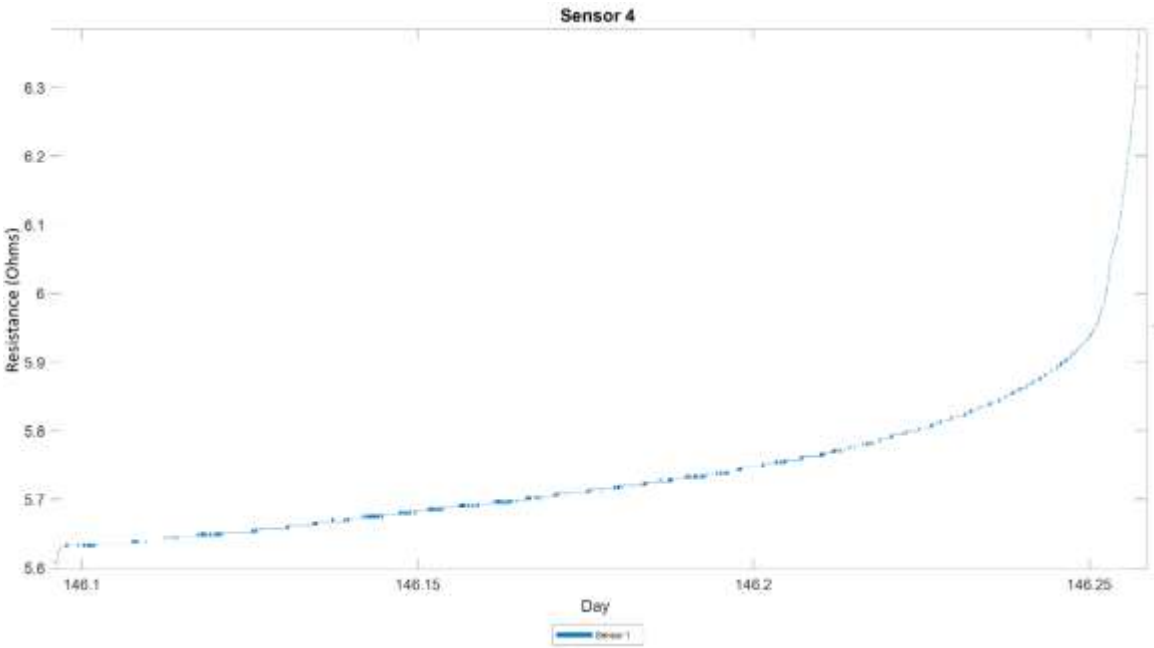

Figure 6.22 Wire Corrosion Sensor 4 Resistance Data Near Break. This graph shows the resistance data from wire Corrosion Sensor 4 near the break.

The data in Figure 6.22 is shaped very much like the expected Corrosion resistance curve in Figure 5.9 until the break occurs. The cross-sectional area of the wire decreased at the breaking point until the wire snapped under the tension of the spring. Unfortunately there are no SEM images of this wire to confirm the existence of cracks or the presence of necking as the wire breaks, but the shape of the resistance curve points to this happening. The exponential curve of the graph would indicate the formation of a crack and the change in slope at the very end right before the break would indicate the sensor is well into the plastic deformation phase and possibly necking.

The PDF estimations for this sensor are shown in Figure 6.23 and are scaled to show a 1 day period.

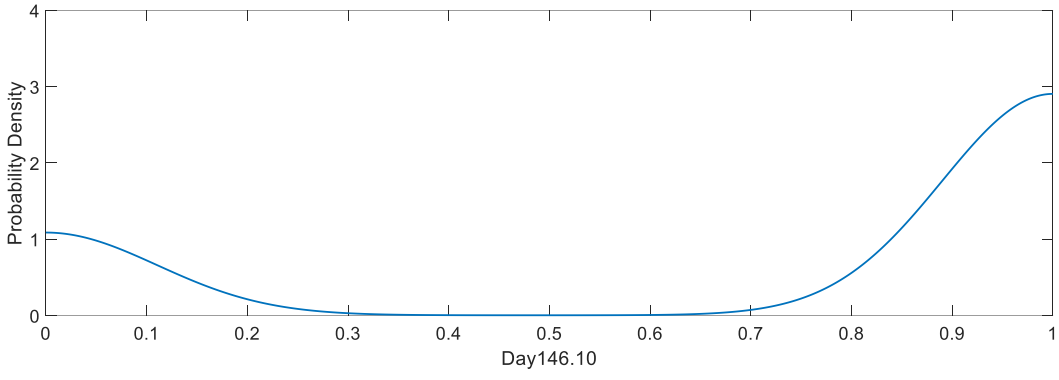
Probability Density
Day146.10

(a)

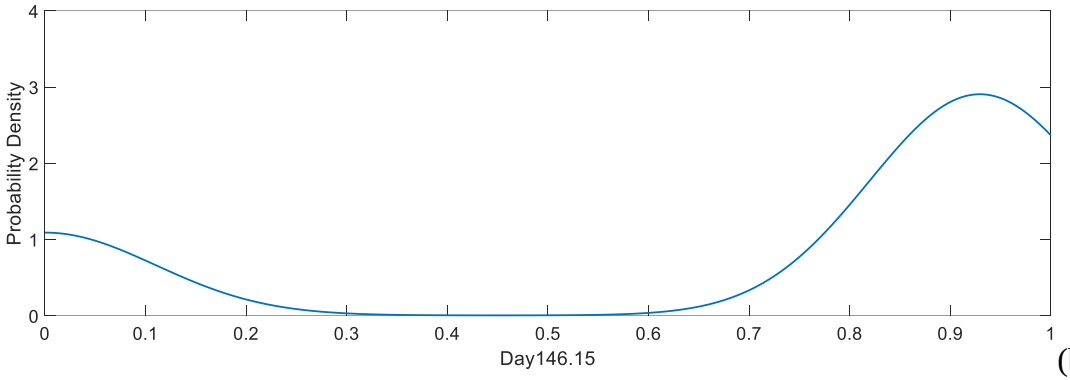
Probability Density
Day146.15

(b)

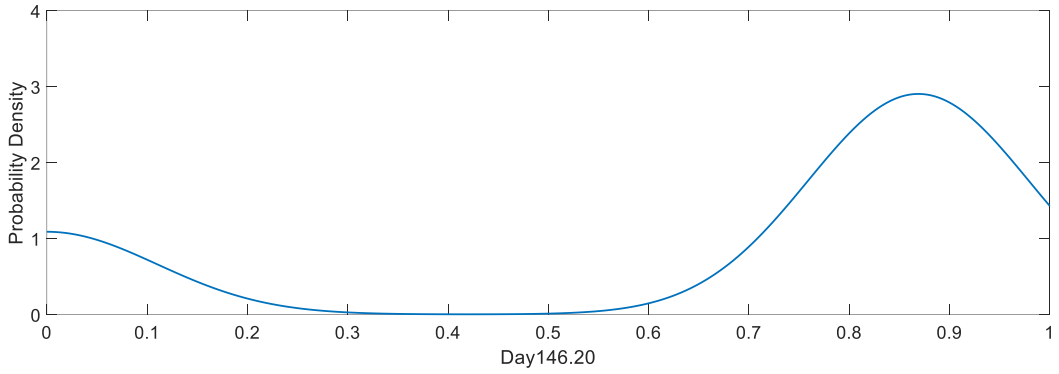
Probability Density
Day146.20

(c)

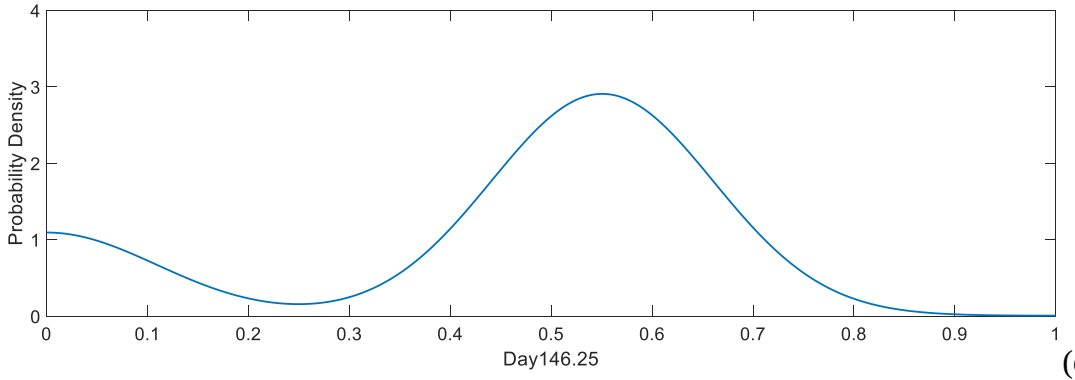
Probability Density
Day146.25

(d)

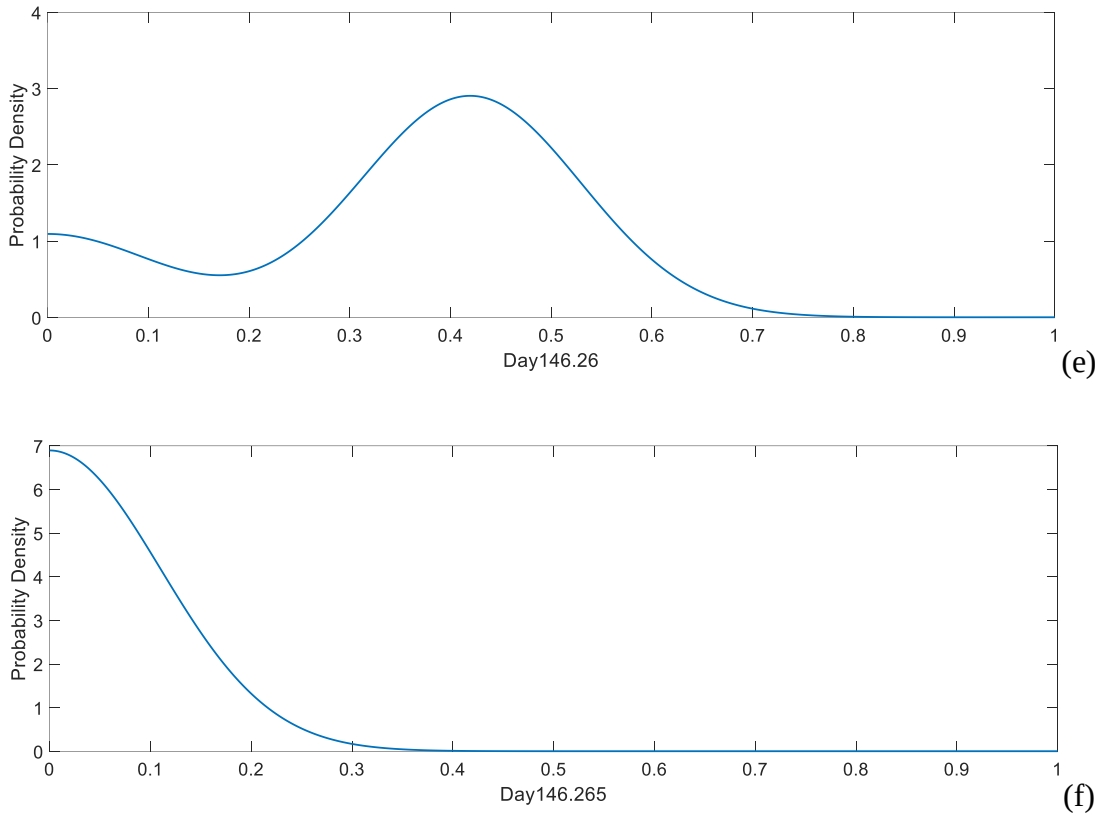

Figure 6.23 Wire Corrosion Sensor 4 PDF. Graphs (a) through (f) show how the probability of sensor failure increases as the sensor nears the breaking point.

The graphs in Figure 6.23 show the progression of the PDF estimation during the four hours prior to the breaking point. As the rate of change in resistance increases, the mean of the PDF related to resistance also moves closer to zero. By the time the resistance has reach the point of Figure 6.23(d), the estimation indicates that there is a 99% chance the wire will break in the next day. This is also the point where it is assumed that the plastic deformation has begun, and the wire fails less than an hour later.

The variance of the PDFs generated in this test are based on the data collected in Test 2, but the sample size is very small. With an increased number of samples the model could be dialed in to provide a more accurate estimation. With this increased amount of data it would also be possible to move to a Poisson distribution rather than a normal distribution for each individual weighted PDF

CHAPTER SEVEN: FUTURE WORK

Robotic Deployment

There has been much discussion on a method to deploy this sensor system onto canisters that are already serving as spent nuclear waste containment. Attaching a sensor system by hand would require the steel canister to be removed from the concrete overpack which would place undue stress on the canister and danger to technicians performing the task. Attaching the sensors to the steel canister while it is inside the concrete overpack poses two major challenges. The first is a viable access area. The only way to reach the canister from the outside of the overpack it through the vents which are far too small to be of use to a human and limit the maneuverability of tools. The second challenge is the variety of canister designs in use. Finding a solution that would work on all canister types is difficult as the orientation of the canisters vary along with the location of the vents and the clearance between the steel canister and the concrete overpack.

The solution to these problems may be robotic deployment. There are multiple robots in development specifically designed to navigate the vents of the overpack and inspect the canister directly. One example is a four wheeled robot with magnetic wheels which is able to climb the walls of the vents by attaching to the carbon steel lining of the concrete casks. This would allow the robot to enter the cask at the bottom and climb to the top of the canisters while inspecting all the way. Another similar robot uses a vacuum

skirt fed by an external hose to attach to the walls. Both of these prototypes are pictured below in Figure 7.1 [45].

Figure 7.1. Prototype Robotic Delivery Systems with Simulated Sensing Devices: Vacuum Suction Prototype (Left) and Magnetic Prototype (Right).

Another prototype robotic delivery system is a snake robot created from multiple omnidirectional joints. This type of robot would be able to slither through vents and would contain a camera and inspection hardware within its head. Figure 7.2 [45] shows this type of robots moving through the vents of a horizontal canister while carrying a non-destructive evaluation (NDE) sensor unit.

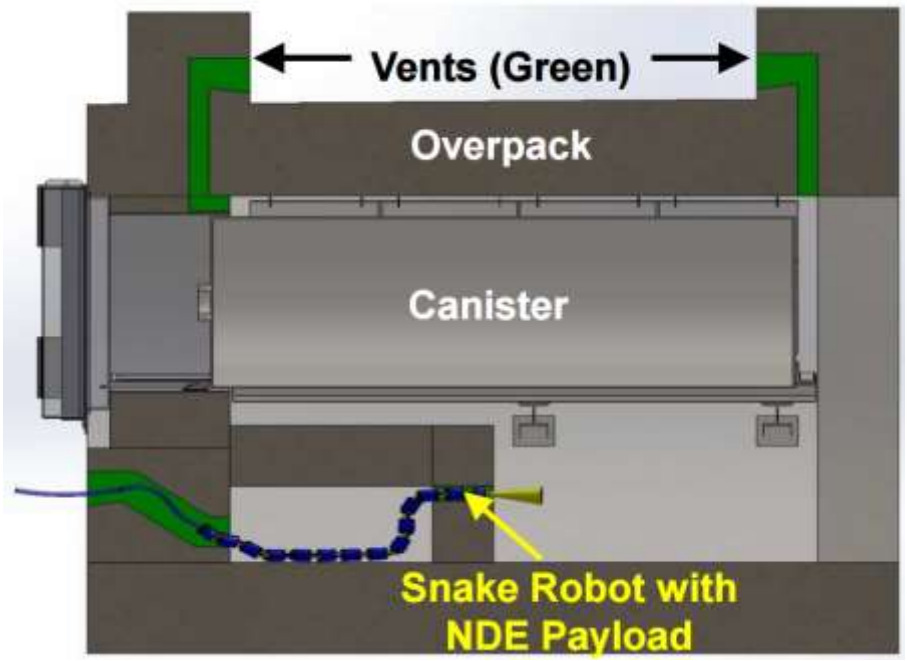

Figure 7.2. Prototype Robotic Snake Delivery System with and NDE payload.

Thermoelectric Generators

The energy requirements for a sensor module are very small and can be made even smaller with the addition of power management integrated circuits (PMICs) to sleep and wake the system when scheduled sensor readings occur. The potential for powering the sensor module using energy harvested from the environment is ever increasing as the efficiency of energy scavenging technology increases. The most abundant source of energy within the canister is thermal energy created by the spent fuel itself. A thermoelectric generator could be used to harvest this environmental energy and convert it to usable electrical energy. Thermoelectric devices use the Seebeck to effectively become heat engines with no moving parts but comparatively low efficiency.

A thermoelectric generator is made of two materials that are electrically conductive but not thermally conductive. An example of this would be silicon and germanium. A temperature differential between these two materials creates a potential

difference between electrodes attached to each material which can then be used to power a device. A famous example of these devices being used with nuclear material is the Curiosity Rover's radioisotope thermoelectric generator (RTG) which uses 4.8kg of plutonium-238 to generate heat for one side and the Martian atmosphere to keep the other side cool. This RTG is rated to provide the rover with 14 years of continuous power [46]. The sensor module in this dissertation uses a fraction of that power.

In the case of a SNF canister, the surface of steel container would be the hot side of the generator and the sensor module enclosure itself would act as the heatsink for the cool side. The electrodes for the generator would return into the sensor module to power it. Depending on the amount of voltage and current generated, the energy would be passed through a switching regulator and stored ether in a super capacitor or battery for later use. The module would then "wake up" at a scheduled interval, take readings, transmit the results, then go back to sleep. It would be possible to add a wireless transmitter to the module then send readings back to a base station. This would make the sensor module self-powered and wireless at the same time, thus simplifying its deployment onto existing canisters.

To prove this was a valid avenue of research a thermoelectric generator (GMZ TG8) designed to be used within a canister environment was connected the testing platform shown in figure 7.3.

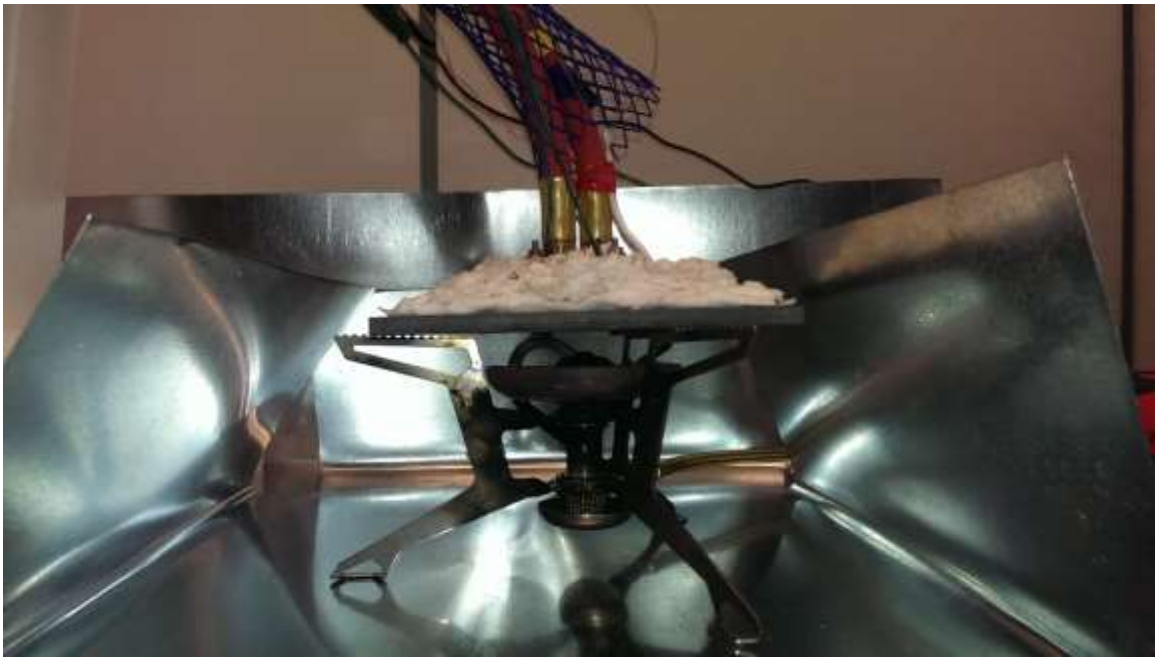

Figure 7.3. Thermoelectric generator placed with a testing apparatus.

The bottom side of the generator is exposed to a gas heat source and the top is liquid cooled using tap water flowing through a water block. This energy was passed through a switching power regulator (an NCP1402 step up regulator in this case) to produce a constant 5V. This 5V was then directly connected to the input power rail of a motherboard which was able to boot and perform sensor readings and send data over a serial cable. A minimum temperature differential of 160˚C was required to produce enough energy to power this system.

Canister Redesign

There are many difficulties in deploying the sensor unit due to the average design of SNF systems. Limited maneuvering room between the steel and the overpack combined with only the vents as a means of access complicates the installation of this sensor unit. The need for monitoring the stainless steel welds increases as the average age of in use SNF canister increases. A proactive solution would involve redesigning all

future canisters with ports that allow the integration of sensor monitoring packages. These packages may be standardized by either the NRC or the canister manufacture, but all weld points need the ability to be easily monitored and the sensor units must remain accessible. This may involve modification of the stainless steel canister or the addition of access ports within the concrete overpack. These smart SNF storage canisters should then be able to self-diagnose problems and report on their overall health.

Time-Domain Reflectometer

Many of the issues in measuring the impedance of the strip geometries might be solved by using a time-domain reflectometer (TDR) in conjunction with the resistance measurements. TDR measurements are normally used to verify impedance controlled PCB traces for manufacturing defects. Pits and cracks forming in the strip do not create a large change in resistance, but would cause a change in the reflection of an incident signal coming from a TDR. The usefulness of a TDR could be verified by measuring the impedance of a strip while corroding with an accelerated tester like the one in Figure 5.5. If the results are promising, then research into designing a small scale TDR would be worthwhile.

CHAPTER EIGHT: CONCLUSIONS

This dissertation detailed an iterative design process that resulted in a low cost sensor system capable of surviving harsh environments and detecting corrosion. The design of the corrosion sensor is of novel origin as is the combination of sensors, electronic hardware, and prognostic algorithms aimed that this target application. The overarching goal of creating a sensor system using sacrificial stainless steel electrodes to detect corrosion was accomplished, however future work into increasing the effectiveness of non-wire sensor geometries is still needed. The results have shown that wire based geometries can and will break due to corrosion, but prognosticly detecting when a failure will occur is limited to a few hours before the break. Larger sensor geometries are needed to effectively gauge the health of a canister as they deteriorate at a slower rate.

The sensor set used in this system has shown that it is capable of detecting the various environmental conditions that cause corrosion. This system as a whole has demonstrated its ability to collect this data and the framework for prognosticly detecting sensor failure by implementing sensor fusion techniques has been shown to be successful. Building up and improving this design to create a full fledged event detection framework for an entire spent nuclear waste facility needs to be the end goal for this research. This is becoming more and more important as an increasing amount of spent nuclear waste is stored in distributed facilities across the country. Such a system will move us towards safer spent nuclear waste storage.

REFERENCES

1. Commission, N.R., *10 CFR Part 72. Licensing Requirements for the Independent Storage of Spent Nuclear Fuel and High-Level Radioactive Waste, U.S. Nuclear Regulatory Commission, Washington DC, 1998.*, 1998.
2. McConnell, P., Hanson, B., Lee, M., and Sorenson, K., *EXTENDED DRY STORAGE OF USED NUCLEAR FUEL: TECHNICAL ISSUES: A USA PERSPECTIVE.* Nuclear Engineering and Technology, 2011. **43**(5): p. 405-412.
3. Commission, N.R., *Cladding Considerations for the Transportation and Storage of Spent Fuel. SFST-ISG-11 (2003a), Rev. 3, U.S. Nuclear Regulatory Commission, Washington DC. 2003.*, 2003.
4. Kammenzind, B.F., Franklin, DG., Peters, HR., Duffin, WJ. *Hydrogen Pickup and Redistribution in Alpha-Annealed Zircaloy-4*. in *In Zirconium in the Nuclear Industry: Eleventh International Symposium, ASTM STP 1295.* 1996. Philadelphia, Pennsylvania: American Society for Testing and Materials.
5. Kearns, J.J., *Terminal solubility and partitioning of hydrogen in the alpha phase of zirconium, Zircaloy-2 and Zircaloy-4.* Journal of Nuclear Materials, 1967. **22**(3): p. 292-303.
6. B. Gordon and M. Taylor, *Climatic Corrosion Considerations for Independent Spent Fuel Storage Installations in Marine Environments*, Report No. 1013524 (Electric Power Research Institute, San Jose, 2006).
7. Hanson, B.D., et al., *Used Fuel Disposition Campaign - Gap Analysis to Support Extended Storage of Used Nuclear Fuel, Rev. 0*, 2012.
8. Meyer, R.M., B. Hanson, and K. Sorenson, *Detecting and Monitoring of Atmospheric SCC in Dry Cask Storage Canisters for Used Nuclear Fuel*, in *CORROSION 2013*2013, NACE International: Orlando, Florida.

9. Rigby, Douglas. "Evaluation of the Technical Basis for Extended Dry Storage and Transportation of Used Nuclear Fuel." NWTRB. NWTRB, 1 Dec. 2010. Web. 8 Apr. 2015. <http://www.nwtrb.gov/reports/eds_rpt.pdf>.

10. " Frequently Asked Questions." *Eureka County, Nevada -- Yucca Mountain.org, Frequently Asked Questions, FAQ's*, Eureka County, Nevada Nuclear Waste Office , 15 May 2019, www.yuccamountain.org/faq.htm#status.

11. Manley, S.L., C. Lowe, *Canopy-Forming Kelps as California's Coastal Dosimeter: from Damaged Japanese Reactor Measured in Macrocystis pyrifera.* Evinronmental Science & Technology, 2013. 46(7): p. 3731–3736

12. "Backgrounder on High Burnup Spent Nuclear Fuel." *United States Nuclear Regulatory Commission - Protecting People and the Environment*, United State Nuclear Regulatory Commission, 1 Oct. 2018, www.nrc.gov/reading-rm/doc-collections/fact-sheets/bg-high-burnup-spent-fuel.html.

13. Engeman, J.K., C.L. Girardot, D.G. Harlow, C.L. Rosenkrance, Tank 241-AY-102 Leak Assessment Report. U.S. Department of Energy , 2012.

14. "Ceion and Electrical Resistance (ER) Monitoring." *Ceion and Electrical Resistance (ER) Monitoring*, CORR Science, www.corrscience.com/products/corrosion/intro-to-corrosion/ceion-and-electrical-resistance-er-monitoring/.

15. Mitchell, Harvey B. *Multi-Sensor Data Fusion: an Introduction*. Springer, 2010.

16. Lumsden, J.B., and M.W. Kendig. "Detecting Initiation of Stress Corrosion Cracking."Detecting Initiation of Stress Corrosion Cracking. EPRI, 1 July 1990. Web. 29 Mar. 2015. <http://www.epri.com/abstracts/Pages/ProductAbstract.aspx?ProductId=NP-6916>.

17. Waldrop, K. "Calvert Cliffs Stainless Steel Dry Storage Canister Inspection." Calvert Cliffs Stainless Steel Dry Storage Canister Inspection. EPRI, 11 Apr. 2014. Web. 29 Mar. 2015. <http://www.epri.com/abstracts/Pages/ProductAbstract.aspx?ProductId=000000000001025209>.

18. Winston, Phil. Canister Monitor Feasibility Report. INEEL, 2001. Print.

19. Vashishta, P. "Hierarchical Petascale Simulation Framework for Stress Corrosion Cracking." Journal of Physics 78.1. Print.

20. "The Novel New Ultra-Sensitive Corrosion Sensor." *Corrosion Monitoring Solution The Novel New Ultra-Sensitive Corrosion Sensor from IButtonLink and Jointly Developed with IBM Research*, Ibuttonlink, www.ibuttonlink.com/pages/corrosion-sensor.

21. S. Loo, M. Owen, J. Kiepert, and A. Planting. "Modular, Portable, Reconfigurable, and Wireless Sensing System for the Aircraft Cabin." Journal of ASTM International. 5.4(2008): 1-9. Web. 29 Feb 2020.<https://doi.org/10.1520/JAI101638>

22. Gonzalez-Guerrero, M., et al. The effect of proton and gamma radiation on different types of temperature sensors. in Radiation and Its Effects on Components and Systems (RADECS), 2009 European Conference on. 2009.

23. "Precision Thermocouple Amplifiers with Cold Junction Compensation." *Precision Thermocouple Amplifiers with Cold Junction Compensation*, Analog Devices, www.analog.com/media/en/technical-documentation/data-sheets/ad8494_8495_8496_8497.pdf.

24. Liu, Thomas. "Digital Relative Humidity & Temperature Sensor RHT03." *Digital Relative Humidity & Temperature Sensor RHT03*, Max Detect, cdn.sparkfun.com/datasheets/Sensors/Weather/RHT03.pdf.

25. Leckie, R. and H. Lenos, *CZT Detectors: Converging assembly technologies open new application opportunities.* Chip Scale Review, 2009(Oct/Nov).

26. Mitkova, M., et al., *Gamma ray induced structural effects in bare and Ag doped Ge-S thin films for sensor application.* 2013.

27. Centronic. *Geiger Muller Tube Theory*. [cited 2013 July 2, 2013]; Available from: http://www.centronic.co.uk/downloads/Geiger_Tube_theory.pdf.

28. Glasstone, S., *Sourcebook on Atomic Energy*. Third ed. 1967, Malabar, FL: Robert E, Krieger Publishing, Inc. 883.

29. Centronic. *Geiger Muller Tube Theory*. [cited 2013 July 2, 2013]; Available from: http://www.centronic.co.uk/downloads/Geiger_Tube_theory.pdf.

30. "LND 7436." LND INC. LND. Web. 7 Apr. 2015. <http://www.lndinc.com/products/383/>.

31. Schindelholz, E., et al., Comparability and accuracy of time of wetness sensing methods relevant for atmospheric corrosion. Corrosion Science, 2013. 67(0): p. 233-241.

32. Schindelholz, E. and R.G. Kelly, Wetting phenomena and time of wetness in atmospheric corrosion: a review. Corrosion Reviews, 2012. 30(5-6): p. 135-170.

33. Sridhar, N., et al., *Corrosion monitoring techniques for thermally driven wet and dry conditions*, in *Corrosion 2000*2000.

34. Jaeger, M.D., B.R. Pilvelait, and P.J. Magari, *Multilayer galvanic cell for next generation corrosion sensors*, in *Corrosion 2000*2000.

35. Broussard, John, and Shannon Chu. "Susceptibility Assessment Criteria for Chloride-Induced Stress Corrosion Cracking (CISCC) of Welded Stainless Steel Canisters for Dry Cask Storage Systems." *Enclosure 3: Presentation Handouts [Memorandum to A. Hsia Re: Summary of April 21, 2015, Public Meeting With The Nuclear Energy Institute On The Chloride Induced Stress Corrosion Cracking Regulatory Issues Resolution Protocol]*., EPRI, 21 Apr. 2015, www.nrc.gov/docs/ML1514/ML15146A115.pdf.

36. G. S. Ohm (1827). Die galvanische Kette, mathematisch bearbeitet

37. Casas, J., Peñacoba, G. F., & Ruiz, M. R. (2008). The Radiation Tolerant Electronics for the LHC Cryogenic Controls: Basic Design and First Operational Experience. *Topical Workshop on Electronics for Particle Physics*,195-199. doi:10.5170/CERN-2008-008.195

38. T. Saegusa, K. Shirai, and H. Takeda, in *Issues and Countermeasures for Long-Term Storage of Spent Fuel by Dry Cask*, Proceedings of the Regulatory Information Conference, Maryland, 2012.

39. C. Bryan and D. Enos, "Interim storage environment: considerations for corrosion testing of SNF dry storage containers," Sandia National Laboratories, 748-754 (2013).

40. Lee J, Asim K, Pan J. Failure Mechanism of Laser Welds in Lap-Shear Specimens of a High Strength Low Alloy Steel. ASME. J. Pressure Vessel Technol. 2012;134(6):061402-061402-5. doi:10.1115/1.4006560.

41. Cárcel-Carrasco, Francisco-Javier, et al. "Pitting Corrosion in AISI 304 Rolled Stainless Steel Welding at Different Deformation Levels." *Applied Sciences*, vol. 9, no. 16, Sept. 2019, p. 3265., doi:10.3390/app9163265.

42. "Trunnion Rod Failure Analysis." Trunnion Rod Failure Analysis - Mobile, Alabama, Metallurgical Consulting, www.metalconsult.com/trunnion-rod-failure-analysis.html.

43. Voort, George Vander. "Measurement of Grain Size in Twinned FCC Alloys." Vacaero, Vac Aero International Inc, 11 Aug. 2016, vacaero.com/information-resources/metallography-with-george-vander-voort/1263-measurement-of-grain-size-in-twinned-fcc-alloys.html.

44. De Moivre, Abraham. *The Doctrine of Chances*. 1756.

45. Renshaw, Jeremy. "Inspection and Delivery Systems for Dry Canister Storage System Inspection." IEEE RoboResearch 2018, IEEE, 6 Mar. 2015, sites.ieee.org/ncc-roboresearch/files/2015/03/Renshaw_Inspection-and-Delivery-Systems-for-Dry-Canister-Storage-Systems.pdf.

46. Bechtel, Ryan. "Multi-Mission Radioisotope Thermoelectric Generator (MMRTG)." NASA Facts, National Aeronautics and Space Administration, Oct. 2013, mars.nasa.gov/mars2020/files/mep/MMRTG_FactSheet_update_10-2-13.pdf.

APPENDIX A

Sensor Module Assembly Instructions

This appendix gives instructions for the assembly of the Boise State Barnacle V3 Sensor Module.

Step 1. PCB Assembly

There are six PCBs to assemble for each unit. The motherboard, corrosion sensor, TOW sensor, atmospheric corrosion sensor, Ethernet adapter, and programmer. These are pictured below. Eagle schematics will contain exact part numbers and component values.

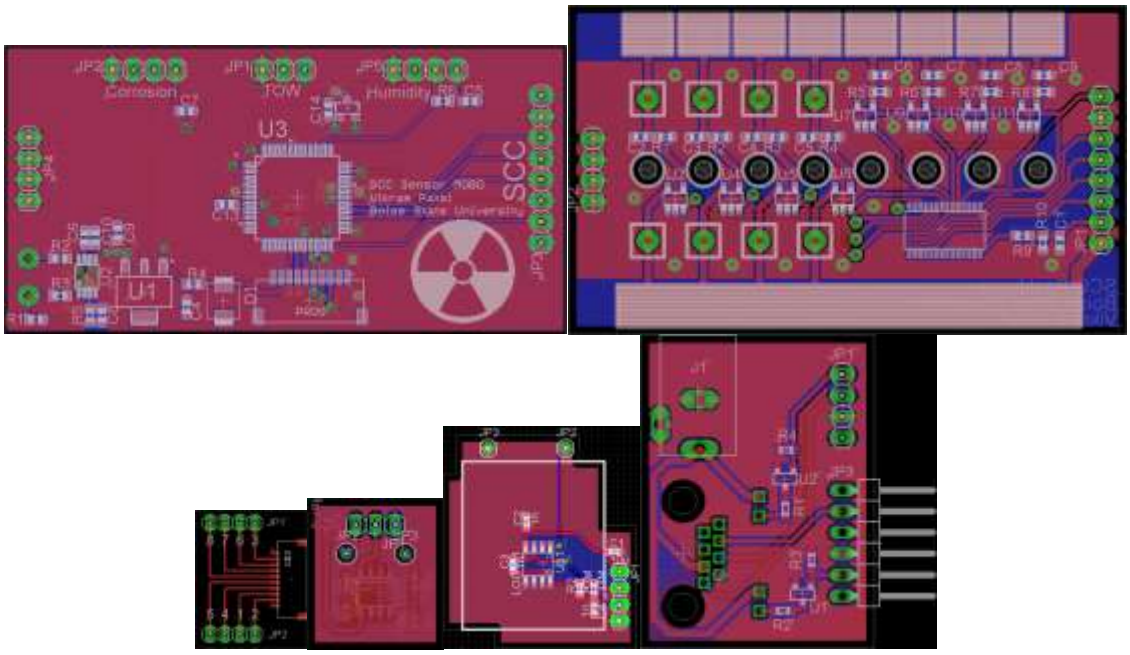

Figure A1. Six PCBs. These are the six PCBs that are needed to construct a single sensor module.

Step 2. Select Sensor Gain

The corrosion sensors use fixed gain current sensors to operate. The selection of which gain to use is dependent on the geometry of the sensor electrode. Smaller cross sections require less gain as the resistance of these electrodes are higher. Larger cross sections have a lower resistance and require a larger gain. Corrosion sensor channels 1-4 are designed for wires and will have smaller gains while channels 5-8 are designed for

strips which will have higher gain. Each current sensor has a corresponding resistor which must also be selected in order to limit the total current flowing through the sensor element.

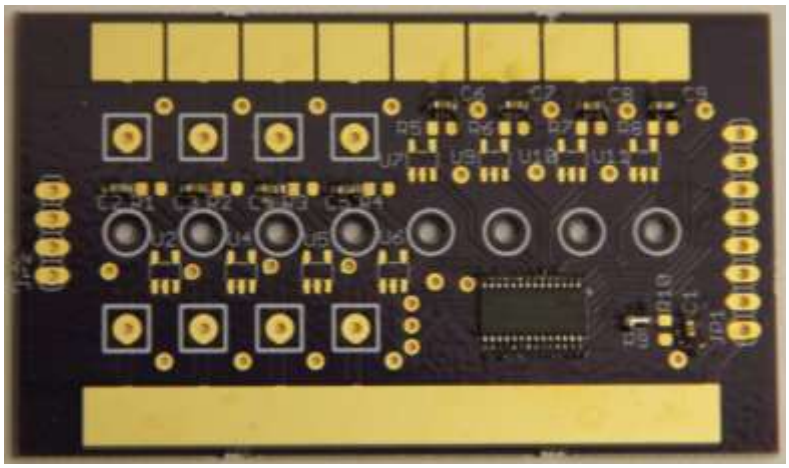

Step 3. Wiring

The TOW sensor, corrosion sensor, humidity sensor, and Ethernet adapter PCBs all require wiring to carry signals to and from the motherboard. The TOW sensor and corrosion sensor require ribbon cable to be soldered to the connection header and terminated in a right angled header. The humidity sensor leads need to be bent 90 degrees as close to the sensor case as possible and crimp connecters need to be used to solder the wires. The Ethernet adapter has eight connections that need to be soldered with short 22 gauge wire. The connections match the numbering on the side of the jack and the silk on the board. Attach a FFC to the motherboard and the Ethernet adapter.

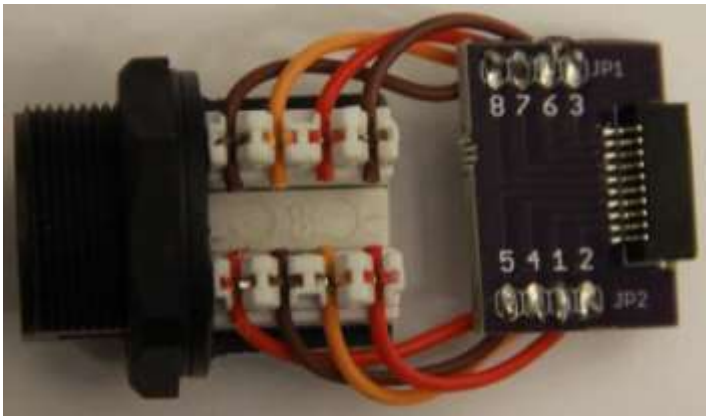

Step 4. Program and test all sensors

Attach all sensors to their respective headers. Connect the Ethernet adapter and programming board with an Ethernet cable. Attach the PICKIT 2 programmer and serial cable to the programming board. Set external power supply to 5V and 100mA and attach to the barrel jack on the programming board. Monitor current consumption for shorts and open circuit conditions. If current draw is normal, initialize serial terminal to 9600 Baud, 8-bits, no parity, and no flow control. Program the board and observe the terminal output. Correlate each sensor's reading with laboratory standards and confirm proper operation.

Step 5. PCB Cleaning

Once the system is verified all remaining flux must be removed from the PCBs. Use the aerosol PCB cleaner to remove the flux. The corrosion sensor pads should be scrubbed clean using a q-tip.

Step 6. Conformal Coating

Each PCB need to be environmentally sealed from liquids and contaminants. Automotive grade conformal coating must be applied to each board to prevent damage. Before conformal coating each female header must be sealed using silicon caulking. The capillary action of the conformal coating can damage the female headers by clogging them and preventing electrical contact. Once these are sealed a paint brush may be used to apply the conformal coating. A UV light may be used to overserve the coating in progress and assist in proper coverage. The corrosion sensor contact pads must remain uncovered for proper operation.

Step 7. Clean Corrosion Sensor SLA

The corrosion sensor mount may contain remnants of the 3D printing process which will interfere with operation. These can be cleaned out using tweezers and other small hand tools. The center span of mount may require filing in order properly slide the corrosion board in and out of the mount. This should be done by holding the file stationary and moving the mount across the file until the desired material is removed.

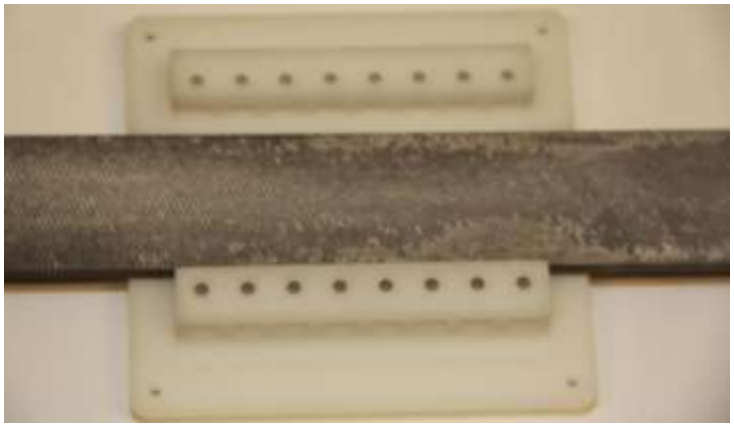

Step 8. Clean Humps

The SLA humps may also require cleaning before use. These can also cleaned using tweezers, but it may become necessary to use a small file to remove excess material.

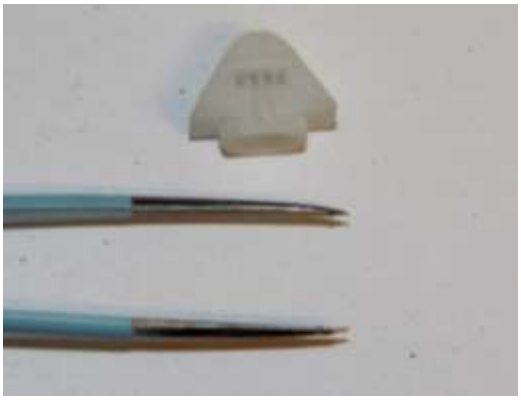

Step 9. Insert Nuts into Humps

Once cleaned the M2 nuts must be inserted into each hump and centered. The alignment of each nut must be maintained as it is inserted into each hump by used a vice to slowly squeeze it into place. Once inserted, the nut may be tapped into place by using a file to adjust its orientation.

Step 10. Insert Springs

Each spring should be inserted into the circular opening at the bottom of each hump.

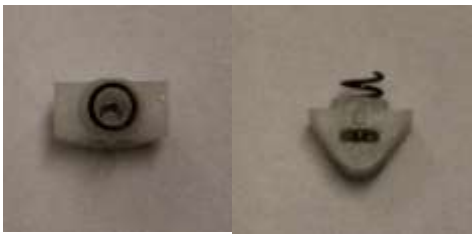

Step 11. Mounting Humps

Each hump must snap into each slot on the corrosion sensor mount. The hump should move freely and bounce back when depressed.

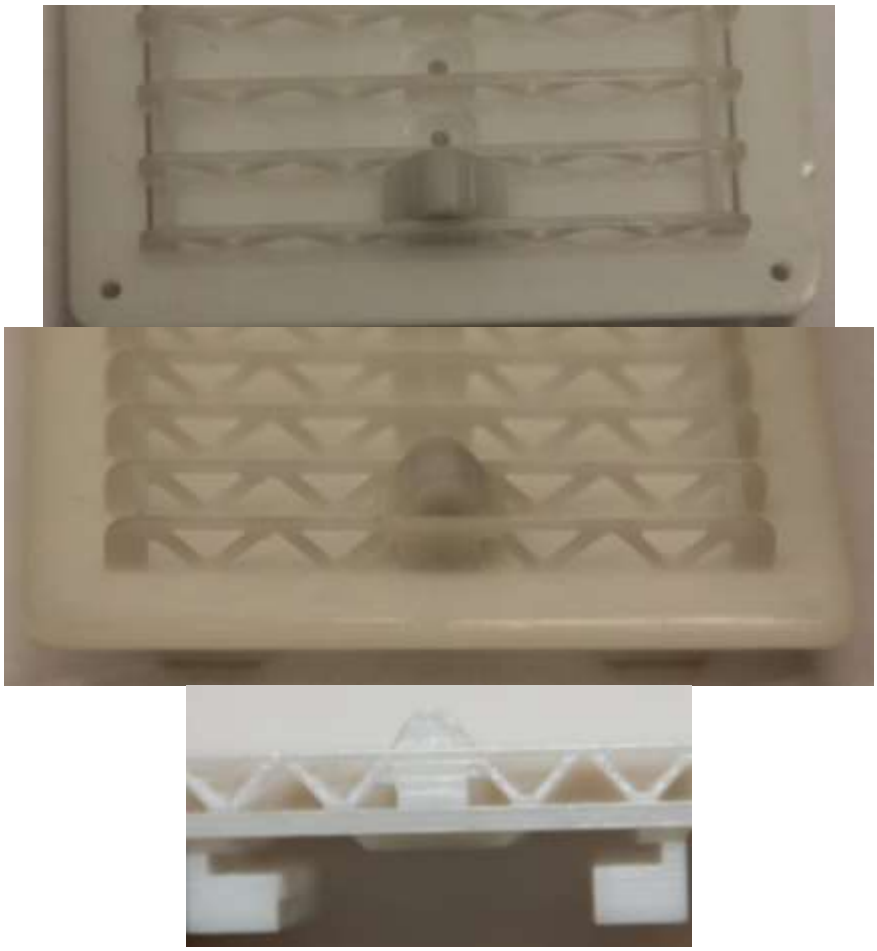

Step 12. Install Corrosion Sensor PCB

The populated and conformal coated Corrosion Sensor PCB should now slide into the back of the corrosion sensor mount. Align the board such that all the mounting holes match up.

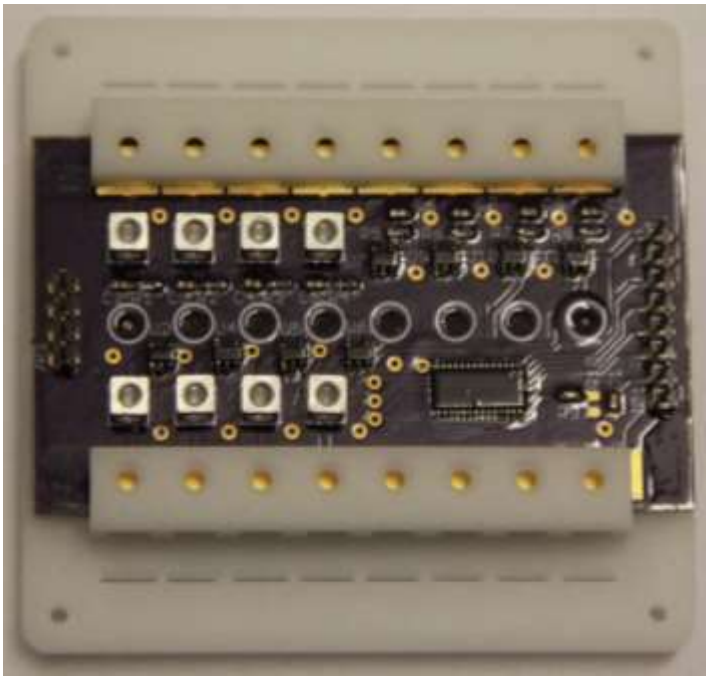

Step 13. Secure Humps with Screws

Use the pan head M2x10 machine screws to tighten down all eight humps to the corrosion sensor mount.

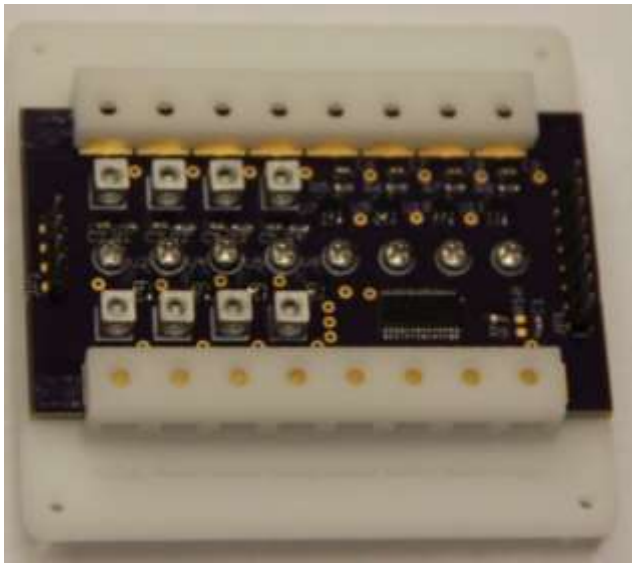

Step 14. Insert strip locking nuts and screws

The strip locking nuts press the strips against the PCB pads and prevent the strip from moving out of position. There are eight locking positions for the strips which require the use of 8 M2 nuts and 8 M2x6 countersunk screws. Slide each nut into the SLA opening above each PCB pad and thread the screw onto the nut such that it gets pulled into the hexagonal recess.

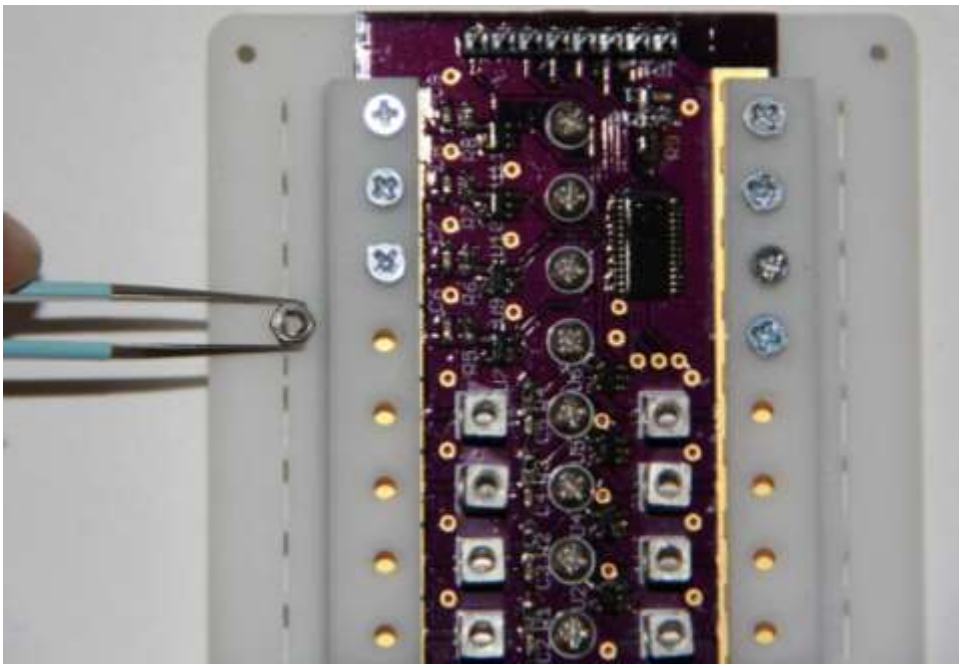

Step 15. Load Wires

The wire corrosion sensor electrodes mount into channels 1-4 and uses the screw terminals located on the corrosion sensor PCB. Cut a six inch section of wire and thread it though each end of the channel mount such that three inches remain on each side of the humps. Using tweezers feed the wire into each of the screw terminals and insert and tighten the screw. Wrap one of the wire ends around the screw such that it no long slips then tighten the wire onto the hump by pulling the other end. Wrap this end around the

remaining screw terminal. The wire should have very little slack over the hump. Add a small application of TEROSON MS 939NA electrically conductive adhesive to bond the wire to the screw terminal.

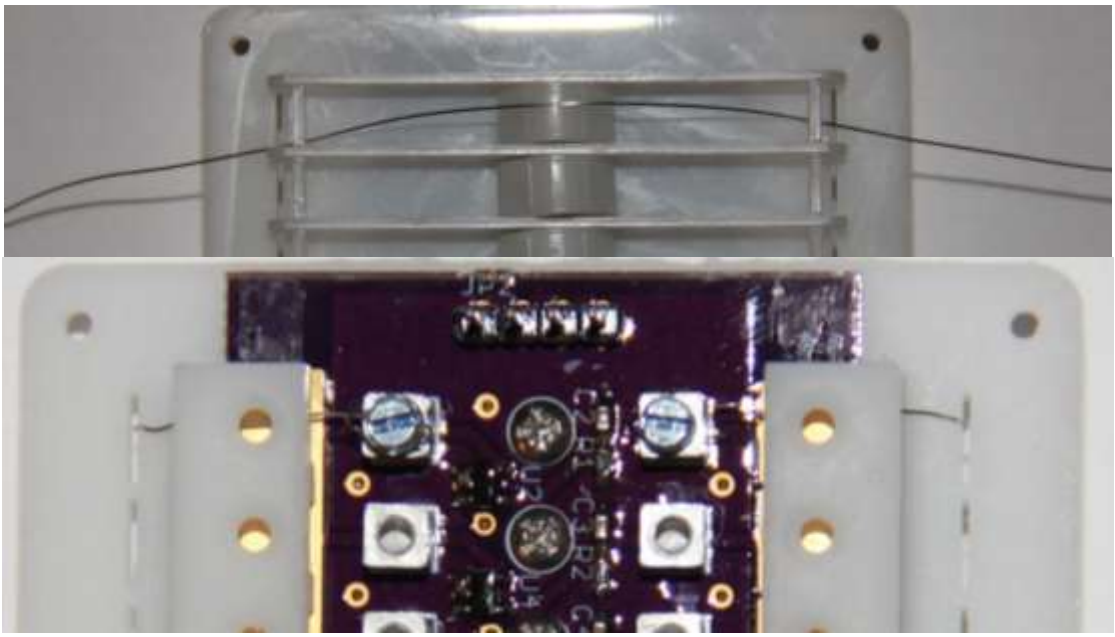

Step 16. Bend Strips

The strips need to be pre-bent to both correctly fit on the hump and to be pre-stressed in order to increase the chances of corrosion occurring on or near the hump. To do this, place the center of each strip on the rubber eraser pad and use the metal cylinder to depress it. This will place a crease into the strip that will be aligned to the hump. The strip is longer then required and will be trimmed when mounted into the sensor.

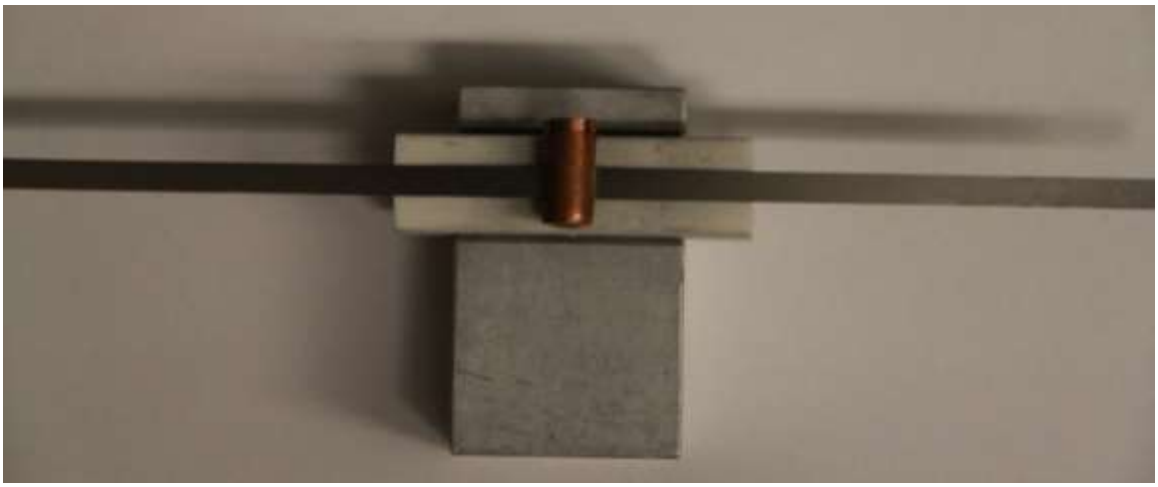

Step 17. Load Strips

Each strip must be loaded carefully and excessive bending should be avoided at all costs. Feed the ends of the strips into the slots of the corrosion sensor channel. These must then be fed into the slot containing the screw and pulled through. Depending on the thickness of the strip, this part may or may not be difficult. If the strip is thick, grabbing the tip of the strip with needle nose pliers is an option to help feed the strips into position. When in place, the pre-bent section should be resting on the hump. Tighten the strip mounting screws such that the strip is sandwiched between the screw and the PCB pad. Do not over tighten the screw as this can crack the SLA. Trim the excess strip material to prevent shorts. Add a small application of TEROSON MS 939NA electrically conductive adhesive to bond the strip to the pad.

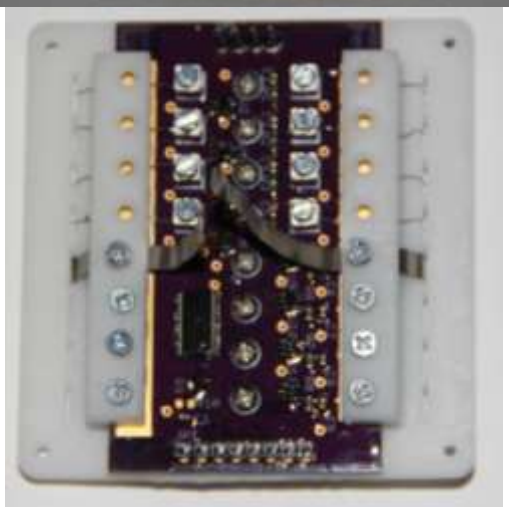

Step 18. Remove Hump Screws

When all channels are loaded and all sensor electrodes are secured the hump screws may be removed to place the electrodes under tension. Once removed, preform a continuity check to ensure that all the electrodes remain functional and are making good contact.

Step 19. Mount Corrosion Sensor Assembly with Silicone (screws)

Apply a thin layer of silicon around the edge of the corrosion sensor and then place it into the cutout located on the aluminum case lid as shown below. Use the M2x10 screws and M2 nuts to secure the corrosion sensor. Place additional silicone around the edge of the SLA where the SLA and aluminum meet.

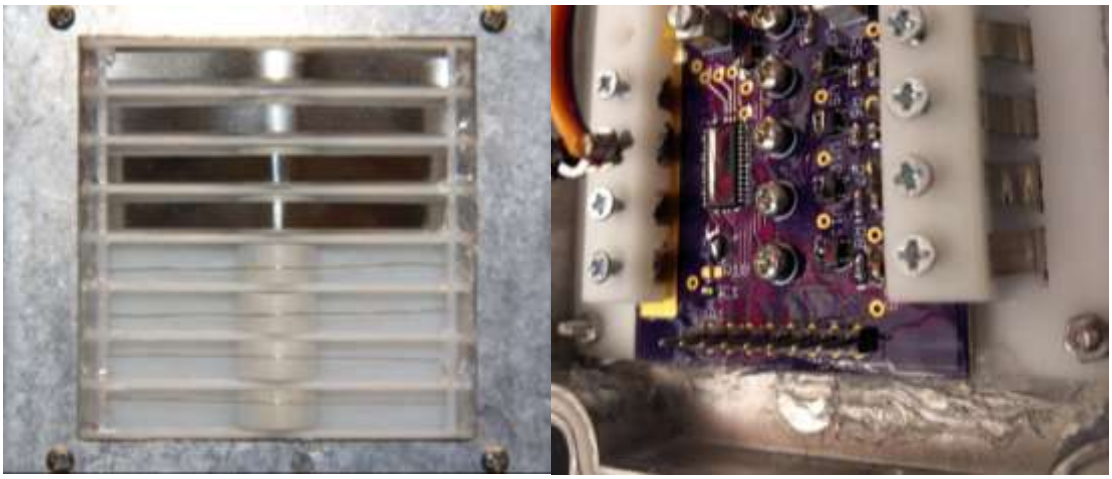

Step 20. Foam Tape TOW and Corrosion PCBs

The TOW sensor and corrosion sensor PCBs are conformal coated, but there is still a potential for shorting if they are placed in direct contact with the aluminum case (which is conductive). The case is also thick such that placing the sensors directly onto the PCBs would make them recessed into the case, which would cause electrolyte buildup within the recess, potentially skewing the results. To fix this, place a layer of double sided foam tape on the PCB and onto the back of each sensor. The tape should not cover the sensor connection vias! Leave the protective film on the tape for now. See the pictures below.

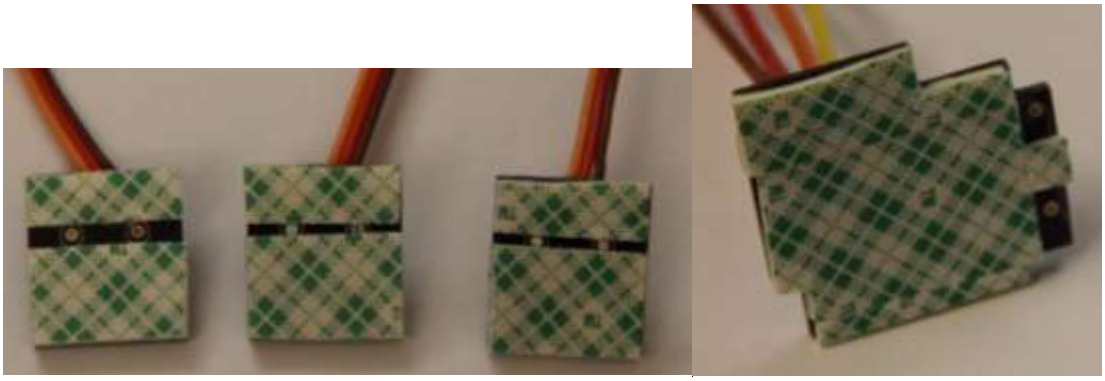

Step 21. Solder TOW Sensor onto PCB

Place a square of foam tape on the back of the TOW sensor and remove areas of tape covering the vias. Remove the protective film from the tape on the TOW sensor PCBS and attach the TOW sensor such that the vias line up. Using a bright light can help with properly lining up the vias on the sensor and PCB. Once attached, place a strand of solid 26 AWG wire through the vias and solder both sides (PCB and TOW sensor). Use care when soldering the gold pads and use silver solder. Trim the nubs on the leads and inspect the TOW sensor for damage.

Step 22. Clean and Conformal Coat TOW Solder Joints

The solder joints on the TOW sensor will be exposed to the corrosive environment and need to be protected. Trim them down using clipping pliers and then conformal coat them. Be sure to only conformal coat the pads and not the comb section of the sensor or it will not function correctly.

Step 23. Mount TOW Sensor

Insert the TOW sensor into the lid opening as shown below. The foam tape should now evenly adhere to the inside surface of the lid. A thin layer of conformal coating may be added at this point around the edges of the foam tap to further secure it and prevent leaks.

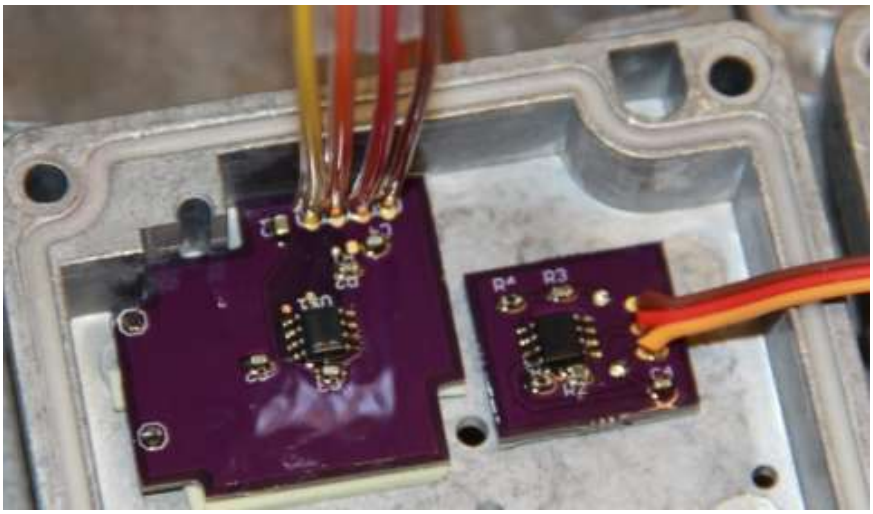

Step 24. Cut Notches into Corrosion Sensor

The atmospheric corrosion sensor is a galvanic sensor that will begin to corrode the moment it is exposed to any electrolyte and the water in the air. Once the sensor is exposed, there is a time table in which the assembly must be completed and placed within the testing chamber. For this reason steps 24-27 may be completed later after step 39.

The atmospheric corrosion sensor cutout is exactly the correct size to fit the sensor, but the contact wires for the sensor are on the exposed side. To connect these sensors properly, two grooves are needed to be cut to allow the sensor wires to reach the pads. Using a Dremel cutting disk, place two notches into the sensor near the connecting pads as shown in the figure below. These will allow the two contact wires to reach the exposed side of the sensor from inside the case.

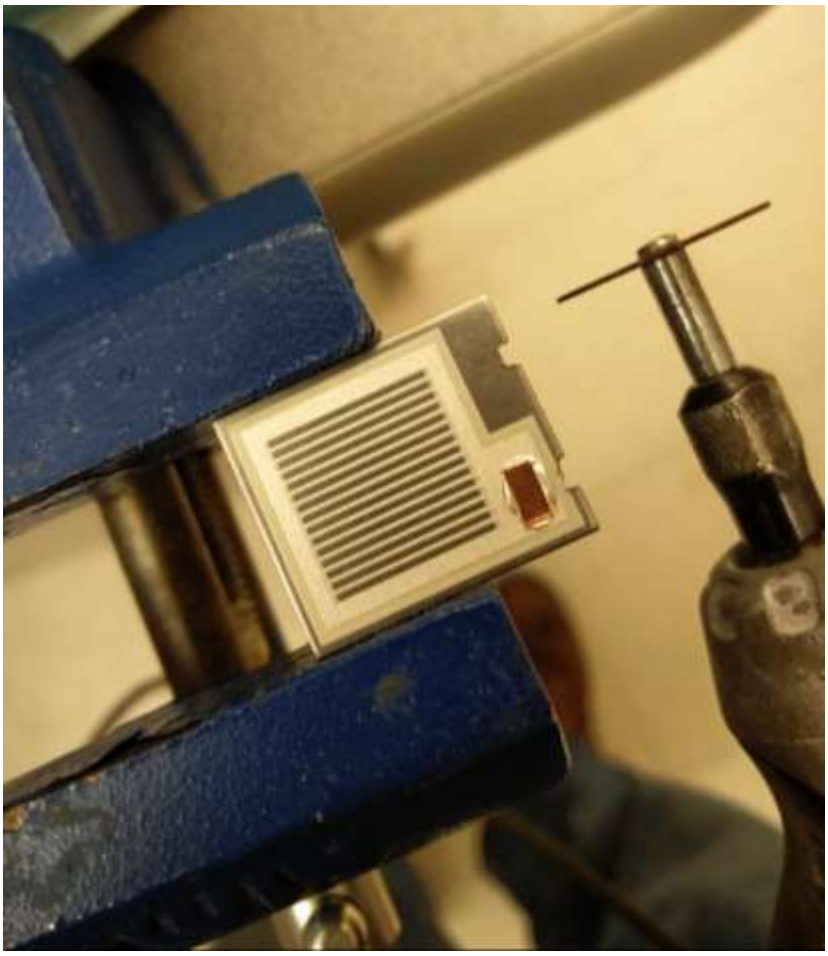

Step 25. Mount Corrosion Sensor

The white square on the top surface of the corrosion sensor board shows the outline of where the atmospheric corrosion sensor will be. Place foam tape on this surface of the PCB and trim the tape such that the entire surface of the PCB is covered, minus the sensor contacts. Remove the protective film and mount the sensor into the case as shown below. Apply foam tape to the back of the atmospheric corrosion sensor such that the entire surface is covered minus the notched area. Place the sensor in the cutout and guide the wires through the notches as shown below. Trim and strip the wires so only a small amount of exposed wire reaches the pads on the senor. Solder these wires to the pads quickly and do not let the plastic coating on the wires melt.

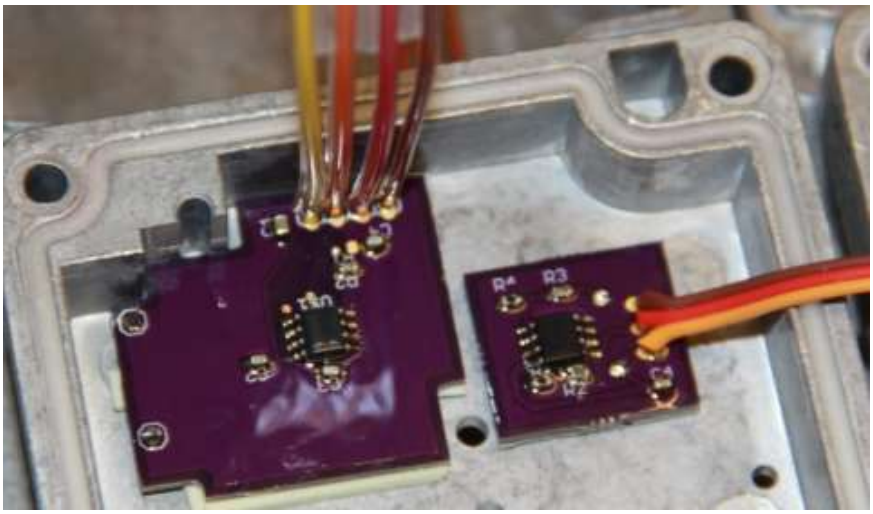

Step 26. Conformal coat corrosion sensor

Trim and clean the soldered contacts on the atmospheric corrosion sensor. Conformal coat these joints without covering the remaining portion of the sensor.

Step 27. Test for Shorts

At this time, check for shorts across all of the connected sensors and fix any problems found. Additional silicone my now be applied to ensure that liquids will not be able to enter the sensor module case.

Step 28. Sand Ethernet Jack

The weather proof Ethernet jack needs to be sanded in order to fit properly into the case. When looking at the jack one can see that the port is not a perfect circle, but more of a “D” shape. This flat part of the jack must be evened out by sanding it down as shown below. Using a long flat file works well, but ensure that the wires are not damaged. If sections of the wire coating are damaged then conformal coat them and double check conductivity.

Step 29. Mount Ethernet Jack

Place a strip of electrical tape in the slot near the Ethernet jack cutout so the wires will not rub against the aluminum housing. Place the rubber washer onto the jack and insert it into the cutout. Push it forward until it snaps into place. Screw the retaining nut on the jack and tighten it to the point where the rubber washer makes a good seal against the aluminum. It will be fine if the jack is slightly twisted.

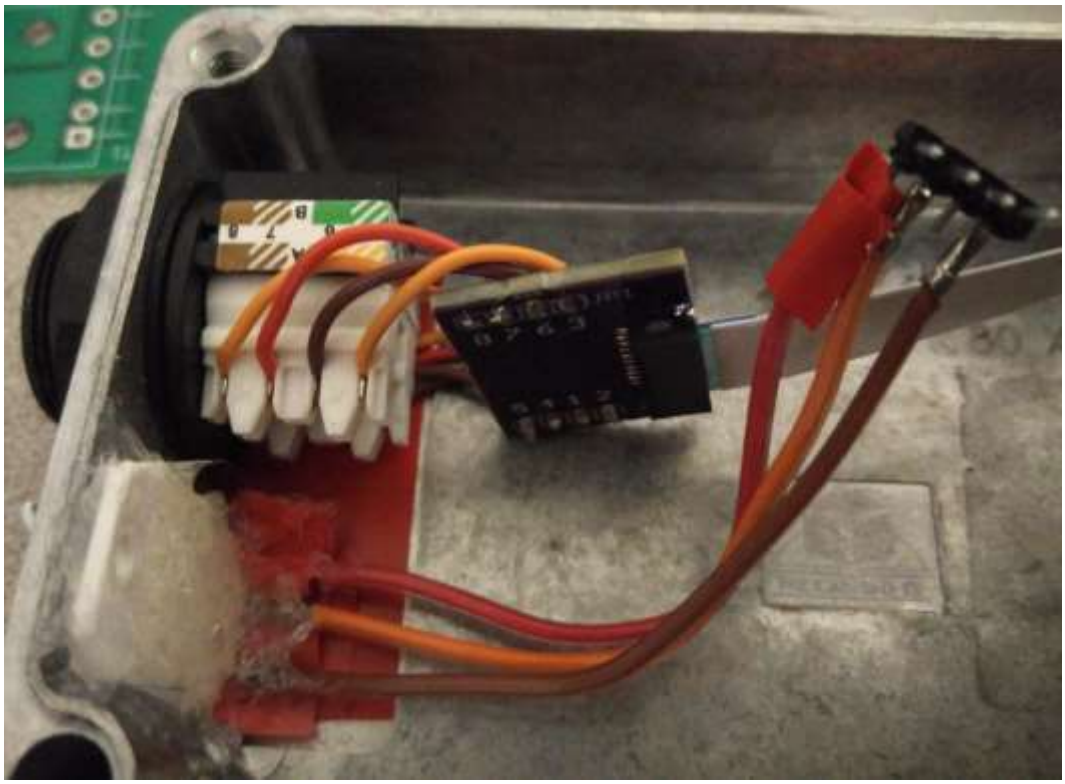

Step 30. Mount Humidity Sensor

The humidity sensor is mounted on the bottom facing side of the sensor module to prevent liquid water from saturating the humidity element. The four wires coming from the sensor will be in very close quarters with the aluminum case which presents the possibility of shorting. To prevent this, place electrical tape both in the sensor cutout as

well as the area in front of the cutout. The plastic casing of the humidity sensor should be flush with the exterior of the aluminum case. Once in this position, use silicone to secure the sensor in place. Prevent silicon from coming in contact with the sensor element, but ensure that the wire contacts in the case are completely covered in silicone and protected.

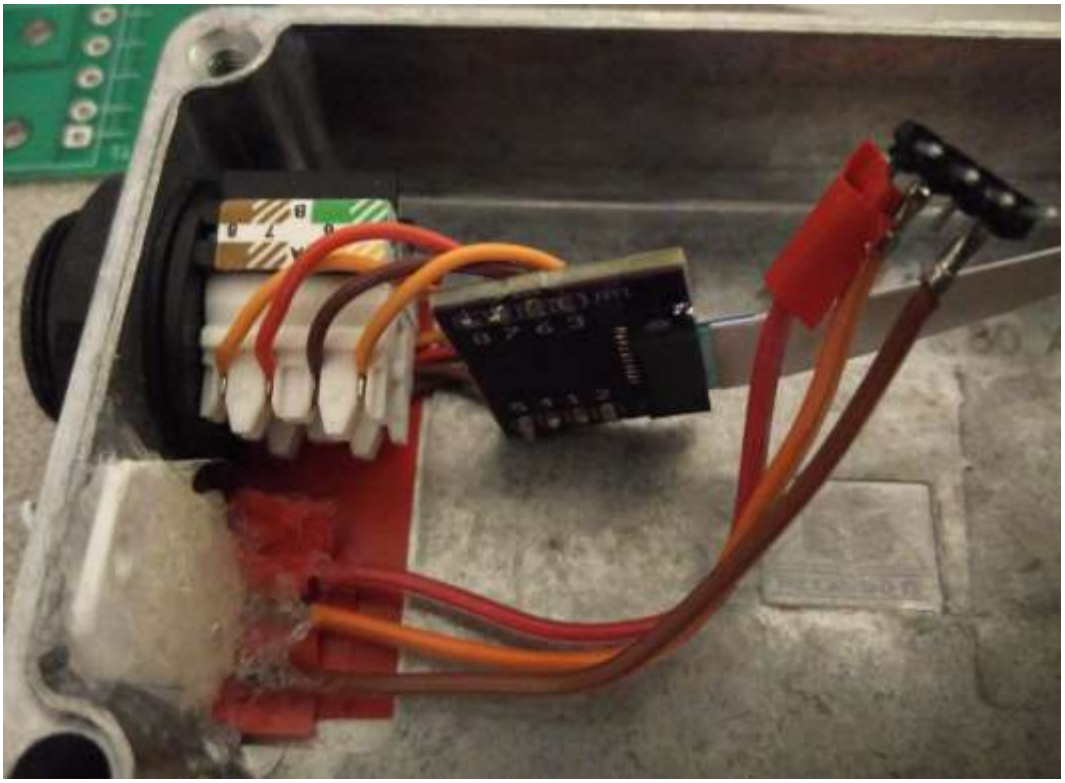

Step 31. Install Motherboard

Connect the motherboard PCB to the corrosion sensor PCB by aligning the headers on each board and connecting them together. Make sure that none of header pins have bent, and that once inserted, the male pins have been completely covered by the female shrouds.

Step 32. Install TOW and Corrosion Sensors Wires

Connect the TOW and atmospheric corrosion sensors to the motherboard by plugging them into their corresponding headers. Placing bends into the wires will keep tension off of the solder joints and prevent the cables from pressing against each other.

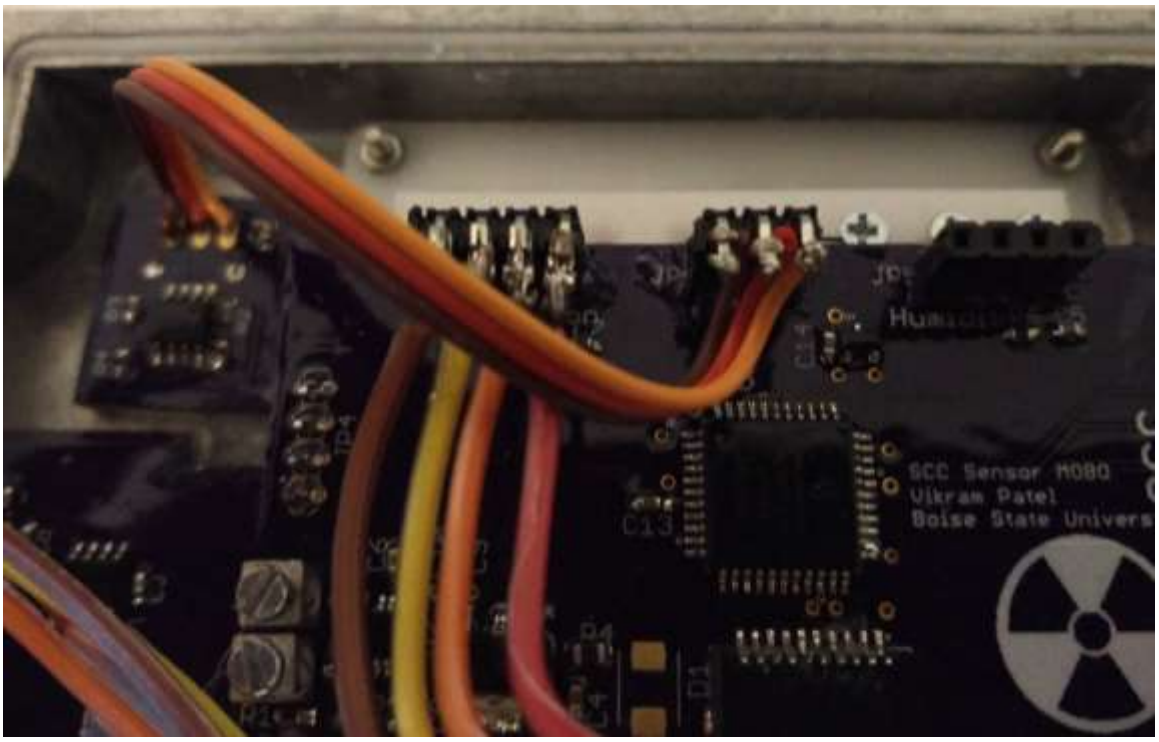

Step 33. Strip Thermocouple Leads

The thermocouples have enameled wires that need to be stripped in the areas that need to be conductive. It should be noted that only the section of the wire going into the thermocouple screw terminal should be stripped. Extra stripped wire may lead to shorting the sensor. Use very fine sand paper to strip the enamel off the wires and test the conductivity of the sensor using an ohm meter. If the thermocouple registers as open on the ohm meter then further enamel must be removed from the sensor.

Step 34. Mount Thermocouple

The thermocouple groove on the top of the aluminum case lid is shorter than the full length of the sensor. Thread the thermocouple through the hole at the end of the groove on the lid such that the wires are inside the case. Bend the thermocouple such that the tip of the thermocouple rests at the end of the grove and the rest of the sensor is flush with the lid.

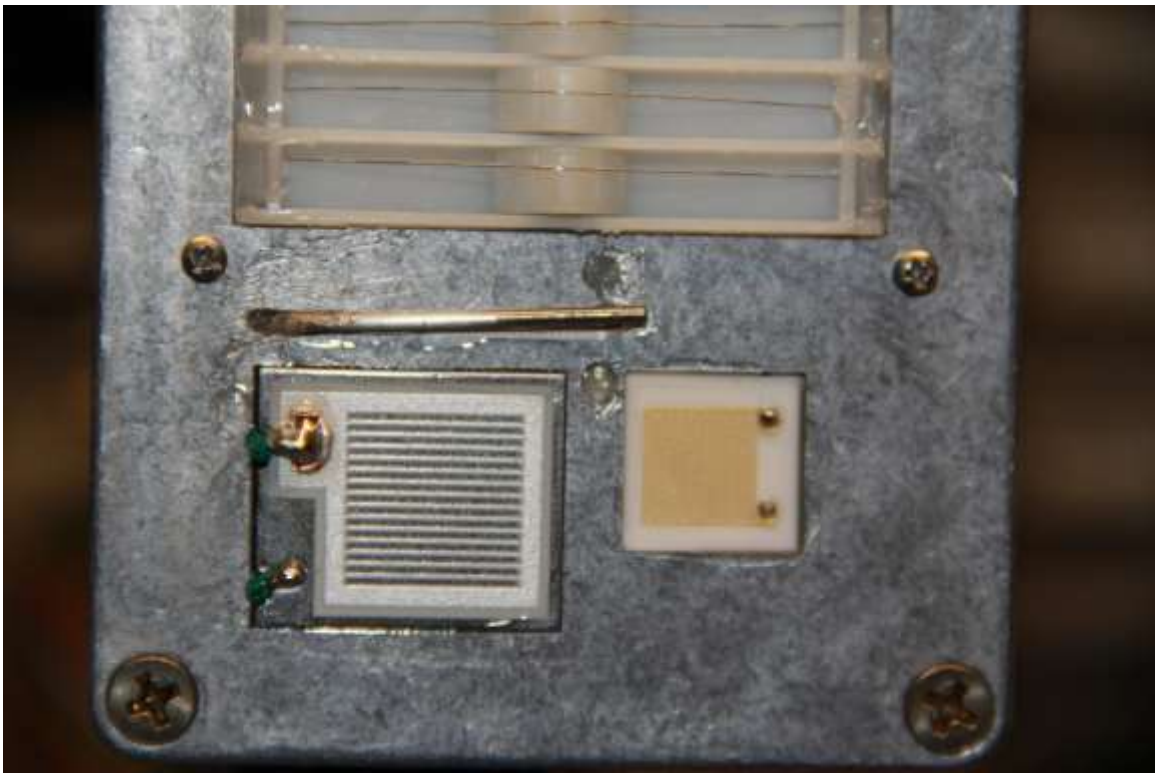

Step 35. Install Thermocouple Wires

Place a piece of electrical tape over the TC to prevent it from moving. Tread the thermocouple wires into the thermocouple screw terminals on the motherboard and lock them in. Test for conductivity and verify that there are no shorts with the aluminum case. Silicone the TC form the inside of the aluminum case such the liquids would not enter case through the hole. Once this silicone is dry, add a small amount of conformal coating to the thermocouple hole from the outside of the case. The thermocouple leads are very susceptible to corrosive material and should be conformal coated as well up to the screw terminals.

Step 36. Connect FFC Cable between Ethernet Port and Motherboard

Connect the ten pin FFC cable from the Ethernet jack PCB board to the motherboard. Double check that the friction lock is holding and the cable is not bent in the receptacle.

Step 37. Install Humidity Sensor Wire

Connect the humidity sensor to the motherboard by plugging it into the corresponding header. Placing bends into the wires will keep tension off of the solder joints and prevent the cables from pressing against each other.

Step 38. Test for Dead Short

Install the test Ethernet cable and tool chain into the Ethernet jack. Do not power the system on. Check for a dead short between VDD and ground on both the 5V rail and 3.3V rail. If there is a problem then track it down. The overall system load will vary depending of the geometry of the corrosion sensor elements used.

Step 39. Power Up Test

Supply the sensor module with 5V at 150mA via the barrel jack on the programming board. Check to see if the current draw is acceptable and check all voltage rails. Debug any problems found.

Step 40. Program Board and Confirm All Sensors

Program the board using the provided hex file and the tool chain. Look for the startup message on the serial terminal using the following settings:

- 9600 baud
- 8-bit
- No parity
- No hardware flow control

Observe the data coming from each sensor and verify the atmospheric sensor readings with the lab standard (temperature and humidity).

Step 41. Seal Aluminum Enclosure

Seal the enclosure using the four case screws. Be very careful not the pinch any of the wires when closing the case. The rubber seal should be flush around the entire seam of the case. Double check steps 38-40 after the case is sealed to ensure nothing was damaged in this step.